

義大研訊

SEARCH & DISCOVERY
RESEARCH AT ISU & EDH



目錄

消息報導	3
義大新成立「醫學系」招收首屆公費生30名	3
義大牽手大樹區 共育「荔枝傳情」升級版	6
修課達標即可前往NTU「3+1」雙學位再進化	8
導入數位醫療技術 百壽堂與義大簽約交流互惠	11
博而美贈正子斷層掃描儀 義大醫療研發能量再升級	14
「影視系」喜連來好光彩 《小白船》獲金穗獎優等、 最佳攝影	16
青春設計節放閃 原民編織展牆「金」獎榮譽	19
義大男籃摘銀 辦球迷歡見會	21
義大「醫學體感中心」引進全國首台健身模擬器	23
歡聚「義術節」 全球各地師生慕名而來	25
文摘	27
Study of Al doped ZnO layers inserting CuO nanorods structure to apply on Flexible Transparent Conductive Electrode	27
The effect of Botox injection compared with usual therapy on activity in children with cerebral palsy A systematic review	43
Nonlinear Dynamic Analysis of Gear Pair System Based on Crack Rotor-Bearing System with Rub-Impact Effect	56
光子晶體光纖之洩漏模態分析	81
物聯網系統架構與應用開發簡介	92

目錄

活動	104
機會	108
編輯室	120

義大新成立「醫學系」

招收首屆公費生30名

創校即將邁入29年，甫獲教育部肯定設立「醫學系」的義守大學，108學年度將招收首屆「醫學系」公費生，併同106年創設的「醫學檢驗技術學系」，義大「醫學院」系所資源更形完備，一躍成為全臺唯四設有「醫學院」的綜合大學，教學績效獲各界肯定。



圖一、義大「醫學系」將於108學年度招收30名公費生。

擁有9大學院的義大，自民國87年設立第一個醫學相關科系、102年獲准成立「醫學院」，並設有全國唯一協助邦交國培育醫療人才的「學士後醫學系(外國學生專班)」，迄今共擁有13個學系及兩個專班；新成立的「醫學系」於新年度將招收首屆30名公費生，包括10名一般公費生、10名金門、澎湖、蘭嶼、綠島、小琉球等離島公費生及10名原住民生。

義大校長陳振遠表示，義聯集團旗下義大醫療體系目前擁有3家醫院，除提供優質醫療服務，也是義大「醫學院」各系所教學與研究的最強後盾；而面對臺灣偏鄉醫療人才與資源長期匱乏課題，義大在集團創辦人林義守期許下，義無反顧肩負使命，將為縮短城鄉醫療差距及培育醫療人才貢獻心力。

「醫學院」院長陳翰容表示，義大是一所綜合大學，除有義聯集團與義大醫院作為強力後盾，未來「醫學院」更可透過連結義大的理工、電機資訊、管理、國際與原民等9大學院，讓智慧醫療網絡更強大；此外，義大「後醫系」採全英語教學，已有60名畢業生學成返國，可望成為邦交國家醫療領域棟樑，對我國醫療外交極具意義。

針對提高公費生紮根偏鄉意願，義大「醫學系」主任梁正隆指出，未來公費生到偏鄉服務，不論是進修或醫療上需求，學校及醫院都會給予強力支援，目前亦積極發展遠距醫療，未

來新手醫生透過遠距醫療網絡，便能及時獲得專業協助，讓新人更有信心根留偏鄉；而為了讓高三學生了解自己適不適合當醫師，義大「醫學院」將於2月21日起，首辦3天免費醫學營，讓高中生體驗基礎醫學與生物生化實驗，並安排到臨床醫院見習、看大體解剖過程、縫合練習初體驗，以及CPR訓練等，課程結束後也將頒予證書。



圖二、義守大學醫學院培育邦交國醫療人才，採全英語教學多年，未來也將以智慧醫療作為發展。

義大牽手大樹區 共育「荔枝傳情」 升級版

繼與屏東三地門鄉、高雄內門區簽約合作後，義守大學於108年5月7日再與高雄大樹區公所簽訂「地方創生合作備忘錄」，將結合9大學院專長，針對觀光發展、科技農業、人才培育中心、扶老攜幼、微電網五大主軸攜手連結，期能把大樹「鳳荔傳情」獨特文化風情發揚光大，共同培育「高雄後花園」更美好成果。



圖一、義大團隊與高雄大樹區公所簽訂 MOU，共育「高雄後花園」。

今簽約活動除大樹區區長陳進雄、主秘王瑞麟與公所團隊多人出席外，行政院南部聯合服務中心組長許文瑞、高雄市政府研究發展考核委員會組長王士誠等亦到場，顯示對義大和地方社區合作的看重；義大方面則由校長陳振遠、副校長沈季燕、研發長陳俊益率各學院院長等多人參與，並透過共識會議交流激盪，勾勒出未來「地方創生」的大致方向。

今年為地方創生元年，義大校長陳振遠表示，全臺各地區大學也積極在推動，義大9大學院優勢具備各種專業，能夠集思廣益，發揮綜效；大樹區區長陳進雄強調，大樹區已有「玉荷包荔枝」、「金鑽鳳梨」等聞名農產品，舊鐵橋溼地公園、佛陀紀念館等亦是大樹區特色景點，期待透過地方創生計畫，活絡產業及刺激在地經濟。

義大校方研發長陳俊益指出，義大預期將與大樹區合推「人才培育中心」，以觀光餐旅學院為主力，針對飲料調製、食品加工及開發、觀光導覽、民宿規劃4大項進行人才培育，增加就業機會；在科技導入面向，則研擬開發大樹區旅遊資訊APP，提升便利性與吸引力，打造數位大樹未來。

修課達標 即可前往NTU 「3+1」 雙學位再進化

在義大讀大學，同時取得英國名校學歷！義守大學(ISU)與英國諾丁漢特倫特大學(Nottingham Trent University, NTU)的「3+1」跨國雙學位學程再進化，未來義大的商管相關科系學生，完成前三年大學課程，並通過NTU認可的PEAP(Pre-Sessional English for Academic Purposes)學術英語課程，即可於大四前往英國NTU攻讀商管學位；透過無縫接軌，學生4年內可同時取得義大及NTU的雙商管學士學位，超級超值大利多。



圖一、英國諾丁漢特倫特大學校長 Prof. Cillian Ryan (右) 與義大校長陳振遠代表簽約，正式啟動「2 degrees, 2 cultures」與 PEAP Program 計畫。

義大校長陳振遠表示，義大致力推動成為跨疆界的「Education Hub」，積極連結全球各大學進行「2+2」、「3+1」雙聯學位合作，此次ISU和NTU兩校得以深化落實”Two degrees, Two cultures”，特別感謝義大國際事務處、國際學院及管理學院的主管與同仁共同戮力促成，期許未來有更多義大生前往英國取得學位，強化國際競爭力與移動力。

為表示深化合作誠意，英國諾丁漢特倫特大學校長Prof. Cillian Ryan專程赴義大簽約，宣示兩校正式啟動”Two degrees, Two cultures”與PEAP Program計畫，專責開設準備就讀NTU國際商管課程所需的專業英語課程，並引導熟悉英國大學上課方式、文化及需求，讓學生具備大四直接進入NTU就讀能力。

簽約現場有一位畢業於義大進修部的傑出校友陳冠奴，多年前從義大「企業管理學系」進修部畢業後，前往英國知名的曼徹斯特大學、新堡大學NEW CASTLE攻讀碩博士，目前為NTU專任教授；此次特別隨行回母校簽約，提起當年義大補助她到英國交換6週，讓她打開眼界、矢志出國，最後進入名校圓夢，進而認識也在就讀博士班的英國籍老公，如今事業與感情順遂。回首來時路，她認為首要歸功義大交流計畫，讓她翻轉人生，感謝母校當年的栽培。

兩校雙學位PEAP計畫將於108學年度上路，未來就讀義大「國際企業經營學系」、「國際財務金融學系」、「娛樂事業管理學系」、「企業管理學系」的學生，可從大一起選讀PEAP Program，採全英小班教學，提供師生更多面對面交流互動與英國文化體驗的實戰經驗。



圖二、NTU 將在義大開設 PEAP 學術英語課程，兩校雙學位合作再進化。

導入數位醫療技術 百壽堂與義大 簽約交流互惠

AI時代來臨，越來越多產業關注數位化發展；進駐義守大學「創新育成中心」的廠商「台灣百壽堂高新科技開發股份有限公司」與義大舉辦產學合作簽約儀式及健診體驗活動，雙方未來將共同強化大數據分析管理，朝智慧醫療領域攜手邁進。



圖一、「台灣百壽堂」張鴻川董事長（右）與義大陳振遠校長簽署產學聯盟意向書。

義大由校長陳振遠率隊，「產學智財營運總中心」副主任洪添燦與多位系所主任、老師出席，「台灣百壽堂」董事長張鴻川也攜主管們一同參與見證；「台灣百壽堂」第九代傳人張鴻川董事長，深感數位浪潮無法擋，因此創立高新科技研發子公司，歷經多年努力後，將AI與傳統中醫理論結合，研發出第三代電腦示波的中醫數位檢測機，可應用於偵測身體潛在疾病，提供醫生更精準的治療參考，有助於延緩並有效控制疾病。

陳振遠校長致詞時表示，感謝「台灣百壽堂」提供先進儀器，讓師生教學使用，希望雙方後續合作更緊密；張鴻川董事長則說，這是首次與學術單位產學合作，意義深遠，數位檢測機近期通過ISO、GMP認證，並榮獲多國專利，可說是精準醫學和數位中醫重要里程碑，也期望藉此與中醫診所、義大醫院等醫療單位攜手合作，共建大數據資料庫，營造三贏，從疾病源頭進行管理，朝向精準醫學邁進。

「台灣百壽堂」研發的中醫數位檢測平台系統，便於檢測人體經絡，同時能透過數據判讀，分析隱性、慢性疾病等，有助於提早發現、對症下藥；該儀器將提供給義大「學士後中醫學系」師生教學使用，並蒐集使用意見，適時回饋以求改良進益；另外，也將連結義大「資訊管理學系」及「資訊工程學系」等系所進行產學合作，共同建構大數據分析平台，完善檢

測數據管理；而研發第三代擬真型雷射針灸儀的「生物醫學工程學系」教授王智昱教授，也藉機分享他的研發成果，雙方交流熱絡。



圖二、義大陳振遠校長體驗中醫數位檢測機健診，由張鴻川董事長（右）示範儀器操作。

博而美贈正子斷層掃描儀 義大醫療 研發能量再升級

教學研發能量UP！繼上週知名中醫高科技公司提供最新電腦示波的中醫數位檢測機，「博而美國際股份有限公司」捐贈一台全新，同時也是全臺唯一的「乳房正子斷層掃描儀(Mammi PET)」給義守大學，可望挹注更多教研能量。



圖一、「博而美公司」18日捐贈全新且全臺唯一的「乳房正子斷層掃描儀」給義大，陳振遠校長與鄧先毅董事長等雙方人員，共同見證。

捐贈儀式由義大校長陳振遠、「醫學院」院長陳翰容及多位系所主任、老師共同見證，「博而美公司」則由董事長鄧先毅率隊，總經理簡博昌、顧問李俊信等出席盛會；鑑於對醫療服務與品質的重視及要求日益增長，為提供和滿足國人醫療資源需求，「博而美公司」董事長鄧先毅，廣結醫療精英籌組團隊，30多年來致力引進國外高科技醫療設備，藉以進行研發和提升國內醫療水準。

陳振遠校長致詞時表示，感謝「博而美公司」捐贈先進儀器，造福義大師生，希望未來在教學與研究上，均能發揮最大效用，攜手培育頂尖醫療人才，回饋社會；「義大是最好的落腳點」鄧先毅董事長表示，除感佩義大創辦人林義守對教育的投入，以及本著取之於社會、用之於社會的理念，決定捐贈給義大，除能嘉惠學術教育單位與莘莘學子，同時作為最佳實踐社會責任的機會。

「博而美公司」捐贈的正子斷層掃描儀，除影像空間解析度可達1mm，相較於須擠壓乳房、2D成像的X光攝影檢查，新儀器設計能讓女性患者感覺較為舒適，診斷出局部乳癌的位置也較為精準；此外，該設備除有助於偵測結果更為精細，未來在癌症、分子藥物研發、藥物活性動態分佈，以及臨床前動物研究上，均能提供先進分子醫學影像，大幅強化研究能量。

「影視系」喜連來好光彩 《小白船》 獲金穗獎優等、最佳攝影

義守大學「電視與電影學系」學生攝製的數部短片作品，近日連傳得獎好消息；由來自馬來西亞的蘇智雄所導演《小白船》，繼去年放視大賞銅牌獎後，再榮獲第41屆金穗獎學生作品類的優等、最佳攝影獎，而《蘋果》、《彌留》、《負子》等片，也陸續獲得各獎項青睞，表現搶眼。



圖一、《蘇智雄（右）執導、李威權（中）擔任主攝影的《小白船》，獲得國內外多想獎項肯定。

《小白船》一片取材導演自身故事，也是去年度畢製作品，除獲得放視大賞銅牌獎，亦入圍華盛頓華語電影節「劇情短片」主競賽單元、Seashort馬來西亞新秀影展10強，以及福爾摩沙影展；導演蘇智雄面對各方肯定，謙虛表示「很幸運」，特別感謝製片許祖寧，以及同獲金穗獎肯定的攝影師李威瑾等，強調跨國團隊合作無間，才能有如此佳績，期許未來還能拍出更多撫慰人心的作品。

蘇智雄非常珍惜臺灣創作環境，回顧《小白船》拍攝點滴，他說，一度陷入低潮，幸賴老師鼓勵與偶然觀看馬國電影後，才重新找回真正想傳達的內涵，並在影片中置入馬國獨特音樂元素，藉由同學林晉德混音技巧，傳達出適切氛圍，幫影片加分許多。

而由義大「影視系」大三學生萬簫桐導演、簡嘉儀製片的《蘋果》，亦獲得創教育影展的首獎，該短片描述女性成長過程中身體意識萌芽，反思社會審美與商業廣告中對女性的物化，帶給青春期女孩的負面影響；簡嘉儀同學指出，劇組成員多數為女性，第一次合作難免遇上須不斷修改的挑戰，她坦承原本沒有要報名比賽，但受到李志薔老師鼓勵而嘗試，謝謝教育影展肯定，也激發同學們繼續拍片的信心。

來自香港的學生導演陳漢華所執導的《彌留》，則獲得藝美獎最佳劇情短片；陳漢華表示，近期經常聽聞身邊長輩

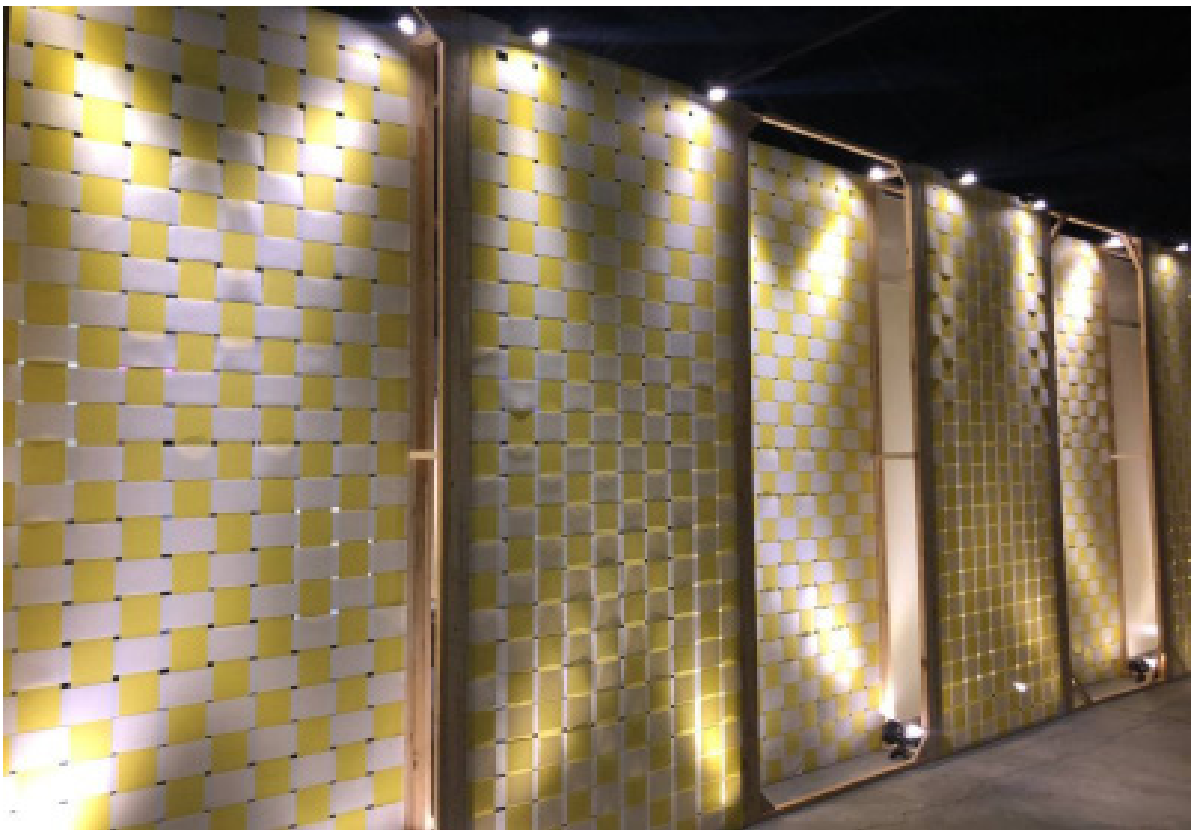
故事，興起以此為題創作靈感，演員多數由系上同學扮演，相當出色，而他更特別把香港阿嬤原型放進劇情中，藉此傳達對長輩的感念；《彌留》的音效也是由義大「影視系」同學蔡昱邦原創製作，而蔡昱邦所製作的另一部短片《負子》，同時獲得今年度藝美獎最佳音效混音。



圖二、「影視系」學生萬蕭桐導演與簡嘉儀製片的《蘋果》，獲得創教育影展的首獎。

青春設計節放閃 原民編織展牆 「金」獎榮譽

邁入第10屆的「青春設計節」，可視為南臺灣設計領域規模最大的競賽活動，義守大學原住民族學院「傳播與設計原住民專班」今年以編織牆作為展牆，獲得觀眾與評審青睞，榮獲「創意設計競賽場地設計金獎」，也是義大首次贏得該項榮譽。



圖一、義大原民學院「傳設原民專班」，以南島原住民編織文化元素作為展牆，榮獲「青春設計節」場地設計金獎。

今年「青春設計節」共計754件作品參賽，義大原民學院「傳設原民專班」以《是生活》為主題參展，10件作品涵蓋以音符譜出追求夢想過程中的樂章，用影像留下部落生活日常，藉文字縫合社會對原住民的刻板印象、紀錄原住民生活裡頭的親情故事，拍攝照片呈現特殊行業工作者的污名化，以及運用視覺傳達自然環境的重大議題和經由設計結合部落產業等面向。

當贏得「場地設計金獎」消息傳來時，《是生活》指導老師胡哲豪興奮表示，該獎項是「青春設計節」團隊設計最高榮譽，共有22所大專院校、46個設計相關科系參與競爭，今年義大能脫穎而出，值得驕傲；他說，展覽隔板以南島原住民編織文化元素加以發想，前後共動員21人、花了半學期籌畫執行，可喻為師生們共同努力後的豐收。

除原民作品吸睛外，義大「創意商品設計學系」學生作品《Lumincone交通錐》，也入圍「青春設計節」立體造型暨產品設計類；另外，在同樣被視為設計領域重要展演平台的「放視大賞」上，義大「數位多媒體設計學系」的《狐說》、《生森》、《禘之》、《探雷針》作品，亦入圍創意企劃類，而《造夢者》、《艾爾克謎》、《神遺》等組別，則入圍遊戲類—PC遊戲創作組。

義大男籃摘銀 辦球迷歡見會

為慶祝義守大學男籃隊在UBA大專籃球聯賽中摘銀，創隊史最佳成績，「餐旅管理學系」結合校內實習課程，特別舉辦慶功宴和球迷歡見會；校長陳振遠親自為隊長徐鈺順戴上冠軍戒指，鼓勵球員再接再厲，而謝玉娟教練也精心準備禮物送給球員，並請師長為他們繫上專屬球員號的吊牌鎖扣，象徵感恩、榮耀和傳承多重涵義。



圖一、小娟教練感謝大四球員們願意跟著訓練多年，祝福未來持續奮勇向前。

讓球迷睽違已久的義大男籃球迷會終於登場，該活動從「餐旅系」的午餐饗宴開場，邀請師長與球員們品嚐西班牙美食，多位長期默默在背後支持的「一三七」聯盟夥伴也應邀出席；小娟教練感性表示，很感謝校方與各界支持，更感謝球員們願意跟著她多年，她特別請張椀晴(阿布)設計吊牌鎖扣、亞軍項鍊及特製的冠軍戒指，並請師長們為大家戴上，希望球員能抱著感恩的心，在球場與未來持續奮戰。

一如義大球隊風格，球迷們滿腔熱情，卻含蓄不張揚；球隊特別贈送球迷每人一張海報，由球員一一簽名，並特例開放可單獨與球隊大合照；互動遊戲則安排球迷追踩球員腳上氣球，只見一群人包圍球員，廖浩羽以長腿不斷跳躍、陳諾以則機靈跳上隊員背上閃躲，逗趣模樣引來歡笑連連，也留下難忘回憶。

義大男籃隊五位主力球員今年均已大四，未來動向尚在規劃中，隊長徐鈺順於本月底先行前往當兵，呂維誠將如期畢業；教練昨還特別介紹今年大一球員，希望球迷能繼續支持義大男籃，相約今年11月球場上再見！

義大「醫學體感中心」引進全國 首台健身模擬器

玩VR也能健身？全國首台健身模擬器ICAROS，出現在義守大學！包括義大校長陳振遠等多人躍躍欲試，搶先體驗，紛紛表示「比想像中刺激！」也吸引不少師生與外賓駐足觀摩。



圖一、ICAROS 全臺首次曝光，義大校長陳振遠搶先體驗，表示比想像中刺激。

義大「電機資訊學院」延續傳統，每年此時舉辦「電機資訊學院專題成果展」，如今已邁入第19年，在為期3天的展出中，共有18件學生專題成果分享，分別由「電機工程學系」、「電子工程學系」、「通訊工程學系」、「資訊工程學系」與「資訊管理學系」團隊組成，其中ICAROS為現場焦點，也是未來義大跨領域教研先鋒。

「電資學院」院長莊景文表示，為呼應高雄市體感科技園區的前瞻計畫，義大率先引進全國首台健身模擬器ICAROS，透過該設備能增加運動趣味性，結合虛擬實境，融入遊戲體驗，同時達到核心肌群訓練，將成為義大「醫學體感中心」研發的關鍵設備；此外，「電資學院」將攜手「傳播與設計學院」，跨域研發VR虛擬實境，讓運動添趣味，並期待與義大「醫學院」、義大醫院合作，共同發展體感、醫學和運動等多媒體輔具，並延伸健康大數據等應用。

展場中還有多項吸睛展出，包括「資工系」的手機APP操控自走車機器人、「通訊系」的人臉自動辨識器、「電子系」推出奈米銅線薄膜觸控面板，以提高薄膜品質與應用等新趨勢作品；莊景文院長樂見學生透過專題展，展現四年所學，同時凸顯各系所教研特色，更鼓勵學生發揮創意，培養創新思考模式，強化未來在學術或職場的實力。

歡聚「藝術節」 全球各地師生 慕名而來

國際化能量高的義守大學，一年一度「國際文化藝術節」熱鬧開幕，數百位來自全球各地師生不畏風雨，熱情參與；活動主持由菲律賓籍Eugene、宏都拉斯籍Andrea以及本國籍陳儀芳三位同學擔任，數十國學生穿著傳統文化服飾亮相，舉旗進場，洋溢青春，而同時登場的特色文化市集，琳瑯滿目，充滿濃濃異國風，校園彷彿國際村。



圖一、義大國際生們穿著傳統服飾亮相。

此次還有目前在嘉義基督教醫院進行短期見習、來自非洲史瓦帝尼10多位醫生及護理師，特別慕名前來，一睹義大文化饗宴丰采；今年「義術節」延續多元傳統，開幕式中安排義大「觀光學系」李佳玲表演峇里島傳統舞蹈、「金笙盃」亞軍香港學生演唱，以及越南生兼具古典與現代風格舞蹈演出。

義大校長陳振遠熱情參與，並以英文打招呼、致詞，強調校內有來自40多國，2,000名國際生，義大「義術節」一年比一年精采，藉此促進文化交流、相互學習；「國際及兩岸事務處」處長吳岱栖表示，今年「義術節」系列活動更勝以往，以「跨越疆界」為主題，自三月起展開，結合動態與靜態形式，除舉辦「國際運動會」，安排籃球、排球及羽球等競賽，鼓勵學生合作與競技，並於今天舉行「世界青年高峰論壇」，以聯合國永續發展17大議題為主軸，由義大「ISU無國界學生聯盟」代表分享各國民情與因應之道，藉論述拓展、共創更多思維的可能性。

就讀義大IMBA的Andrea指出，在義大就讀認識許多國際生，打開視野，她尤其期待特色創意市集的各國美食；來自聖露西亞與貝里斯的學生也很開心能參與該活動，充分感受到臺灣的好與人的善良；「義術節」將持續至6月9日，特色文化市集明日截止，可上FB義守大學國際文化義術節 ISU Cultural Festival: Across Boundaries」搜尋更多消息。

Study of Al doped ZnO layers inserting CuO nanorods structure to apply on Flexible Transparent Conductive Electrode



Yen-Sheng Lin(林彥勝)*¹, Jhe-Wei Lai(賴哲璋)¹

Fadli Rohman², Joachim Mayer²

Department of Electronic Engineering, I-Shou University

(義守大學電子工程學系)¹

Central Facility for Electron Microscopy, RWTH Aachen University

(德國亞琛工業大學電子顯微鏡研究中心)²

Abstract

In this study, the optimum distribution of the straight CuO nanorods structure inserted in the AZO(Al-doped ZnO) thin film is supposed to be achieved, which has the lowest resistance of $1.25 \times 10^{-3} \Omega\text{-cm}$ and the average transmittance in 400-800nm is about 82%. The best figure of merit for the AZO/CuO nanorods/AZO layer is $1.04 \times 10^{-3} (\Omega^{-1})$.

Due to less Al and Zn diffusion in the interface between seed layer and nanorods, the reduced density of disorder structures in seed layer had been observed by high-resolution transmission electron microscopy (HRTEM), which enhances the formation of more straight nanorods structures. The process as the surface of

AZO seed layer on flexible substrate had been roughed with 50W etching power under 3 minutes, then 20 seconds Cu deposition in Ar/O₂ ambience, the optimum distribution of the straight CuO nanorods structure is formed, which shows the application of AZO thin film with CuO nanorods on soft transparent conductive electrode is viable.

Keywords: Straight CuO nanorods, Aluminum-doped Zinc Oxide (AZO), Transparent Conductive Oxides (TCO), flexible substrate, RF magnetron sputtering.

Introduction

Now, Transparent Conducting Oxides (TCO) is widely used in soft photoelectric devices such as organic light emitting diodes (OLEDs), thin film solar cells, flexible touch sensors and so on [1-6], which is defined to have a transmittance of greater than 80% in the visible range (400nm~800nm) and a resistivity of less than $10^{-3}\Omega\cdot\text{cm}$ [7-10].

Due to the indium is a rare and toxic material, even indium tin oxide (ITO) thin film is currently the most widely used TCO material [11], which could be probably replaced by another new materials in the future[12-17].

One of the new materials is Aluminum-doped ZnO (AZO), which has been the subject of many recent studies [18-22], due to ZnO has a wide band gap (3.2eV) and higher transmittance in the visible range, and it is also cheaper more abundant and non-toxic. But the conductivity is still not enough even after Aluminum-doped, which need to be further improved.

Lots of papers had been reported to embed a metal layer within a dielectric thin film to improve it, such as AZO/Ag/AZO, AZO/Au/AZO and AZO/Fe/AZO, but the transmittance is

also reduced [23-31], due to the metal layer will probably make difference reflection in the visible range and produces a selective transparency [32]. Many studies have concerned to grow nano-metal structures to reduce the reflection [33-35], compared with the grown process, the embedded CuO nanorods structure in AZO thin film has low cost and more readily available [36], which is worth further studying.

During the depositing process, copper has two p-type semiconductors oxides: cuprous oxide (Cu_2O) and cupric oxide (CuO) [37-38]. Due to the CuO phase is more stable and more easily produced than the Cu_2O phase, many deposition techniques are used to synthesize CuO thin film, such as thermal oxidation, hydrothermal electro-deposition, and DC or RF sputtering [39-40].

In this study, the CuO nanorods structure had been again successfully grown after our former research [41], the self-buffer AZO is treated as seed layers and the surface is roughed by different duration and power of plasma etching treatments, which are expected to lead the optimum straight distribution of CuO nanorods structure and also enhance the optoelectronic properties of Al doped

ZnO layers. The microstructures, optical properties and electrical characteristics of various AZO/CuO nanorods /AZO thin films are analyzed, finally the figures of merit for the different treated thin films are calculated.

Experimental

The AZO/CuO nanorods /AZO thin films were deposited on PC flexible substrates using RF magnetron sputtering and the AZO thin film was prepared as a ZnO: Al (2wt.% Al₂O₃) target. The thicknesses of the AZO seed layer and capping layer were fixed about 100 nm and 40 nm, respectively. The mixed O₂/Ar is treated as plasma etching, both quantity is fixed as 50 and 10 sccm.

The etching duration is chosen as 1-7 min and power of plasma etching is designed as 30-90W, and the various Cu deposited time as 10s-40s is chosen in this study. Before deposition, the PC flexible substrate was cleaned in an ultrasonic cleaner with methyl alcohol and DI water.

A diffusion pump coupled with a rotary pump was used to achieve a base pressure of 5×10^{-6} torr. The working pressure was maintained at 70×10^{-3} torr

during the sputtering process. The AZO and Cu targets were cleaned by pre-sputtering with Ar plasma for 10 minutes. The distance between the target and substrate was maintained about 5 cm and the deposition of RF power for AZO layer and Cu was maintained at 50W. The crystallinity and crystal orientation of the thin films were determined by X-ray diffraction (XRD). The morphology of the multilayer thin films and etched surface was determined by field emission scanning electron microscopy (FESEM). The microstructures of AZO/CuO nanorods /AZO thin films were analyzed by High-resolution TEM (HRTEM). The TEM specimens were prepared using a Focused Ion Beam (FIB) (FEI Strata 205) with a tungsten layer deposition for surface protection layer. The milling was performed at an acceleration voltage of 30 kV with current about 30 pA. The cut lamellas were placed onto a molybdenum (Mo) grid for TEM analysis. Transmission electron microscopy (TEM) was performed to obtain the detail of the CuO nanorods structure using TEM FEI Tecnai G2 F20 instrument operated at an accelerating voltage of 200 kV with field-emission gun (FEG) and equipped with energy

dispersive X-Ray (EDX) detector, a Fischione high-angle angular dark field (HAADF) detector and Gatan GIF 2000 Energy-Filter TEM (EFTEM).

High-resolution micrographs were obtained with a point resolution of 0.23 nm, lattice image simulations based on the multi-slice method were performed using the MACTEMPAS software package, for comparison with the experimentally obtained images. HRTEM images were compared with Fast-Fourier Transform (FFT) pattern for processed images to confirm the local orientation of the thin film. The optical transmission was measured using a UV-VIS-NIR spectrophotometer. The electrical resistivity was measured using a Hall characteristic measurement system and the final figure of merit (FOM) of different thin films was calculated.

Results and discussion

Due to the flexible substrate was used in this study, the quantity of Cu to form stable CuO nanorods need to be confirmed. At first, the surface of AZO seed layer is roughed for 3 minutes under O_2/Ar mixed plasma etching and the etching power is fixed as 50W.

Top-view SEM images show the different CuO nano structures on the surface of the AZO seed layers with different Cu deposited time.

The CuO nanorods structure is obviously observed after 20s and 30s Cu deposited time as shown in figure 1(b)(c), and the higher density is observed in 30s deposited time. Only the nano-particles structure is observed in figure 1(a), which means the quantity of Cu should be not enough to form CuO nanorods structure, but it seems too much to form a mixed structures after 40s deposited time as shown in figure 1(d).

After Cu deposition, the resistivity of AZO/CuO nano-structures/AZO layers all reduced to $10^{-3} \Omega\text{-cm}$ except 10s, and the average transmittance spectra of layers for different Cu deposited time is shown in figure 2, the higher average transmittance in visible wavelength range is about 82% after 10s and 20s Cu deposited time, which means proper quantity of Cu will not only improve conductivity but also keep higher transmittance. Depend on this result, the CuO nanorods structure is better for conductivity than nano-particles structure, and more uniform distribution of CuO nanorods

structure seems to play an important role which is proved from SEM images. Depend on different applications of transparent conductive layers, both the optical and electrical properties of the layers are very important, which should be done to approach optimum. But usually the balance between them must be discussed, Haacke [42] proposed a figure of merit Φ_{TC} as $\Phi_{TC} = T^{10}/R_s$ (equation 2) [42] where, Φ_{TC} , T and R_s are the figure of merit (Ω^{-1}), the average transmittance (%) and the sheet resistance (Ω/square) of the layer, respectively.

As shown in figure 3, the conductive properties were measured by a carrier characteristics measurement system and all significantly increased after 20s Cu deposition. Under comparing with transmittance, the maximum figure of merit of $1.04 \times 10^{-3} \Omega^{-1}$ is calculated after 20s Cu deposition, which gives a resistivity as $1.25 \times 10^{-3} \Omega\text{-cm}$ and an average transmittance between 400 nm and 800 nm of 82%. The more detail results about the various Cu deposition time is shown in table 1.

In order to modify various roughed surface to lead the optimum straight

distribution of CuO nanorods structure, the different treatments as etching duration and power are studied. The AFM images of the seed layer after different etching power are shown in figure 4, the more uniform roughed surface is obviously observed in figure 4(b) and also has higher roughness as 55.95 nm. The optimum roughed surface is expected to lead the more uniform straight distribution of CuO nanorods structure, which is not only to enhance conductivity but also to improve transmittance. After the deposition of 20s CuO nanorods and 40nm AZO capping layer, the transmittance spectra of AZO/CuO nanorods /AZO thin films with different etching power of seed layer is shown in figure 5, compare with the other etching power, the higher average transmittance between 400 nm and 800 nm is 82% after 50W treatment, which even reduced to 67% after 90W etching power.

The different etching power is confirmed to make various roughed surface of seed layer and also lead different distribution of CuO nanorods structure. After different etching to rough the surface of seed layer, the optimum 3 min etching duration is also confirmed. Figure 6 shows the top-view

SEM images of different distribution of CuO nanorods structure on the surface of AZO seed layers with various etching duration. The nanorods structure seems to be more straight after 3 min etching duration than the others as shown in figure 6(b), but the lower transmittance is measured as 73% after 1 min etching duration as shown in figure 6(a), which shows most nanorods structure seems to lie down on the surface of seed layer and then the transmittance decreased. In this study, the optimum roughed surface of seed layer should be fabricated with O₂/Ar mixed plasma etching for 3 min duration and 50W etching power, which can efficiently lead 20s Cu to deposit as more uniform and straight CuO nanorods structure.

The more detail of straight and non-straight nanorods structures are observed from Scanning(S) TEM images. Figure 7(a) shows the low magnification of bright-field TEM image, the high magnification of HRTEM images are observed from the inserted white dotted square of (b)(c), which show the crystalline structures of CuO nanorods.

Figure (d)(e) also show the high magnification HRTEM images from the interface between CuO nanorods and

AZO seed layer, the insert shows the main Fast-Fourier Transform(FFT) pattern. The lattice constant for CuO nanorods is measured as 4.68Å and average width of the nanorods is about 40 nm. The amorphous structures as shown in figure 7(b)(c) is formed from tungsten protection layer, which comes from the FIB sample preparation. Lots of different orientations of lattice arrangement as indicated by white arrows are observed from HRTEM image as shown in figure 7(d), which mean higher disorder structures had been formed in the interface between non-straight nanorods and AZO seed layer.

But on the contrary, only few different orientations of lattice arrangement as indicated by white arrows are observed from HRTEM image as shown in figure 7(e) and also has less of FFT pattern taken from that area of the image. Depend on these results, the straight and non-straight nanorods structures seem to be strongly influenced by the interface bonding ability, which means disorder structures will reduce the bonding ability and then easier to form non-straight nanorods structures.

The line-scan elemental profiles on energy dispersive X-ray (EDX) spectra of straight CuO nanorods structure approaching the interface is shown in figure 8(b), which come from the white dotted arrow directed as figure 8(a). A higher quantity distribution of W, C elements are observed due to the protection layer during FIB sample preparation. Compared with Al and Zn, the quantity distribution of Cu, O elements are higher, which means to have less quantity of Al and Zn elements diffuse from AZO seed layer to CuO nanorods and reduce the density of disorder structures as shown in figure 7(e). Depend on the line-scan elemental profiles, the formation of more straight CuO nanorods structure is further confirmed to be influenced by the bonding ability of seed layer, the order structures in interface between CuO nanorods and seed layer play an important role to have a higher bonding ability.

Conclusions

In this study, transparent conducting oxides (TCO) are designed as AZO/ nanorods /AZO layers and deposited on PC flexible substrates

using RF magnetron sputtering. The optimum distribution and more straight of the CuO nanorods structure are achieved when 20 sec Cu is deposited on the surface of AZO seed layer, which is roughed by the 50W plasma etching power in 3 minutes duration. This gives of AZO/CuO nanorods /AZO thin film has the lowest resistance of $1.25 \times 10^{-3} \Omega\text{-cm}$ and the average transmittance in 400-800nm is about 82%. The optimum figure of merit is calculated as $1.04 \times 10^{-3} \Omega^{-1}$, which proves the uniform distribution and more straight of CuO nanorods structure play an important role for the enhancement of conductivity and transmittance of AZO thin films.

Acknowledgements

We gratefully thank Dr. Schwedt Alexander, Mariano Fabian for helpful discussion and SEM measurement, Kistermann Kevin for conducting the HRTEM specimen preparation at Central Facility for Electron Microscopy, RWTH Aachen University, Germany. This work is partially supported by the Ministry of Science and Technology, Taiwan R.O.C., under grant MOST106-2918-I-214-001 and MOST106-2221-E-214-036.

References

- [1] R. Liu, L. Ma, S. Huang, J. Mei, E. Li and G. Yuan, *J. Phys. Chem. C*, 120, 28480-28488 CAS, 2016.
- [2] J. Zhong, Y. Zhang, Q. Zhong, Q. Hu, B. Hu, Z. L. Wang and J. Zhou, *ACS Nano*, 8, 6273-6284, 2014.
- [3] K. Cherenack, C. Zysset, T. Kinkeldei, N. Munzenrieder and G. Troster, *Adv. Mater.*, 22, 5178-5182, 2010.
- [4] Y. Meng, Y. Zhao, C. Hu, H. Cheng, Y. Hu, Z. Zhang, G. Shi and L. Qu, *Adv. Mater.*, 25, 2326-2331, 2013.
- [5] D.R. Sahu, Shin-Yuan Lin, Jow-Lay Huang, *Thin Solid Films*, 516, pp.4728-4732, 2008.
- [6] Joachim Muller, Bernd Rech, Jiri Springer, Milan Vanecek, *Solar Energy*, 77, pp.917-93, 2004.
- [7] Nozomu Tamoto, Chihaya Adachi, and Kazukiyo Nagai., *Chem., Mater.*, 9, pp.1077-1085, 1997.
- [8] Jinhua Huang, Ruiqin Tan, Yulong Zhang, Jia Li, Ye Yang, Xianpeng Zhang, Weijie Song, *J Mater Sci: Mater Electron*, 23, pp.356-360, 2012.
- [9] Tadatsugu Minam, *Thin Solid Films*, 516, pp.5822-5828, 2008.
- [10] C. C. Wu, C. I. Wu, J. C. Sturm, and A. Kah, *American Institute of Physics*, S0003-6951, 00511-1, 1997.
- [11] S. Schonau, F. Ruske, S. Neubert, and B. Rech, *Applied Physics Letters*, 103(19):192108, 2013.
- [12] Andriy Zakutayev, Nicola H. Perry, Thomas O. Mason, David S. Ginley, and Stephan Lany, *Applied Physics Letters*, 103(23):232106, 2013.
- [13] E Fortunato, P Barquinha, and R Martins, *Advanced Materials*, 24(22):2945-86, June 2012.
- [14] Hairen Tan, Rudi Santbergen, Arno H M Smets, and Miro Zeman, *Nano letters*, 12(8):4070-6, August 2012.
- [15] H. Kima, U. A. Pique, J.S. Horwitz, H. Murata, Z.H. Kafafi, C.M. Gilmore, D.B. Chrise, *Thin Solid Films*, 377, pp.798-802, 2000.
- [16] Traci R. Jensen, Michelle L. Duval, K. Lance Kelly, Anne A. Lazarides, George C. Schatz, and Richard P. Van Duyne, *J. Phys. Chem. B*, 103, pp.9846-9853, 1999.

- [17] D.R. Sahu, Shin-Yuan Lin, Jow-Lay Huang, Thin Solid Films, 516, pp.4728-4732, 2008.
- [18] Hyun-Jin Cho, Kyung-Woo Park, Jun-Ku Ahn, Nak-Jin Seong, Soon-Gil Yoon, Won-Ho Park, Sung-Min Yoon, Dong-Jun Park, and Jeong-Yong Lee, Journal of The Electrochemical Society, 156 (8), pp.215-220, 2009.
- [19] S. Sutthana, N. Hongstith, S. Choopun Current, Applied Physics, 10, pp.813-816, 2010.
- [20] T. Dimopoulos, G.Z. Radnoczi, B. Pécz, H. Brückl, Thin Solid Films, 519, pp.1470-1474, 2010.
- [21] L.S. Wang, Y.Z. Chen, G.H. Yue, H.D. She, X.H. Luo, D.L. Peng, Applied Surface Science, 255, pp.2545-2549, 2008.
- [22] L. Huang, B. Li, N. Ren, Ceram. Int. 42, 7246, 2016.
- [23] C.H. Lee, K. Bae, I.H. Jin, H.M. Kim, S.Y. Sohn, J. Korean Phys.Soc. 67, 1007, 2015.
- [24] Z. Demircioglu, E. Ozkol, H. Nasser, R. Turan, Phys. Status Solidi C 12, 1215, 2015.
- [25] S. Fernández, J.D. Santos, C. Munuera, M. García-Hernández, F.B. Naranjo, Sol. Energy Mater.Sol. Cells 133, 170, 2015.
- [26] C.C. Hu, T.W. Lu, C.Y. Chou, J.T. Wang, H.H. Huang, C.Y. Hsu, Bull. Mater. Sci. 37, 127, 2014.
- [27] R.G. Waykar, A.S. Pawbake, R.R. Kulkarni, A.A. Jadhavar, A.M. Funde, V.S. Waman, H.M. Pathan, S.R. Jadhkar, J. Mater Sci. Mater. Electron. 27, 1134, 2016.
- [28] Tianlin Yang, Zhisheng Zhang, Shumei Song, Yanhui Li, Maoshui Lv, Zhongchen Wu, Shenghao Han, Vacuum, 83, pp.257-260, 2009.
- [29] Shumei Song, Tianlin Yang, Maoshui Lv, Yanhui Li, Yanqing Xin, Lili Jiang, Zhongchen Wu, Shenghao Han, Vacuum, 85, pp.39-44, 2010.
- [30] Y.P. Wang, J.G. Lu, X. Bie, Z.Z. Ye, X. Li, D. Song, X.Y. Zhao, W.Y. Ye, Applied Surface Science, 257, pp.5966-5971, 2011.
- [31] C. H. Xu, C. H. Woo and S. Q. Shi, "Formation of CuO Nanowires on Cu Foil," Chemical Physics Letters, Vol. 399, No. 1-3, pp. 62-66, 2004.
- [32] F. Gao, X.-J. Liu, J.-S. Zhang, M.-Z. Song, N. Li, J Appl

- Phys,111(8), 084507, 2012.
- [33] S.-L. Cheng, M.-F. Chen, Nanoscale Res Lett 7(1), 1, 2012.
- [34] P. Samarasekara, N. Kumara, N.J. Yapa, Phys Condens Matter, 18(8), 2417, 2006.
- [35] P. Chand, A. Gaur, A. Kumar, Superlattices Microstruct 60, 129, 2013.
- [36] M. Abaker, A. Umar, S. Baskoutas, S. Kim, S. Hwang, J Phys D, Appl Phys 44(15), 155405, 2011.
- [37] N. Serin, A. Yildiz, E. C. am, S. . Uzun, T. Serin, Superlattices, Microstruct 52(4), 759, 2012.
- [38] V. Dhanasekaran, T. Mahalingam, R. Chandramohan, J.-K. Rhee, J. Chu, Thin Solid Films 520(21), 6608, 2012.
- [39] Anita Sagadevan Ethiraj and Dae Joon Kang, Nanoscale Res Lett. ; 7(1): 70, 2012.
- [40] V. Dhanasekaran, T. Mahalingam, R. Chandramohan, J.-K. Rhee, J. Chu, Thin Solid Films 520(21), 6608, 2012.
- [41] Y.S. Lin, Y. H. Huang, W. C. Huang, Vacuum, vol. 122, pp. 143-146, 12, 2015.
- [42] Haacke G, J. Appl. Phys, 47, pp.4086-4089, 1976.

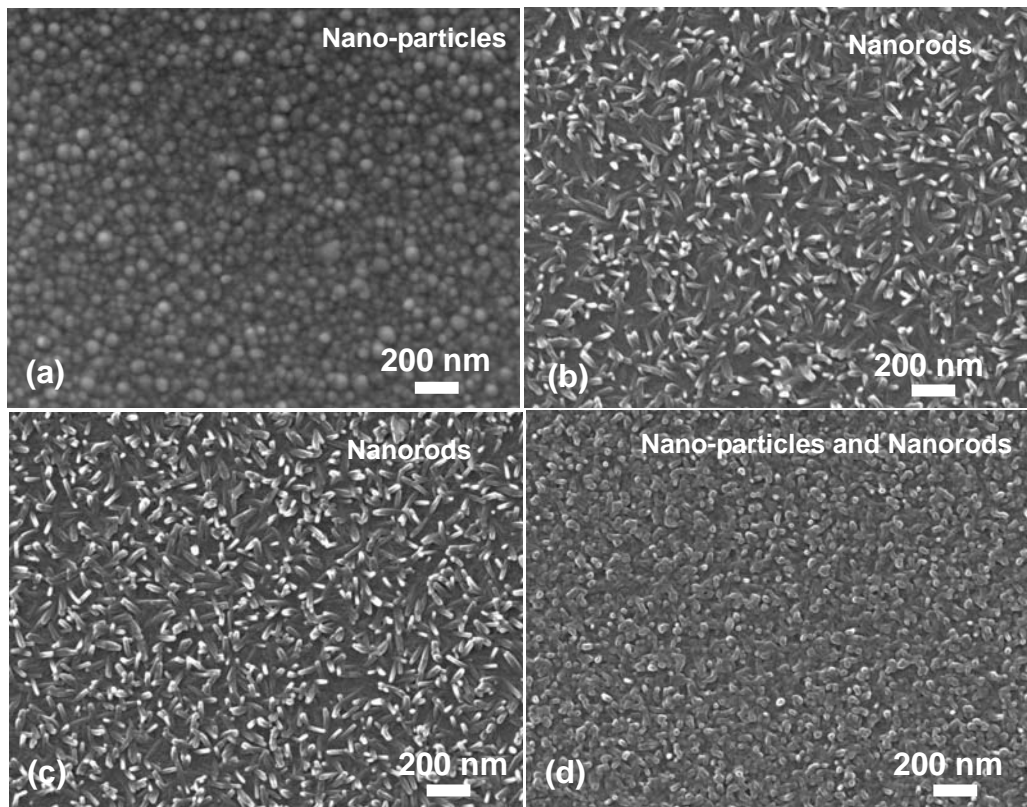


Figure 1. Top-view SEM images of CuO nano-particles to nanorods on the surface of AZO seed layers with different Cu deposited time of (a) 10s (b) 20s (c) 30s (d) 40s.

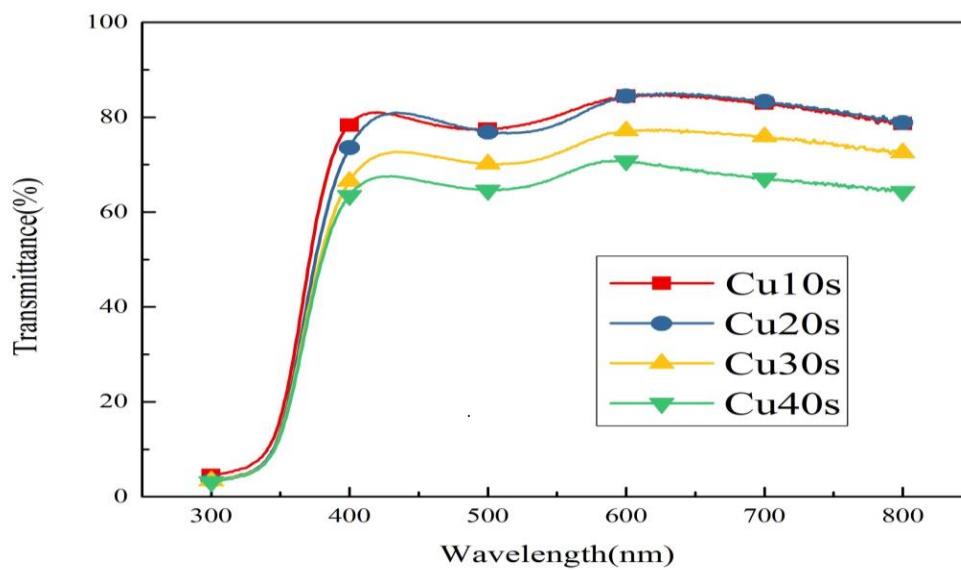


Figure 2. The average transmittance spectra for AZO/CuO nano-structures/AZO layers with different Cu deposited time.

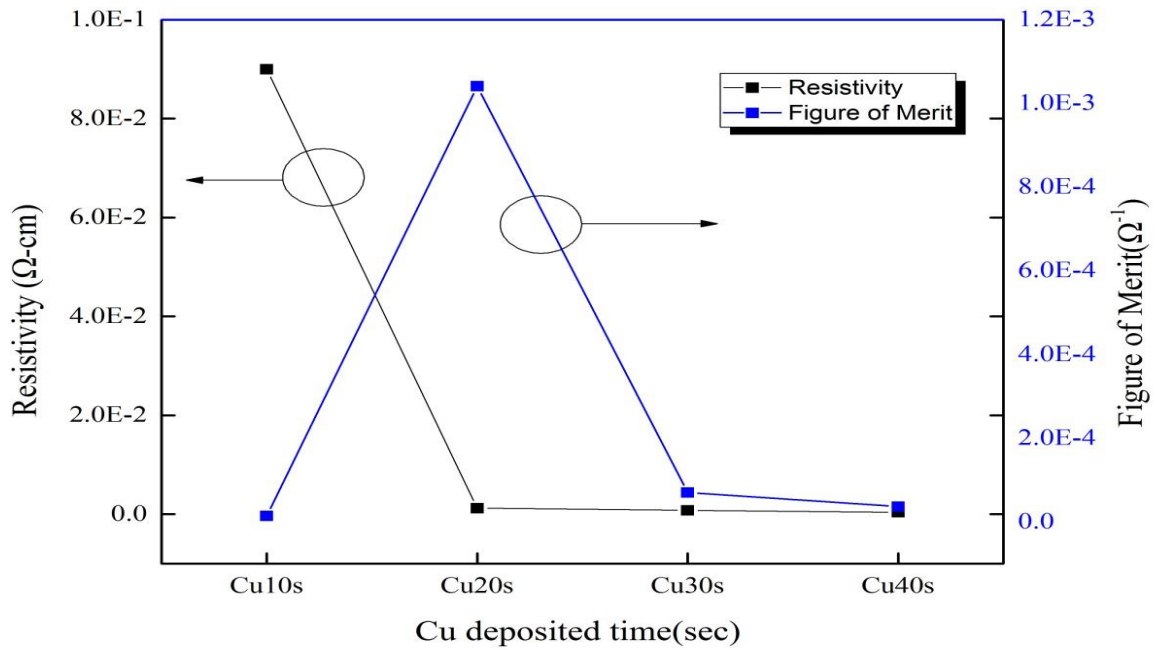


Figure 3. The FOM and resistivity for AZO/CuO nano-structures/AZO with different Cu deposition time.

Table 1. The optoelectronic property of AZO/CuO nanorods /AZO with different Cu deposition time.

Cu deposition	10s	20s	30s	40s
Resistivity (Ω-cm)	8.99E-2	1.25E-3	7.91E-4	3.96E-4
Carrier Concentration (cm ⁻³)	1.285E+19	-5.962E+19	-4.908E+20	-1.343E+21
Mobility (cm ² /Vs)	5.399E+00	8.430E+01	1.607E+01	1.171E+01
Transmittance (%)	81	82	73	67
FOM (Ω ⁻¹)	1.38E-5	1.04E-3	7.01E-5	3.64E-5

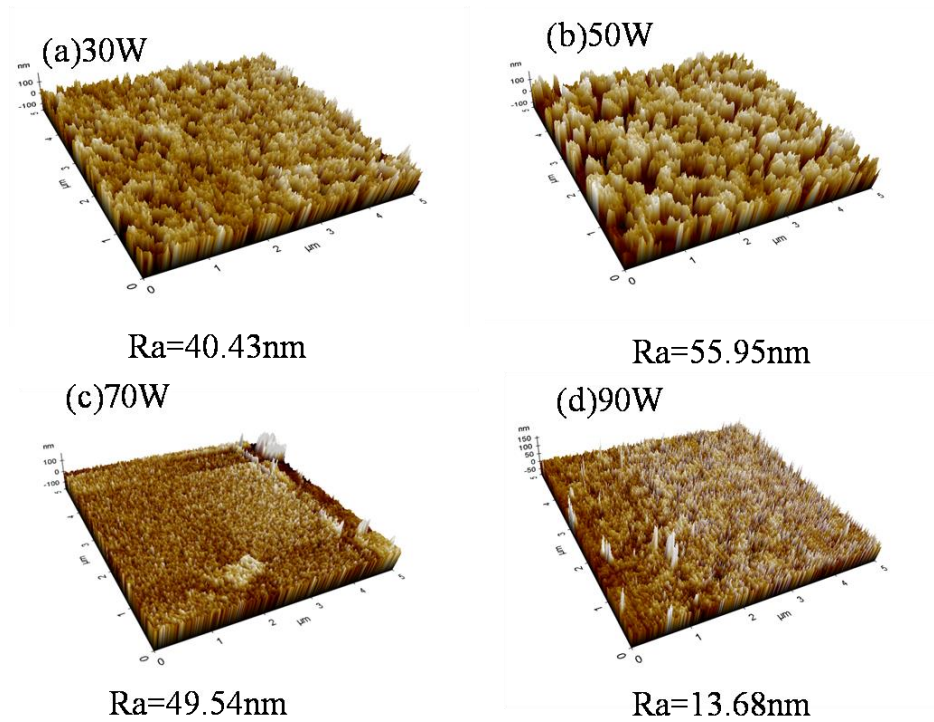


Figure 4. The AFM images of the seed layer after different etching power.

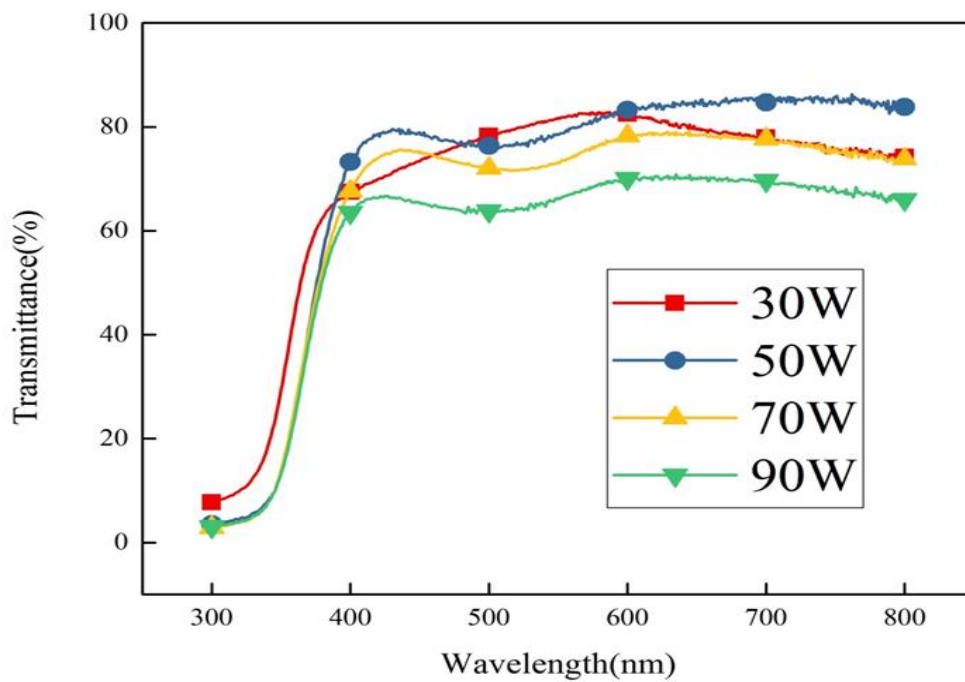


Figure 5. The transmittance spectra of AZO/CuO nanorods /AZO layer with different etching power on the surface of AZO seed layer.

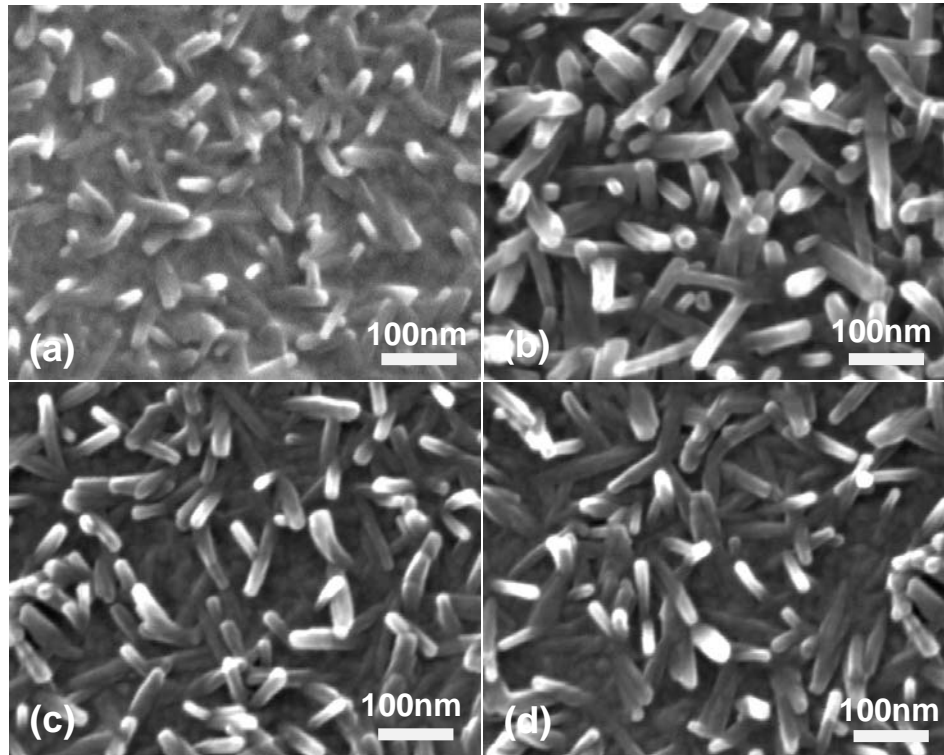


Figure 6. Top-view SEM images of CuO nanorods structure on the surface of AZO seed layers with different etching duration (a) 1min (b) 3min (c) 5min (d) 7 min.

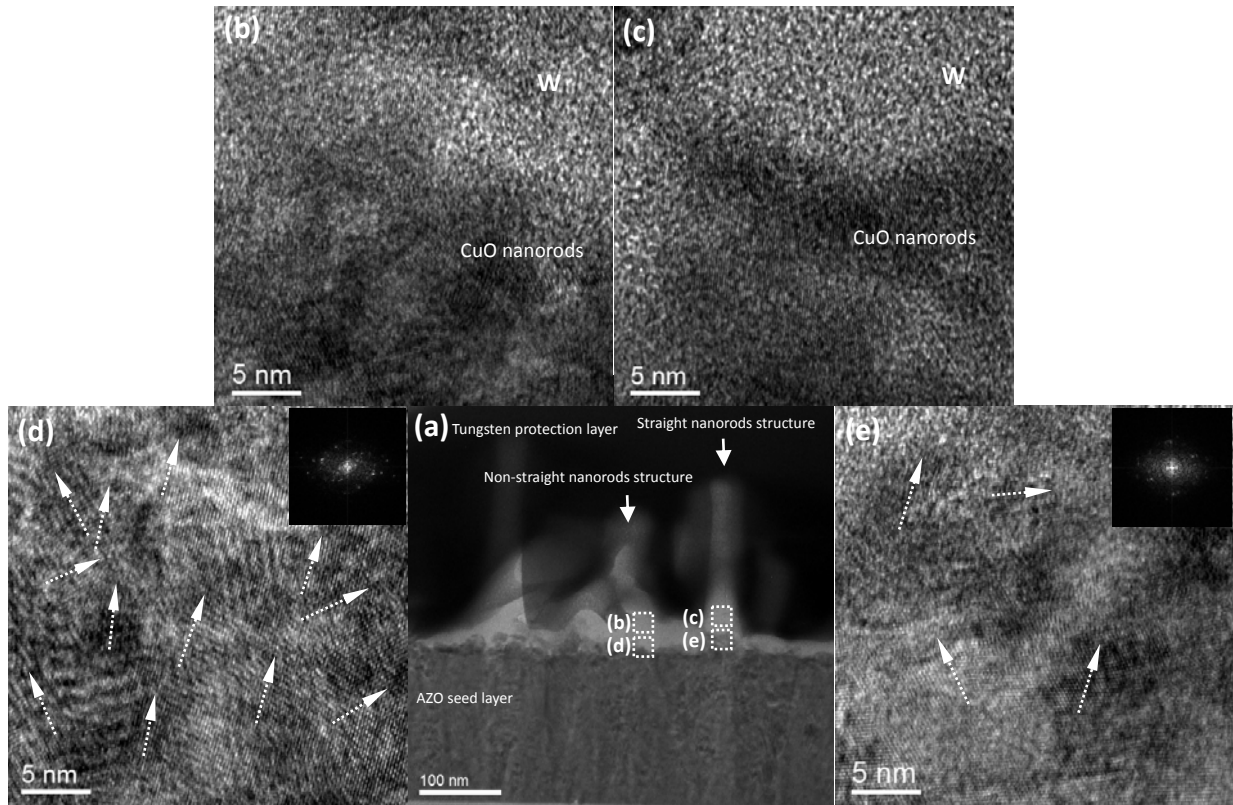


Figure 7. (a) The low magnification of bright-field (S)TEM image of straight and non-straight CuO nanorods structures. (b)(c) The high magnification of the inserted white dotted line from (a) which shows the crystalline structure of nanorods. (d)(e) The high magnification of the inserted white dotted line from (a) which shows the interface between CuO nanorods and AZO seed layer, the insert shows the main Fast-Fourier Transform (FFT) pattern.

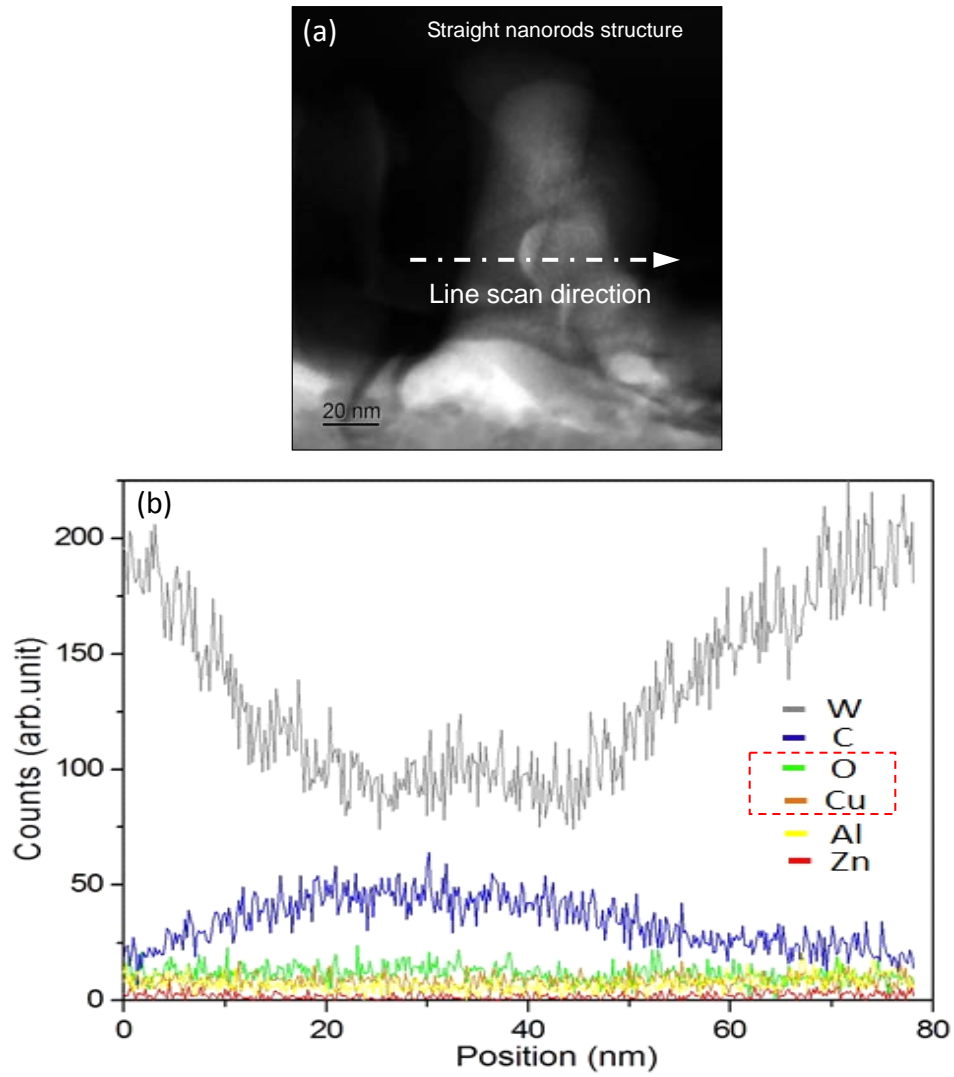


Figure 8. (a) The low magnification of bright-field (S)TEM image for straight CuO nanorods structure, the EDX line scan direction is shown as the white array dotted line. (b) The EDX line scan profile of different chemical composition.

The effect of Botox injection compared with usual therapy on activity in children with cerebral palsy: a systematic review



Yin-Tzu Hsieh¹, Chrysostomos Panou²
Hsiu-Ching Chiu³, Theofani Bania⁴

Department of Physical Therapy, I-Shou University¹
Department of Physical Therapy, TEI of Western Greece²
Associate Professor, Department of Physical Therapy, I-Shou University³
Lecturer, Department of Physical Therapy, TEI of Western Greece⁴

Abstract

1.Purpose:

The aim of this review aims to summarize results of studies that compare intervention of Botulinum toxin type A (BTX-A) injections with usual physical therapy.

2.Method:

MEDLINE and PEDro databases were searched for randomized controlled trials. Studies of randomized controlled trials (RCTs) were included if the participants were children (< 18 years old) with spastic cerebral palsy, who underwent an intervention of BTX-A injection. Measures that best reflected the body structure and function and activity were used in the report.

3.Results:

Three RCTs were included (60 participants). At post-intervention, one RCT only demonstrated statistically important result between the experimental and control group for Modified Ashworth Scale (mean difference: -0.7, $p = 0.002$) and Gross Motor Function Measure (mean difference: 11.14, $p = 0.03$). The rest RCTs showed no statistically significant differences between groups, although some statistically significant with group differences were found for the experimental group.

4.Conclusion:

This review provides only some preliminary evidence that BTX-A can

decrease spasticity and increase gross motor function in children with spastic cerebral palsy. High quality randomized trials on current and focused interventions related to physical therapy are needed in the future.

Introduction

Cerebral Palsy (CP) is the term most commonly used to describe children with disorders of posture and movement occurring from a lesion in the immature brain[1]. Cerebral palsy is always accompanied with a variety of impairments involving neuromuscular, musculoskeletal and sensory systems which may directly or indirectly result from the existing pathology[2]. Spasticity is a common and very complicated phenomenon in children with cerebral palsy, that has been defined as “a motor disorder characterized by a velocity-dependent increase in tonic stretch reflexes (muscle tone)” [3].

Botulinum toxin type A (BTX-A) is a serotype of botulinum toxin, produced by the Gram-positive bacterium *Clostridium botulinum* [5]. The clinical effect of BTX-A when injected in a muscle is decreased

activation of that muscle. In particular, BTX-A binds and internalizes itself at the presynaptic cholinergic nerve terminals. The purpose of this action is to inhibit the release of acetylcholine at the neuromuscular junction. If acetylcholine is not released the muscle tends to be functionally denervated, atrophy, and produce extra junctional acetylcholine receptors. Normally, the muscle gradually recovers as soon as new axon terminals sprout and form new synapses to contact the adjacent muscle fibers [6]. A main benefit of botulinum toxin A is treatment of local or segmental dystonia. Over the last 20 years, BTX-A has also been used to treat strabismus and muscle spasticity. Considering how often spasticity is observed in children with cerebral palsy and that it limits their ability to move, stand and walk, it is important to look at the effect of BTX-A in these children. This critical review examines the recent literature on the effect of BTX-A injections into muscles of children with muscle spasticity.

Although there were some clinical trials showing the efficacy of BTX-A injections with additional physiotherapy in children with cerebral palsy [13, 14, 15, 16], especially in the

gastrocnemius muscle, information about BTX-A injections without additional therapies was not clear. Therefore, the research question for this systematic review was “Does BTX-A injection alone improve activity and reduce spasticity in children with cerebral palsy?”

Methods

Identification and selection of studies

Searches were conducted of MEDLINE (1966 to May 2019), PUBMED (1966 to May 2019) and PEDro (1966 to May 2019) databases, with language in English using keywords related to Botox and cerebral palsy. Studies were included if were randomized controlled trials with participants children with cerebral palsy (under 18 years of age) that had received Botox-A injection The control group of the studies had to have received only other usual therapy such as splinting. Outcome measurements analyzed were body and function and activity outcomes (Table 1).

Table 1 Inclusion criteria

Design

- RCT
- BTX-A injection versus usual therapy (both group or only control group received splinting or usual therapy)

Participants

- Children, i.e., <18 years old
- Spastic cerebral palsy
- Any level of GMFCS

Intervention

- BTX-A injection to lower extremities

Outcome measures

- Outcome measures of body structure and function, ie, muscle tone
- Outcome measures of activity, ie, gait speed or gross motor function

*BTX-A = Botulinum Toxin A,
GMFCS = Gross Motor Function Classification System, RCT = Randomized Controlled Trial

Assessment of characteristics of studies

Quality

The quality of included studies was assessed by extracting PEDro scores from the PEDro website (<https://www.pedro.org.au/>).

Participants

Studies involving children with cerebral palsy of either gender, regardless of the level of initial disability were included.

Intervention

The experimental group had to receive BTX-A injection. The control group had to receive other intervention, such as exercises or splinting. Both groups of participants could have received usual therapy.

Outcome Measures

Measures that best reflected the body structure & function and activity trained were used in the report.

Data analysis

Information about the method (i.e., design, participants, intervention, measures) and outcome data (i.e., number of participants and mean (SD) of outcomes) were extracted. We calculated the mean difference (% difference) for each study and presented the between baseline and post training analysis reported as following formula.

$$\frac{(\text{Post-Pre}) \text{ Exp} - (\text{Post-Pre}) \text{ Con}}{(\text{Base Exp} + \text{Base Con})/2}$$

Results

Flow of studies through the review

The search strategy identified 533 studies. After screening titles and abstracts, 39 full papers were retrieved. After full texts were read and assessed against the inclusion criteria, three randomized controlled trials were included in the review. See the Figure 1 for the flow of studies through the review.

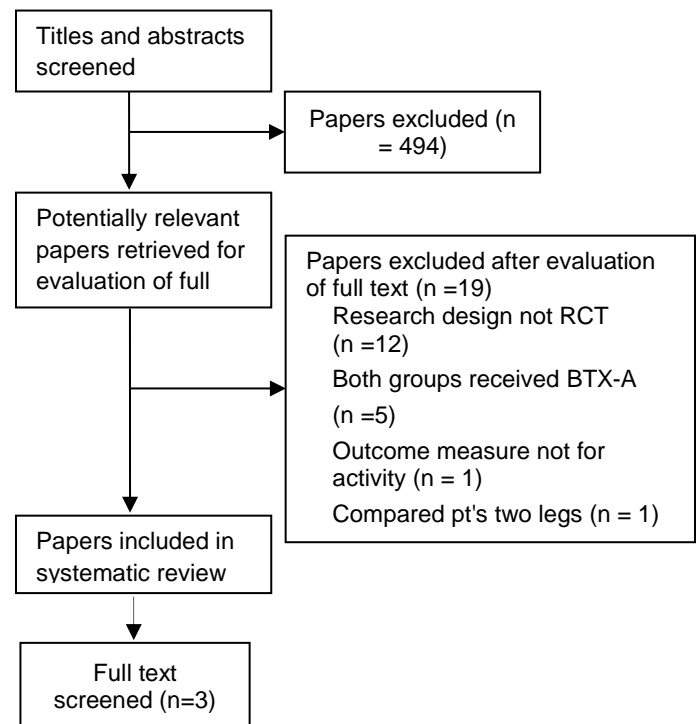


Figure 1. Flow of studies through the review.

Characteristics of Included Studies

Three studies that compared BTX-A injection with another usual intervention were included in the review [17, 18, 19].

Quality

The mean PEDro score of the papers was 5.5 (range 4 to 7) (Table 2). In the majority of the papers: participants were randomized (100%), between-group difference was reported (100%), point estimates and variability were reported (100%), had similar groups at baseline (100%), and had blinded assessors (67%). On the other hand, the majority of studies did not carry out an intention-to-treat analysis (100%), did not blind participants or therapists (100%), reported < 15% loss at follow-up (67%) and did not conceal the allocation list (67%).

Table 2 PEDro scores for included papers (n = 3)

Study	Random allocation	Concealed allocation	Groups		Therapist blinding	Assessor blinding	<15% dropouts	Intention -to-treat analysis	Between-group difference reported	Point estimate and variability reported	Total (0 to 10)
			similar at baseline	Participant t blinding							
Corry et al (1998)	Y	N	Y	N	N	Y	N	N	Y	Y	5
Flett et al (1999)	Y	Y	Y	N	N	Y	Y	N	Y	Y	7
Hazneci et al (2006)	Y	N	Y	N	N	N	N	N	Y	Y	4

Participants

Three studies investigated children and adolescents with the mean age of participants ranging from 4.6 to 8.8 years. Participants were of GMFCS level from I to III. Summary of the characteristics of the studies is presented in Table 3.

Intervention

The experimental group received Botox injection in the lower extremities. Two studies had BTX-A in the gastrocnemius and one study had BTX-A in the hip adductors and hamstrings. The control group received various splinting methods, i.e., stretching cast, fixed plaster casting and Johnstone pressure splints (Table 3).

Measures

Body structure and function was measured using the Modified Ashworth Scale and activity was measured using the Gross Motor Function Measure (GMFM) and the Physician Rating Scale (PRS).

Table 3 Characteristics of the studies (n = 3)

Study	Design	Participants	Intervention	Outcome Measures
Corry et al [19]	RCT	n=20 Mean age (range) = 4.6yr(2-9) Classification = spastic cerebral palsy GMFCS = III	Exp = BTX-A Muscle/Dose: -gastrocnemius: 6-8 U/kg -soleus :6-8 U/kg Con = Stretching cast (4-6 wks)	Activity: PRS (score) week = 0, 2, 12
Flett et al [17]	RCT	n=20 Mean age (range) = 3.71yr(2-8) Classification = spastic cerebral palsy GMFCS = I-III	Exp = BTX-A Muscle/Dose: -gastrocnemius: 4-8 U/kg Con = Fixed plaster casting (reapplication at 2 wks, removed at 4 wks)	Body structure and function: MAS (grade) Activity: GMFM (%) week = 0, 8, 16, 24
Hazneci et al [18]	RCT	n=20 Mean age (range) = 8.78yr Classification = spastic diplegia cerebral palsy	Exp = BTX-A Muscle/Dose: -hip adductors -medial hamstrings (Total of 322 IU of BTX-A was injected) Con = JPS (30 min/session, 3 days/wk) Both = BNDEs (3 days/wk)	Body structure and function: MAS (grade) Activity: GMFM (%) week = 0, 12

*BNDE = Bobath neurodevelopmental exercises, BTX-A = Botulinum toxin A, Con = Control group, Exp = Experimental, GMFCS = Gross Motor Function Classification System, GMFM = Gross Motor Function Measure, JPS = Johnstone Pressure Splints, MAS = Modified Ashworth Scale, PRS = Physician Rating Scale, RCT = Randomized Controlled Trial.

Effect of BTX-A injection versus splinting

Body structure and function

The immediate effect of BTX-A injection compared with splinting on body structure and function was examined by MAS from 2 comparisons with a PEDro score of 5.5 and 40 participants. The results show that BTX-A injection decreased spasticity (Modified Ashworth Scale mean difference: -0.7, $p=0.002$) (Percentage change = -25%) compared with splinting in one of these studies [18]. The other RCT demonstrated no significant difference between groups [17] (Table 4).

Activity

The immediate effect of BTX-A injection compared with splinting on activity was measured using GMFM and PRS from 3 comparisons with a PEDro score of 5 and 60 participants. One RCT only showed that children in the group with BTX-A injection increased GMFM (mean difference: 11.14, $p= 0.03$) (Percentage change = 32%) compared with control group [18] (Table 4). The other two RCT's showed that children of the experimental group (BTX-A injection) did not improve PRS or GMFM (Percentage change = -25%, -2%) in comparison with control group [17, 19] (Table 4).

Table 4 Within group and between groups effect on motor function and spasticity after BTX-A injection (n = 3)

Study	Outcome measure	Mean difference within group/	Significance of the difference within experimental group	Percentage change (EXP comparison with CON)
Corry et al (1998)	PRS	0/(SD=NA)	$P = 0.006$	-25% (P = NA)
Flett et al (1999)	GMFM	6.41/(SD=NA)	$P < 0.01$	-2% (P = NA)
	MAS	-1.01/ (SD=NA)	$P < 0.01$	-3% (P = NA)
Hazneci et al (2006)	GMFM	-13.55/(SD=8.66)	$P < 0.001$	32% (P = 0.03)
	MAS	1.18/(SD=0.59)	$P < 0.001$	-25% (P = 0.002)

*CON = control group, GMFM = Gross Motor Function Measure, MAS = Modified Ashworth Scale, PRS = Physician Rating Scale, Only significant p values are reported.

Discussion

This narrative review reported the results from 3 RCTs that implemented BTX-A injection to children with cerebral palsy. All articles were published before 2006. The results of the review support preliminary evidence of the effectiveness of BTX-A in spasticity and gross motor function of children with cerebral palsy.

The Hazneci et al [18] study only found statistically significant differences between the experimental and control group in MAS and GMFM at post-intervention. In this study adductors and hamstrings were injected, while in the other 2 studies that did not find positive results gastrocnemius was injected. Also, the study of Hazneci et al [18] included older children compared with the studies of Corry et al and Flett et al [17] that included very small children. Therefore, a reason that these latter studies did not show any improvement in spasticity or gross motor function after the BTX-A application might be that younger children could not comply with instructions following the BTX-A such as positioning or avoiding certain activities. The fact that in the study of

Hazneci et al [18] the children were older and could comply with instructions after the BTX-A might helped these children to show improvements. Additionally, the children in this study continued after the application of BTX-A with neurodevelopmental exercises that may also helped them to improve.

The PEDro scale score for each of these three studies was 5, 7, and 4 [17, 18, 19]. Considering the PEDro score, this review was based on randomized trials of low to high quality. Given that 5 is moderate PEDro score achievable, because it is not possible to blind the therapists or participants during complex interventions such as BTX-A injection, the mean PEDro score of 5 for the papers included in this review suggested that the findings were relatively credible. In addition, most studies demonstrated within experimental group positive differences either in spasticity (MAS) or activity (GMFM). Although this is a good effect, we cannot support high evidence of the effectiveness of the BTX-A in spasticity and activity of children with spastic cerebral palsy because statistically significant differences between groups are

required to have been reported in the studies.

Although BTX-A is an excellent treatment to decrease muscle spasticity, its main limitation is the relatively short duration of its action. The average reinjection interval for blepharospasm in the published literature is between two and three months [21]. Compared to the studies [13, 14, 15, 16], only one of the studies included in our review had significant improvements in GMFM and no study in PRS. The reason may also be that BTX-A injection without been followed by exercise could not improve gait and gross motor function.

This review generates an implication for clinical practice with children with spastic cerebral palsy. BTX-A injection is an effective way to decrease spasticity at the body structure and function level. Given that the same dose of intervention without exercise is likely to result in decreases in spasticity. However, BTX-A combined with Bobath neurodevelopmental exercises is likely to result in decreases in spasticity but also in increases in gross motor function. Ultimately, the combination of BTX-A injection and Bobath

neurodevelopment exercise would be more effective and could be a choice in the future.

Conclusions

Three studies were included in this review examining the efficacy of BTX - A in terms of decreasing spasticity and increasing gross motor abilities in children with spastic cerebral palsy. This review provides only some preliminary evidence that BTX-A injection can decrease spasticity and increase gross motor function. Further, BTX-A combined with Bobath neurodevelopmental exercises seems to have better results in spasticity or gross motor function in children with spastic cerebral palsy. High quality randomized trials on current and focused interventions related to physical therapy are needed in the future.

References

- [1] Rosenbaum, P., Paneth, N., Leviton, A., Goldstein, M., Bax, M., Damiano, D., & Jacobsson, B. (2007). A report: the definition and classification of cerebral palsy April 2006. Developmental

- medicine and child neurology. Supplement, 109, 8-14.
- [2] Koman, L. A., & Smith, B. P. en Shilt, JS (2004) Cerebral palsy. The Lancet, 363, 1619-163.
- [3] Braun, K. V. N., Doernberg, N., Schieve, L., Christensen, D., Goodman, A., & Yeargin-Allsopp, M. (2016). Birth prevalence of cerebral palsy: a population-based study. Pediatrics, 137(1), 1.
- [4] Bjornson, K., Hays, R., Graubert, C., Price, R., Won, F., McLaughlin, J. F., & Cohen, M. (2007). Botulinum toxin for spasticity in children with cerebral palsy: a comprehensive evaluation. Pediatrics, 120(1), 49.
- [5] Dressler, D., & Saberi, F. A. (2005). Botulinum toxin: mechanisms of action. European neurology, 53(1), 3-9.
- [6] Arnon, S. S., Schechter, R., Inglesby, T. V., Henderson, D. A., Bartlett, J. G., Ascher, M. S., & Lillibridge, S. (2001). Botulinum toxin as a biological weapon: medical and public health management. Jama, 285(8), 1059-1070.
- [7] Cosgrove, A. P., & Graham, H. K. (1994). BOTULINUM TOXIN A PREVENTS THE DEVELOPMENT OF CONTRACTURES IN THE HEREDITARY SPASTIC MOUSE. Developmental Medicine & Child Neurology, 36(5), 379-385.
- [8] Yana, M., Tutuola, F., Westwater-Wood, S., & Kavlak, E. (2019). The efficacy of botulinum toxin a lower limb injections in addition to physiotherapy approaches in children with cerebral palsy: A systematic review. NeuroRehabilitation, (Preprint), 1-15.
- [9] Wong, V. (2003). Evidence-based approach of the use of botulinum toxin type A (BTX) in cerebral palsy. Pediatric rehabilitation, 6(2), 85-96.
- [10] Nolan, K. W., Cole, L. L., & Liptak, G. S. (2006). Use of botulinum toxin type A in children with cerebral palsy. Physical therapy, 86(4), 573-584.
- [11] Balaban, B., Tok, F., Tan, A. K., & Matthews, D. J. (2012). Botulinum toxin a treatment in children with cerebral palsy: its effects on walking and energy expenditure. American journal of

- physical medicine & rehabilitation, 91(1), 53-64.
- [12] Jongerius, P. H., van den Hoogen, F. J., Limbeek, J. V., Gabreëls, F. J. M., Hulst, K. V., & Rotteveel, J. J. (2004). Effect of botulinum toxin in the treatment of drooling: a controlled clinical trial.
- [13] Xu, K., Yan, T., & Mai, J. (2009). A randomized controlled trial to compare two botulinum toxin injection techniques on the functional improvement of the leg of children with cerebral palsy. *Clinical rehabilitation*, 23(9), 800-811.
- [14] Tedroff, K., Löwing, K., Haglund-Åkerlind, Y., Gutierrez-Farewik, E. M., & Forssberg, H. (2010). Botulinumtoxin A treatment in toddlers with cerebral palsy. *Acta paediatrica*, 99(8), 1156-1162.
- [15] Chaturvedi, S. K., Rai, Y., Chourasia, A., Goel, P., Paliwal, V. K., Garg, R. K., ... & Gupta, R. K. (2013). Comparative assessment of therapeutic response to physiotherapy with or without botulinum toxin injection using diffusion tensor tractography and clinical scores in term diplegic cerebral palsy children. *Brain and Development*, 35(7), 647-653.
- [16] Liu, J. J., Ji, S. R., Wu, W. H., Zhang, Y., Zeng, F. Y., & Li, N. L. (2014). The relief effect of botulinum toxin-a for spastic iliopsoas of cerebral palsy on children. *Eur Rev Med Pharmacol Sci*, 18(21), 3223-3228.
- [17] Flett PJ, Stern LM, Waddy H, Connell TM, Seeger JD, and Gibson SK (1999). Botulinum toxin A versus fixed cast stretching for dynamic calf tightness in cerebral palsy. *J. Paediatr. Child Health*, 35, 71-77.
- [18] Hazneci Maj Bulent, Tan Col Arif Kenan, Guncikan Maj Mustafa Nuri, Dincer Col Kemal, and Kalyon Col Tunc Alp (2006). Comparison of the Efficacies of Botulinum Toxin A and Johnstone Pressure Splints against Hip Adductor Spasticity among Patients with Cerebral Palsy: A Randomized Trial. *MILITARY MEDICINE*, (171).
- [19] Corry I. S., Cosgrove A. P., Duffy C. M., Taylor T. C., and Graham H. K. (1998). Botulinum Toxin A Compared with Stretching Casts

in the Treatment of Spastic Equinus: A Randomised Prospective Trial. *Journal of Pediatric Orthopaedics*, 18, 304-311.

[20] Pingel Jessica, Nielsen Mikkel Schou, Lauridsen Torsten, Rix Kristian, Bech Martin, Alkjaer Tine, Anderen Ida Torp, Nielsen Jens Bo, & Feidenhansl R. (2017) Injection of high dose botulinum-toxin A leads to impaired skeletal muscle function and damage of the fibrillar and non-fbrillar structures. *Scientific Reports*, 7.

[21] Andrew R. Harrison, Zachary Berbos, Renzo A. Zaldivar, Brian C. Anderson, Mollie Semmer, Michael S. Lee, and Linda K. McLoon (2011). Modulating Neuromuscular Junction Density Changes in Botulinum Toxin-Treated Orbicularis Oculi Muscle, 52, 2.

Appendix

Search strategy

Databases

Medline (1966 to April 2017) and Pubmed (1966 to April 2017).

The search of the databases was using the terms as follows:

- 1.cerebral pals\$.mp.
- 2.hemiplegia.mp. or Hemiplegia/.
- 3.quadriplegia.mp. or Quadriplegia/.
- 4.hemiplegi\$.mp.
- 5.monoplegia.mp.
- 6.triplegia.mp.
- 7.quadriplegi\$.mp.
- 8.1 or 2 or 3 or 4 or 5 or 6 or 7.
- 9.randomized controlled trial.pt.
- 10.randomized controlled trials.mp. or Randomized Controlled Trial/.
- 11.controlled clinical trials.pt.
- 12.controlled clinical trial.pt.
- 13.random allocation.mp. or Random Allocation/.
- 14.single-blind method.mp. or Single-Blind Method/.
- 15.clinical trial.pt.
- 16.exp clinical trial/.
- 17.(clin\$ adj5 trial\$.mp. [mp=title, original title, abstract, name of substance word, subject heading word].
- 18.(single adj5 (blind\$ or mask\$)).mp. [mp=title, original title, abstract, name of substance word, subject heading word].
- 19.placebo\$.mp. or Placebos/.
- 20.random\$.mp.

- 21.research design.mp. or Research Design/.
- 22.multicenter study.pt.
- 23.intervention studies.mp. or Intervention Studies/.
- 24.cross-over studies.mp. or Cross-Over Studies/.
- 25.control\$.tw.
- 26.alternate treatment.tw.
- 27.latin square.tw.
- 28.comparative Study/.
- 29.exp evaluation studies/.
- 30.follow-up studies.mp. or Follow-Up Studies/.
- 31.prospective studies.mp. or Prospective Studies/.
- 32.prospective.tw.
- 33.counterbalanc\$.tw.
- 34.versus.tw.
- 35.or/9-34
- 36.muscle spasticity/ or muscle hypertonia/ or muscle rigidity/ or muscle tonus/.
- 37.spasm/ or dystonia/ or paraparesis, spastic/.
- 38.(spastic\$ or high tone).tw.
- 39.(muscle\$ adj5 (spasm or rigid\$ or tone or tonus or hyperton\$ or hypermyoton\$ or dyston\$ or contracture\$)).tw.
- 40.or/36-39.
- 41.exp botulinum toxins/ or exp phenols/ or ethanol/ or injections, intramuscular/ or nerve block/.
- 42.(botulinum\$ or botulin or botox or BoNT\$ or BTX\$ or disport or xeomin or myobloc or neurobloc or oculinum or onabotulinum\$ or abobotulinum\$ or incobotulinum\$ or rimabotulinum\$).tw.
- 43.(phenol or ethanol or alcohol or nerve block\$ or motor point block\$).tw.
- 44.(intramuscular adj3 (injection\$ or treatment\$ or medication\$ or neurolysis)).tw.
- 45.or/41-44.
- 46.(child\$ or adolescent\$).mp. [mp=title, original title, abstract, name of substance word, subject heading word].
- 47.8 and 35 and 40 and 45 and 46.

Databases: PEDro (1966 to April 2018)

Search strategy: Advanced.

Abstract and Title: Cerebral palsy and Botox.

Subdiscipline: Paediatrics.

Method: Clinical trial.

Nonlinear Dynamic Analysis of Gear Pair System Based on Crack Rotor-Bearing System with Rub-Impact Effect

Cai-Wan Chang-Jian

Department of Mechanical and Automation Engineering
I-Shou University



Abstract

A systematic analysis of the dynamic behaviors of a gear pair system based on rotor-bearing system under strongly nonlinear effects, i.e. nonlinear suspension effect, nonlinear oil-film force, nonlinear rub-impact force, nonlinear gear mesh force and crack effect is presented in this study. The dynamic trajectories of the system are observed using bifurcation diagrams plotted using the dimensionless rotational speed ratio and dimensionless parameter of depth of crack as control parameters. The onset of non-periodic or chaotic motion is specified from the phase diagrams, power spectra, Poincaré maps, Lyapunov exponents and fractal dimension of the system. There exist various forms of periodic, quasi-periodic

and chaotic motions at different bifurcation parameters. The simulation results are also found that highly non-periodic motions do exist in gear-rotor-bearing systems under those nonlinear effects. The results presented in this study provide an understanding of the operating conditions under which undesirable dynamic motion takes place in a gear-bearing system and therefore serve as a useful source of reference for engineers in designing and controlling such systems.

Keywords: gear pair, crack, rub-impact, rotor-bearing system

Introduction

It is well known that vibrations of gear pairs are significantly affected by

the amplitude and phase of deviations of the tooth profile from the true involute profile. Gear errors must be checked carefully especially to avoid systematic faults especially for highly precision manufacturing, consequently. Accordingly, many studies have focused on analyzing gear dynamics [1-5] and they introduced some methods based on the measurement of the gear torsional vibrations to identify natural frequency, damping parameters and equivalent gear error of a spur gear pair model with constant stiffness. The effects of the dynamic backlash subjected to internal and external periodic excitations are considered in the gear pair system and performed by Li et al. [6]. The dynamic backlash, time-varying stiffness and excitation force amplitude are also considered in this study. The parametric resonance, multi-valued properties and jump phenomena are found in the dynamic model. The excitation force amplitude is not the key effect to affect the vibration of gear systems, but the increase of dynamic backlash and damping ratio may play the significant roles to control the nonlinear vibration. Li et al. [7] studied a gear-shaft-bearing system with the backlash, time-varying mesh stiffness and radial clearance of

bearing. The crack effect of shaft is also considered in their study. The dynamic responses and bifurcation plots are used to show their simulation results. They proved that gentle crack fault may induce instantaneous tooth separation and serious double-sided impact faults. Cooley et al. [8] presented a comparison of calculation approaches to study the gear dynamics with the gear tooth mesh stiffness. Dai et al. [9] studied the dynamic responses of the spur gear pair system with both the theoretical and experimental analysis. The dynamic tooth root strains and experimental correlations are also considered in their study. Sainte-Marie et al. [10] analyzed spur gear and helical gear considering the correlation between dynamic transmission error and dynamic tooth loads in their study. Korta et al. [11] used the method of combining finite element approach and multibody modeling techniques to study the nonlinear dynamics of gear systems with time-efficient simulation. Recently, Arreyndip et al. [12] performed a research of studying nonlinear multi-frequency dynamics of wind turbine components with a single-mesh helical gear train system. Including time-varying mesh stiffness, axial

vibrations, torsional vibrations, shaft and bearing damping and gear backlashes are considered in their study. They proved that a smaller mesh frequency will induce extra noise in the generator, and the external excitation due to wind gust has a greater influence on the nonlinearity of the wind turbine dynamics as compared to the internal excitations due to static transmission errors, time and varying mesh stiffness.

Previous studies never considered all the nonlinear effects, i.e. nonlinear suspension, nonlinear rub-impact force, nonlinear oil-film force, crack shaft effect and nonlinear gear mesh force to analyze the gear-rotor-bearing systems at the same time. The present study performs a nonlinear analysis of the dynamic behavior of a gear pair system equipped with rotor-bearing system under nonlinear suspension, nonlinear rub-impact force, nonlinear oil-film force, crack shaft effect and nonlinear gear mesh force. The frictional force of meshing teeth, time-varying stiffness and damping on gear pairs system are also considered in this study. The remainder of this paper is organized as follows. Section 2 derives dynamic models for the gear-rotor-bearing system with a nonlinear suspension effect,

strongly nonlinear rub-impact force, strongly nonlinear gear mesh force, crack shaft effect and strongly nonlinear oil-film force. Section 3 describes the simulation results of techniques, i.e. phase plots, FFT spectra, Poincaré maps, bifurcation diagrams, Lyapunov exponents and the fractal dimension of the system used to analyze the dynamic response of the gear-rotor-bearing system and also presents the numerical analysis results obtained for the behavior of the gear-rotor-bearing system under various operational conditions. Finally, Section 4 presents some brief conclusions.

Mathematical Modeling

The dynamic model simulating the gear-rotor-bearing system under the assumptions of nonlinear rub-impact force, nonlinear fluid film force, nonlinear suspension effect, crack effect and nonlinear gear meshing force is presented in Figure 1.

Applying the principles of force equilibrium, the forces acting at the center of journal 1, i.e. $O_{j1}(X_{j1}, Y_{j1})$, center of journal 2, i.e. $O_{j2}(X_{j2}, Y_{j2})$, equations of motion of $O_g(X_g, Y_g)$ and $O_p(X_p, Y_p)$ in Cartesian coordinate form and equations of motion of the center of bearing 1 (X_1, Y_1), the center of bearing 2 (X_2, Y_2) and the center of rotor under the assumption of nonlinear suspension are given by

$$m_p X_p + C X_p + K_{p1}(X_p - X_{j1}) = W_{cx} \quad (1)$$

$$m_p Y_p + C Y_p + K_{p1}(Y_p - Y_{j1}) = L_{py} - G_{py} - W_{cy} - m_p g \quad (2)$$

$$m_g X_g + C X_g + K_{p2}(X_g - X_{j2}) \left(1 - \frac{\delta_1 \delta_2}{2}\right) + \frac{\delta_1 f}{2} K [(X_g - X_{j2}) \cos(2\omega t) + (Y_g - Y_{j2}) \cos(2\omega t)] = -W_{cx} \quad (3)$$

$$m_g Y_g + C Y_g + K_{p2}(Y_g - Y_{j2}) \left(1 - \frac{\delta_1 \delta_2}{2}\right) + \frac{\delta_1 f}{2} K [(X_g - X_{j2}) \cos(2\omega t) - (Y_g - Y_{j2}) \cos(2\omega t)] = L_{py} - G_{py} + W_{cy} - m_g g \quad (4)$$

$$m_1 X_1 + C_1 X_1 + K_{11} X_1 + K_{12} X_1^3 = F_{x1} \quad (5)$$

$$m_1 Y_1 + C_1 Y_1 + K_{11} Y_1 + K_{12} Y_1^3 = -m_1 g + F_{y1} \quad (6)$$

$$m_2 X_2 + C_2 X_2 + K_{21} X_2 + K_{22} X_2^3 = F_{x2} \quad (7)$$

$$m_2 Y_2 + C_2 Y_2 + K_{21} Y_2 + K_{22} Y_2^3 = -m_2 g + F_{y2} \quad (8)$$

$$m_r X_r + C_r X_r + K_r(X_r - X_g) + K_r(X_r - X_{j1}) = m_r \rho \omega^2 \cos \phi + R_x \quad (9)$$

$$m_r Y_r + C_r Y_r + K_r(Y_r - Y_g) + K_r(Y_r - Y_{j1}) = m_r \rho \omega^2 \cos \phi - m_r g + R_y \quad (10)$$

where f_{e1} and $f_{\phi 1}$ are the viscous damping forces in the radial and tangential directions for the center of journal 1 respectively, and f_{e2} and $f_{\phi 2}$ are the viscous damping forces in the radial and tangential directions for the center of journal 2 respectively. R_x and R_y are the components of the rub-impact force.

$$\delta_1 = \frac{1}{2} L_R \frac{\bar{\lambda}_\xi - \bar{\lambda}_\eta}{(L_R + \bar{\lambda}_\xi)(L_R + \bar{\lambda}_\eta)}, \quad \delta_2 = \frac{1}{\delta_1} - \frac{\bar{\lambda}_\xi + \bar{\lambda}_\eta}{\bar{\lambda}_\xi - \bar{\lambda}_\eta} - \frac{2L_R}{\bar{\lambda}_\xi - \bar{\lambda}_\eta}, \quad L_R = \frac{L_1}{3R(1-\nu^2)},$$

$$\bar{\lambda}_\xi = \frac{\pi R^3 E}{(1-\nu^2)} c_\xi \int_{-\frac{b}{R}}^{\frac{b}{R}} \int_0^{\frac{\eta}{R}} 32 \left[1 - \left(\frac{\xi}{R}\right)^2\right] \left(\frac{\bar{\eta}}{R}\right) F_2^2\left(\frac{\bar{\eta}}{R}\right) d\left(\frac{\bar{\eta}}{R}\right) d\left(\frac{\xi}{R}\right), \quad \bar{\lambda}_\eta = \frac{\pi R^3 E}{(1-\nu^2)} c_\eta \int_0^{\frac{b}{R}} \int_0^{\frac{\eta}{R}} 32 \left(\frac{\xi}{R}\right)^2 \left(\frac{\bar{\eta}}{R}\right) F_1^2\left(\frac{\bar{\eta}}{R}\right) d\left(\frac{\bar{\eta}}{R}\right) d\left(\frac{\xi}{R}\right),$$

$h = 2\sqrt{R^2 - \xi^2}$, $\eta(\xi) = a - R + \sqrt{R^2 - \xi^2}$ is the local depth of crack, L_1 is the length of shaft between both supported ends, R is the radius of journal, E is the Young's Modulus, a is the depth of crack and ν is the poisson ratio.

$$F_1\left(\frac{\eta}{h}\right) = \sqrt{\frac{2h}{\pi\eta \tan\left(\frac{\pi\eta}{2h}\right)}} \{0.923 + 0.199[1 - \sin(\pi\eta)]^4\} / \cos\left(\frac{\pi\eta}{2h}\right)$$

$$F_2\left(\frac{\eta}{h}\right) = \sqrt{\frac{2h}{\pi\eta \tan\left(\frac{\pi\eta}{2h}\right)}} \{0.752 + 2.02\left(\frac{\eta}{h}\right) + 0.37[1 - \sin(\pi\eta)]^3\} / \cos\left(\frac{\pi\eta}{2h}\right). \quad L_{py} \text{ and } L_{gy} \text{ are the centrifugal}$$

forces in the vertical gear mesh direction for pinion and gear, G_{py} and G_{gy} are the inertia forces in the vertical gear mesh direction for pinion and gear, w_{cx} is the dynamic gear mesh force in the horizontal direction, and w_{cy} is the dynamic gear mesh force in the vertical direction. L_{py} , L_{gy} , G_{py} , G_{gy} , w_{cx} and w_{cy} can be performed as:

$$L_{py} = m_p e_p \omega_p^2 \sin \theta_1, \quad (11)$$

$$L_{gy} = m_g e_g \omega_g^2 \sin \theta_2, \quad (12)$$

$$G_{py} = m_p e_p \ddot{\theta}_1 \cos \theta_1, \quad (13)$$

$$G_{gy} = m_g e_g \ddot{\theta}_2 \cos \theta_2, \quad (14)$$

$$W_{Cx} = C_m(\dot{X}_p - \dot{X}_g - e_p \Omega \sin(\Omega t)) + K_m(X_p - X_g - e_p \sin(\Omega t)), \quad (15)$$

$$W_{Cy} = C_m(\dot{Y}_p - \dot{Y}_g - e_p \Omega \cos(\Omega t)) + K_m(Y_p - Y_g - e_p \cos(\Omega t)), \quad (16)$$

Introducing the following parameters:

$$x_j = X_j / d, \quad y_j = Y_j / d, \quad j = 1, 2, j1, j2, p, g, \quad \frac{d}{dt} = \Omega \frac{d}{d\phi}, \quad s^2 = \frac{\Omega^2}{\omega_n^2}, \quad \omega_n^2 = K / m_p, \quad \omega_g = \Omega / 8,$$

$$\omega_p = \Omega / 4, \quad \beta = E_p / 16, \quad \beta_g = E_p / 16, \quad f = \frac{m_p g}{dK}, \quad f_g = \frac{Kg}{dm_p}, \quad \xi_1 = \frac{C_1}{2\sqrt{K_1 m_1}}, \quad \xi_2 = \frac{C}{2\sqrt{K m_p}},$$

$$\xi_3 = \frac{C_m}{2\sqrt{K m_p}}, \quad \xi_4 = \frac{C}{2\sqrt{\frac{K}{m_p} m_g}}, \quad \xi_5 = \frac{C_m \sqrt{m_p}}{2m_g \sqrt{K}}, \quad \xi_6 = \frac{C_2}{2\sqrt{K_2 m_2}}, \quad C_{1p} = \frac{m_1}{m_p}, \quad C_{01} = \frac{K}{k_1}, \quad s_1^2 = C_{01} C_{1p} s^2,$$

$$C_{2p} = \frac{m_2}{m_p}, \quad C_{02} = \frac{K}{k_2}, \quad s_2^2 = C_{02} C_{2p} s^2, \quad \Lambda = \frac{K_m}{K}, \quad \Lambda_g = \frac{K_m m_p^2}{m_g K^2}, \quad \alpha_1 = \frac{K_{12} d^2 K}{m_1 m_p}, \quad \alpha_1 = \frac{K_{22} d^2 K}{m_2 m_p},$$

$$p = mc\omega^2, \quad \Gamma = 1 - \frac{\delta_1 \delta_2}{2}$$

Equations (1)~(10) can be expressed as

$$x_p'' = -\frac{2\xi_2}{s} x_p' - \frac{1}{s^2} (x_p - x_1 - \varepsilon_1 \cos \varphi_1) + \beta \cos(\phi/4) - \frac{2\xi_3}{s} (x_p' - x_g' - E_p \sin \phi) - \frac{\Lambda}{s^2} (x_p - x_g - E_p \cos \phi), \quad (17)$$

$$y_p'' = -\frac{2\xi_2}{s} y_p' - \frac{1}{s^2} (y_p - y_1 - \varepsilon_1 \sin \varphi_1) + \beta \sin(\phi/4) - \frac{2\xi_3}{s} (y_p' - y_g' - E_p \cos \phi) - \frac{\Lambda}{s^2} (y_p - y_g - E_p \sin \phi) - \frac{f}{s^2}, \quad (18)$$

$$x_g'' = -\frac{2\xi_4}{s} x_g' - \frac{\Gamma}{s^2} (x_g - x_2 - \varepsilon_2 \cos \varphi_2) - \frac{\delta_1 f}{2s^2} [(x_g - x_2 - \varepsilon_2 \cos \varphi_2) \cos(2\phi) + (y_g - y_2 - \varepsilon_2 \sin \varphi_2) \sin(2\phi)] \\ + \beta_g \cos(\phi/8) + \frac{2\xi_5}{s} (x_p' - x_g' - E_p \sin \phi) - \frac{\Lambda_g}{s^2} (x_p - x_g - E_p \cos \phi), \quad (19)$$

$$y_g'' = -\frac{2\xi_4}{s} y_g' - \frac{\Gamma}{s^2} (y_g - y_2 - \varepsilon_2 \sin \varphi_2) - \frac{\delta_1 f}{2s^2} [(x_g - x_2 - \varepsilon_2 \cos \varphi_2) \sin(2\phi) - (y_g - y_2 - \varepsilon_2 \sin \varphi_2) \cos(2\phi)] + \beta_g \sin(\phi/8) + \frac{2\xi_5}{s} (y_p' - y_g' - E_p \cos \phi) + \frac{\Lambda_g}{s^2} (y_p - y_g - E_p \sin \phi) - \frac{f_g}{s^2}, \quad (20)$$

$$x_1'' + \frac{2\xi_1}{s_1} x_1' + \frac{1}{s_1^2} x_1 + \frac{\alpha_1}{s_1^2} x_1^3 - \frac{1}{2C_{1p}s_1^2} (x_p - x_1 - \varepsilon_1 \cos \varphi_1) = 0, \quad (21)$$

$$y_1'' + \frac{2\xi_1}{s_1} y_1' + \frac{1}{s_1^2} y_1 + \frac{\alpha_1}{s_1^2} y_1^3 - \frac{1}{2C_{om}s_1^2} (y_p - y_1 - \varepsilon_1 \sin \varphi_1) + \frac{f}{s_1^2} = 0, \quad (22)$$

$$x_2'' + \frac{2\xi_6}{s_2} x_2' + \frac{1}{s_2^2} x_2 + \frac{\alpha_2}{s_2^2} x_2^3 - \frac{1}{2C_{2p}s_2^2} (x_g - x_2 - \varepsilon_2 \cos \varphi_2) = 0, \quad (23)$$

$$y_2'' + \frac{2\xi_6}{s_2} y_2' + \frac{1}{s_2^2} y_2 + \frac{\alpha_2}{s_2^2} y_2^3 - \frac{1}{2C_{2p}s_2^2} (y_g - y_2 - \varepsilon_2 \sin \varphi_2) + \frac{f}{s_2^2} = 0, \quad (24)$$

$$x_r'' + \frac{2\xi_2}{s_3} x_r' + \frac{1}{s_3^2} (x_r - x_g) + \frac{1}{s_3^2} (x_r - x_1 - \varepsilon \cos \varphi) = \beta_r \cos \phi + \frac{R_x}{p}, \quad (25)$$

$$y_r'' + \frac{2\xi_2}{s_3} y_r' + \frac{1}{s_3^2} (y_r - y_g) + \frac{1}{s_3^2} (y_r - y_1 - \varepsilon \sin \varphi) = \beta_r \sin \phi - \frac{f}{s_3^2} + \frac{R_y}{p}, \quad (26)$$

Equations (17)~(26) describe a non-linear dynamic system.

Analytical Tools, Numerical Results and Discussions

The analytical tools used to observe nonlinear dynamics of the gear-rotor-bearing system with rub-impact effect and crack effect in this study are dynamic trajectories, Poincaré maps, spectrum, bifurcation diagram, Lyapunov exponent and fractal dimension. A bifurcation diagram can be used to summarize the essential dynamics of the system and is therefore a useful means of observing its nonlinear dynamic response at first step. Then we may check the dynamic trajectories, Poincaré maps and spectrum for each bifurcation parameters to clarify the more detailed dynamic behaviors in the next step. Finally, Lyapunov exponent and fractal dimension are used as the most useful tools to detect chaotic motions for nonlinear dynamical systems.

In the simulations, the system parameters are assigned the following values: $f = 0.2$, $f_g = 0.2$, $\xi_1 = 0.01$, $\xi_2 = 0.02$, $\xi_3 = 0.015$, $\xi_4 = 0.02$, $\xi_5 = 0.015$, $\xi_6 = 0.02$, $C_{1p} = 2.0$, $\Lambda = 0.04$, $\Lambda_g = 0.04$, $\alpha_1 = 1.0$, $\alpha_2 = 1.0$, $x_1(0) = 0.11$, $x'_1(0) = 0.00001$, $y_1(0) = 0.22$, $y'_1(0) = 0.00001$, $x_2(0) = 0.11$, $x'_2(0) = 0.00001$, $y_2(0) = 0.22$,

$$\begin{aligned} y'_2(0) &= 0.00001 & , & & x_p(0) &= 0.11 & , \\ x'_p(0) &= 0.00001 & , & & y_p(0) &= 0.22 & , \\ y'_p(0) &= 0.00001 & , & & x_g(0) &= 0.22 & , \\ x'_g(0) &= 0.00001 & , & & y_g(0) &= 0.22 & , \\ y'_g(0) &= 0.00001 & , & & x_r(0) &= 0.5 & , \\ x'_r(0) &= 0.00000001 & , & & y_r(0) &= 0.2 & , \\ y'_r(0) &= 0.00000001 & [24]. \end{aligned}$$

The nonlinear dynamic equations introduced in Equations (21) to (34) for the gear-rotor-bearing system with nonlinear suspension effects, strongly nonlinear oil-film force, nonlinear gear mesh force, crack effect and nonlinear rub-impact force were solved with direct numerical integration. The time step in the iterative solution procedure was assigned a value of $\pi/300$ and the termination criterion was specified as an error tolerance of less than 0.0001. The time series data corresponding to the first 800 revolutions of the whole system were deliberately excluded from the dynamic analysis to ensure that the analyzed data related to steady-state conditions. The effects of system parameters on analyzing dynamical behaviors are investigated in this section. Among many control parameters, the main system parameters, rotating speed and parameter of depth of crack are analyzed and discussed.

In practical rotor-bearing systems, the rotational speed ratio s is most commonly used as a control parameter. Accordingly, the dynamic behavior of the current gear-bearing system was also examined using the dimensionless rotational speed ratio s as a bifurcation control parameter. Figures 2(a)~2(e) display the bifurcation diagrams for the displacement of the gear-rotor-bearing system with crack effect against the dimensionless rotational speed ratio, s . The bifurcation diagrams show that the centers of bearing 1, bearing 2, gear center, pinion center and rotor center perform almost the same dynamic behaviors for different rotational speed ratios s , but the amplitude of each geometrical center behaves totally different. Especially, the dynamic trajectories of gear center and pinion center present higher amplitudes for almost every dimensionless rotational speed ratios except lower rotational speed ratios. The dynamic trajectories behave T-periodic at lower rotational speeds, i.e. $s < 0.49$, and they will become quasi-periodic for $s = 0.50 \sim 0.89$. The dynamic trajectories present fully non-periodic until $s < 3.50$ and they present chaotic for $s = 0.90 \sim 1.49$, quasi-periodic for $s = 1.50 \sim 1.99$, chaotic

for $s = 2.00 \sim 2.30$, quasi-periodic for $s = 2.31 \sim 2.49$ and chaotic for $s = 2.50 \sim 3.50$. 3T-periodic motions are found for $s = 3.51 \sim 3.79$, and they may be regarded as chaotic motions. Then the dynamic trajectories perform quasi-periodic for $s = 3.80 \sim 4.20$ and become 8T-periodic for $s > 4.21$, finally.

The dynamic trajectory of rotor center is most important for the analysis of gear-rotor-bearing system especially with crack effect, and therefore we introduce the dynamic orbits more clearly. In figures 3, Poincaré maps corresponding to different dimensionless rotational speed ratios for rotor center are provided to show the tendency of dynamic trajectories of rotor center. The Poincaré section shown in figures 3 tells us that the return points of Poincaré maps present periodic at $s = 0.01, 0.10, 0.20, 0.30$ and 0.40 , quasi-periodic at $s = 0.50, 0.60, 0.70$ and 0.80 , chaotic at $s = 0.90, 1.00, 1.10, 1.20, 1.30$ and 1.40 , quasi-periodic at $s = 1.50, 1.60, 1.70, 1.80$ and 1.90 , chaotic at $s = 2.00, 2.10, 2.20, 2.30, 2.40, 2.50, 2.60, 2.70, 2.80, 2.90, 3.00, 3.10, 3.20, 3.30, 3.40$ and 3.50 , 3T-periodic at $s = 3.60$ and 3.70 , quasi-periodic at $s = 3.80, 3.90, 4.00, 4.10$ and 4.20 , 8T-periodic at $s = 4.30, 4.40, 4.50, 4.60$ and 4.70 . Figures 4 and 5 are

the simulation results for center of rotor center at $s=1.30$ and 3.50 in the horizontal direction respectively. The phase diagrams are highly disordered and the power spectra reveal numerous excitation frequencies. Furthermore, it can be seen that the return points in the Poincaré maps form geometrically fractal structures and the maximum Lyapunov exponent is positive in each case. Finally, the fractal dimensions are found to be 2.38 and 2.46 for the dimensionless rotational speed ratio of $s=1.30$ and 3.5 at the rotor center respectively. In other words, the results presented in these figures all indicate that the center of rotor exhibit chaotic behaviors at those values of the dimensionless rational speed ratios.

In this study, we introduce an important parameter, i.e. the depth of crack to verify the significance of rotor with crack effect. Figures 6 are bifurcation diagrams of gear-bearing system using dimensionless parameter of the depth of crack, A , as bifurcation parameter. The bifurcation results reveal that the dynamic trajectories behave nT -periodic for small depth of crack and non-periodic for higher values of depth of crack in accordance with the numerical results. We also pick a value

of depth of crack to prove that the chaotic motion found in this gear-rotor-bearing system, e.g. $A=0.93$. In figures 7, the dynamic trajectory behaves highly disordered and it may be classified as non-periodic. Nevertheless, we still cannot regarded the trajectory belongs to chaotic motion or quasi-periodic motion. Thus, we must introduce other tools to verify the dynamic behavior of rotor center with dimensionless depth of crack $A=0.93$. The power spectrum in this case reveals numerous excitation frequency and the return points in the Poincaré map form a geometrically fractal structure. The maximum Lyapunov exponent is also positive in this case. Finally, the fractal dimension is found to be 2.33 for the dimensionless depth of crack $A=0.93$ at the rotor center. In other words, the results presented in these figures all indicate that the rotor center exhibits the so-called chaotic behavior at the value of the dimensionless depth of crack.

Conclusions

This study performed a numerical analysis of the nonlinear dynamic responses of a gear-rotor-bearing system subject to nonlinear rub-impact force,

nonlinear suspension effects, nonlinear oil-film force, nonlinear gear mesh force and crack effect. The dynamic responses of the system are evaluated by reference to its dynamic trajectories, power spectra, Poincaré maps, bifurcation diagrams, maximum Lyapunov exponents and fractal dimensions, respectively. The analysis has investigated the dynamic response of the gear-rotor-bearing system as a function of the dimensionless depth of crack (A) and the dimensionless rotational speed ratio (s). The simulation results have shown that the gear-rotor-bearing system exhibit periodic, sub-harmonic, non-periodic and chaotic motions. Overall, the results presented in this study provide a detailed understanding of the nonlinear dynamic response of a gear-rotor-bearing system under typical rotational speed condition and crack effect. Specifically, the results enable suitable values of the depth of crack and rotational speed ratio to be specified such that chaotic behavior can be avoided, thus reducing the amplitude of the vibration within the system and extending the system life.

Nomenclature

- A dimensionless parameter of the depth of crack, $A=a/R$
- a depth of crack
- C damping coefficient of the gear mesh
- C_1 damping coefficients of the supported structure for bearing 1
- C_2 damping coefficients of the supported structure for bearing 2
- C_{1p} dimensionless parameter, $C_{1p} = \frac{m_1}{m_p}$
- C_{01} dimensionless parameter, $C_{01} = \frac{K}{k_1}$
- C_{2p} dimensionless parameter, $C_{2p} = \frac{m_2}{m_p}$
- C_{02} dimensionless parameter, $C_{02} = \frac{K}{k_2}$
- e static transmission error and varies as a function of time
- e_i offset of the journal center of the rotor relative to the X-coordinate direction
- f dimensionless parameter, $f = \frac{m_p g}{dK}$
- f_s dimensionless parameter, $f_s = \frac{Kg}{dm_p}$
- f_e, f_ϕ components of the fluid film force in radial and tangential directions
- g acceleration of gravity
- K stiffness coefficient of the gear mesh
- K_{11}, K_{12} stiffness coefficients of the springs supporting the two bearing housings for bearing 1

K_{21}, K_{22} stiffness coefficients of the springs supporting the two bearing housings for bearing 2

K_{p1}, K_{p2} stiffness coefficients of the shafts

L bearing length

m_1 mass of the bearing housing for bearing 1

m_2 mass of the bearing housing for bearing 2

m_p mass of the pinion

m_g mass of the gear

O_1 geometric centers of the bearing 1

O_2 geometric centers of the bearing 2

O_{j1} geometric centers of the journal 1

O_{j2} geometric centers of the journal 2

O_g center of gravity of the gear

O_p center of gravity of the pinion

p pressure distribution in the fluid film

R inner radius of the bearing housing

r radius of the journal.

s rotational speed ratio, $s = (\frac{\omega^2}{\omega_n^2})^{1/2}$

s_1 dimensionless parameter,

$$s_1^2 = C_{o1}C_{1p}s^2$$

s_2 dimensionless parameter,

$$s_2^2 = C_{o2}C_{2p}s^2$$

X, Y, Z horizontal, vertical and axial coordinates

x_j, y_j $X_j/c, Y_j/c$, $j=1, 2, j1, j2, p, g$

α_1 dimensionless parameter, $\alpha_1 = \frac{K_{12}d^2K}{m_1m_p}$

α_2 dimensionless parameter, $\alpha_2 = \frac{K_{22}d^2K}{m_2m_p}$

ξ_1 dimensionless parameter, $\xi_1 = \frac{C_1}{2\sqrt{K_1m_1}}$

ξ_2 dimensionless parameter, $\xi_2 = \frac{C}{2\sqrt{Km_p}}$

ξ_3 dimensionless parameter, $\xi_3 = \frac{C_m}{2\sqrt{Km_p}}$

ξ_4 dimensionless parameter, $\xi_4 = \frac{C}{2\sqrt{\frac{K}{m_p}m_g}}$

ξ_5 dimensionless parameter, $\xi_5 = \frac{C_m\sqrt{m_p}}{2m_g\sqrt{K}}$

ξ_6 dimensionless parameter, $\xi_6 = \frac{C_2}{2\sqrt{K_2m_2}}$

Λ dimensionless parameter, $\Lambda = \frac{K_m}{K}$

Λ_g dimensionless parameter, $\Lambda_g = \frac{K_m m_p^2}{m_g K^2}$

ρ mass eccentricity of the rotor

ϕ rotational angle, $\phi = \omega t$

ω rotational speed of the shaft

θ the angular position oil dynamic viscosity

ε eccentricity ratio, $\varepsilon = e/c$

ω_n natural frequency, $\omega_n = \sqrt{K/m_p}$

ω_g dimensionless parameter, $\omega_g = \omega_n / 8$

ω_p dimensionless parameter, $\omega_p = \omega_n / 4$

φ_l attitude angle of the rotor relative to the X-coordinate direction

Reference

- [1] A. Kahraman, R. Singh (1990), Nonlinear dynamics of a spur gear pair, *Journal of Sound and Vibration*, vol. 142, pp. 49-75.
- [2] H. H. Lin, R. L. Huston, J. J. Coy (1988), On dynamic loads in parallel shaft *transmission*: Part 1- modeling and analysis, *ASME Journal of Mechanical Design*, vol. 110, pp. 221-225.
- [3] K. Y. Yoon, S. S. Rao (1996), Dynamic load analysis of spur gears using a new tooth profile, *ASME Journal of Mechanical Design*, vol. 118, pp. 1-6.
- [4] K. Ichimaru, F. Hirano (1974), Dynamic behavior of heavy-loaded spur gears, *ASME Journal of Mechanical Design*, vol. 12, pp. 373-381.
- [5] M. Amabili, A. Fregolent (1998), A method to identify model parameters and gear errors by vibrations of a spur gear pair, *Journal of Sound and Vibration*, vol. 214(2), pp. 339-357.
- [6] Y. G. Li, T. N. Chen, X. P. Wang (2016), Non-linear dynamics of gear pair with dynamic backlash subject to combined internal and external periodic excitations, *Journal of Vibration and Control*, vol. 22(6), pp. 1693-1703.
- [7] C. Li, C. L. Cai (2015), Nonlinear dynamic analysis of a gear-shaft-bearing system with breathing crack and tooth wear faults, *The Open Mechanical Engineering Journal*, vol. 9, pp. 483-491.
- [8] X. Dai, C. G. Cooley, R. G. Parker (2016), Gear tooth mesh stiffness: A comparison of calculation approaches, *Mechanism and Machine Theory*, vol. 105, pp. 540-553.
- [9] X. Dai, C. G. Cooley, R. G. Parker (2016), *Dynamic* tooth root strains and experimental correlations in spur gear pairs, *Mechanism and Machine Theory*, vol. 101, pp. 60-74.
- [10] N. Sainte-Marie, P. Velex, G. Roulois, J. Caillet (2017), A study on the *correlation* between dynamic transmission error and dynamic tooth loads in spur and helical gears, *Journal of Vibration and Acoustics*, vol. 139(1), pp.011-021.

- [11]J. Korta, A. Palermo, D. Mundo, S. Shweiki (2015), Combining finite element and multibody modeling techniques for time-efficient simulation of nonlinear gear dynamics, *The Seventh International Conference on Advances in System Simulation*.
- [12]N. A. Arreyndip, A. M. Dikande, E. Joseph (2018), Nonlinear Multi-Frequency Dynamics of Wind Turbine Components with a Single-Mesh Helical Gear Train, *Mathematical Computation Application*, vol. 23, pp. 1-12.

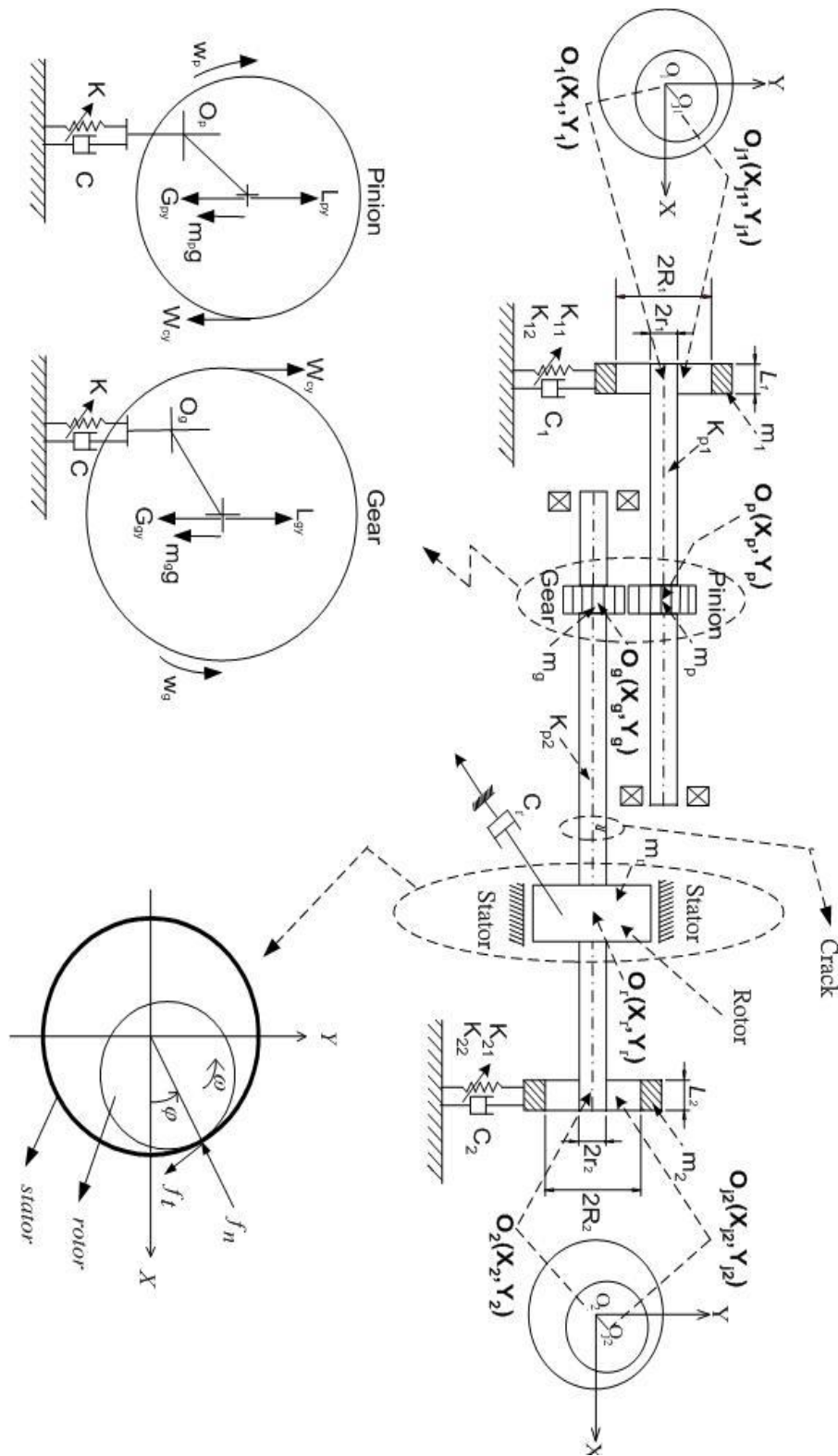
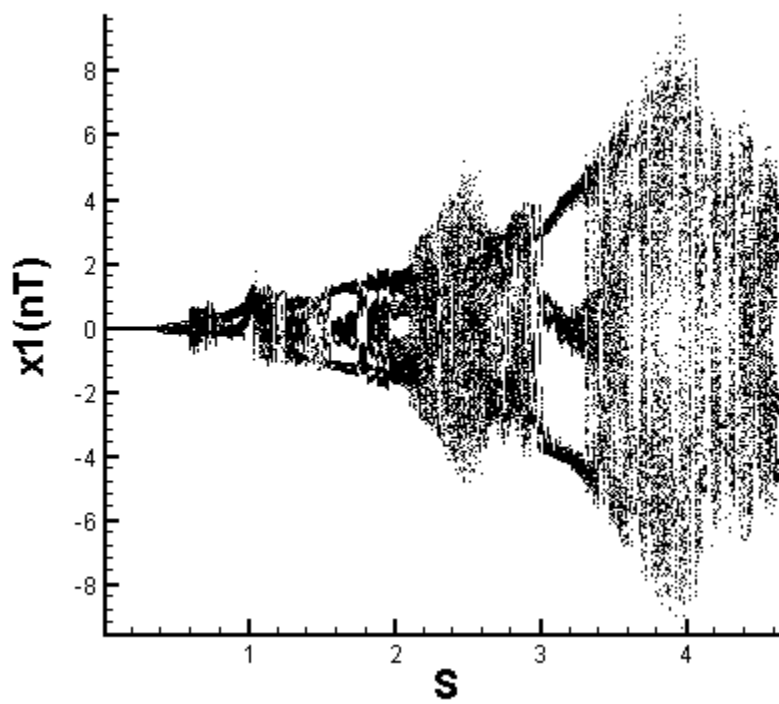
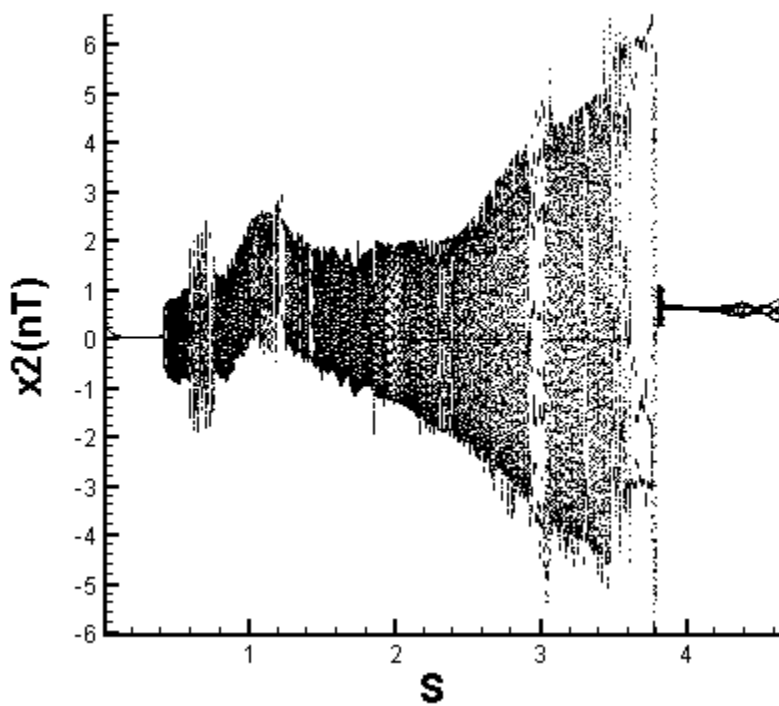


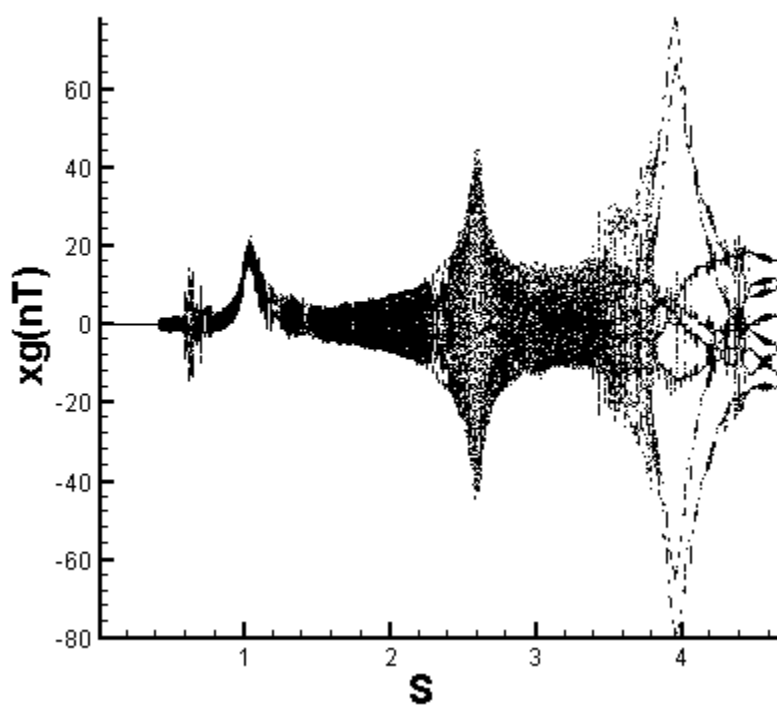
Fig.1 Schematic illustration of the gear-bearing system with crack effect under nonlinear suspension, model of force diagram between pinion and gear, and model of rub-impact force diagram between rotor and stator.



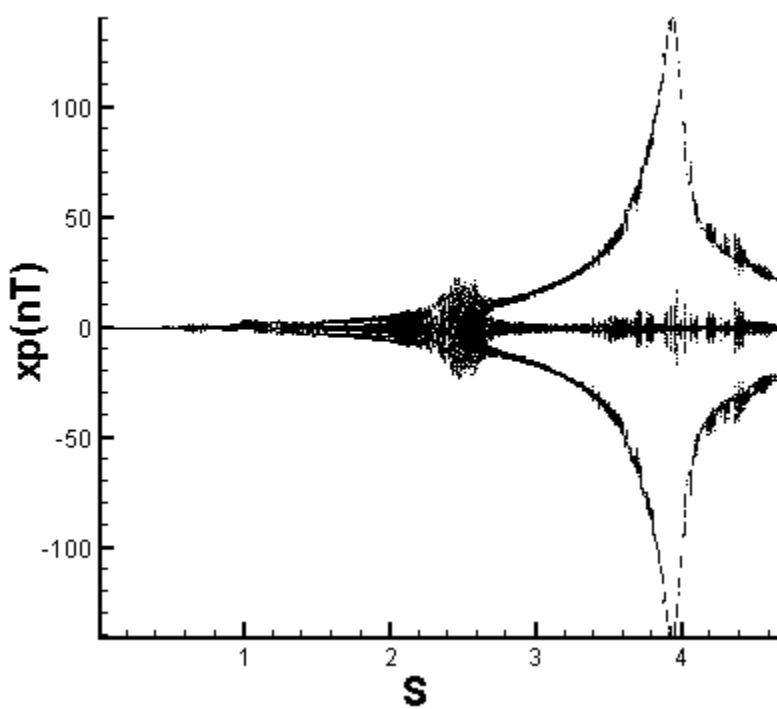
(a)



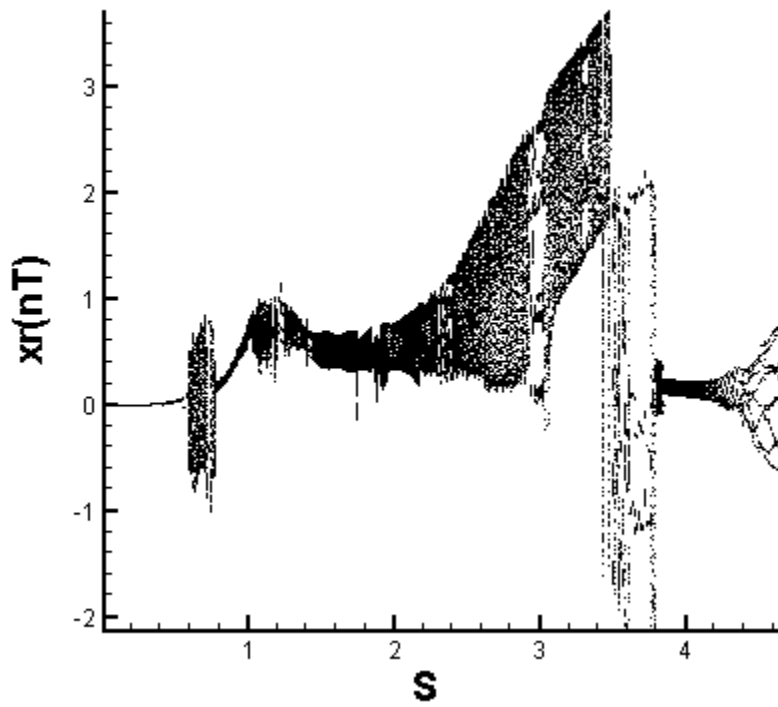
(b)



(c)

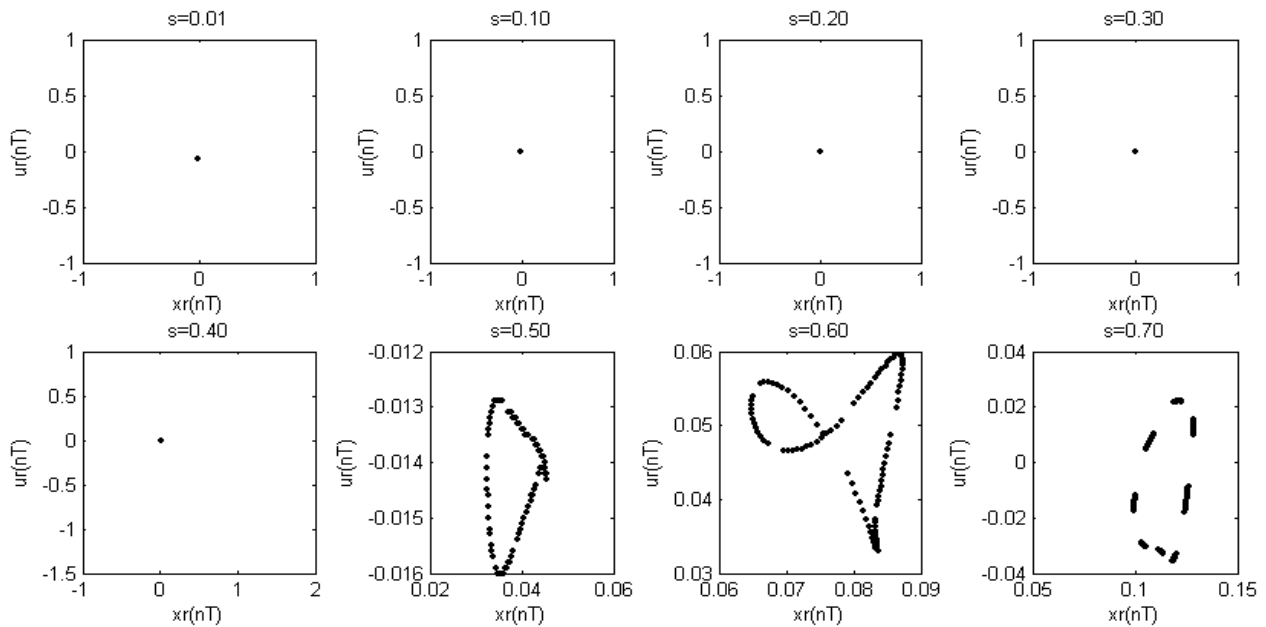


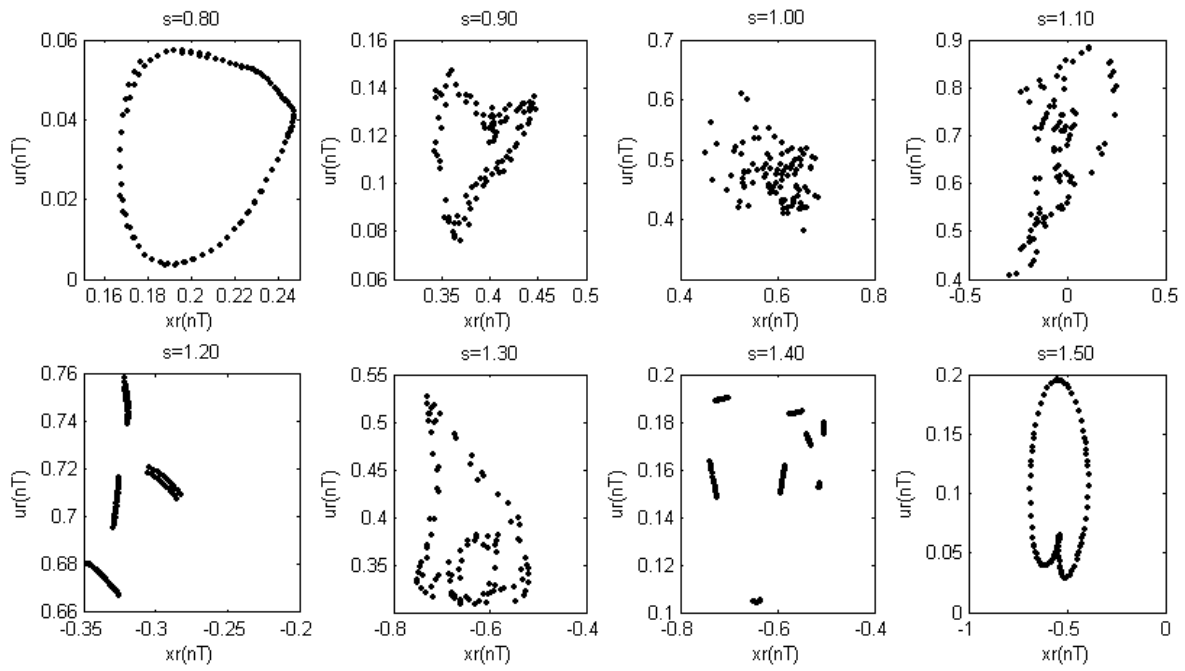
(d)



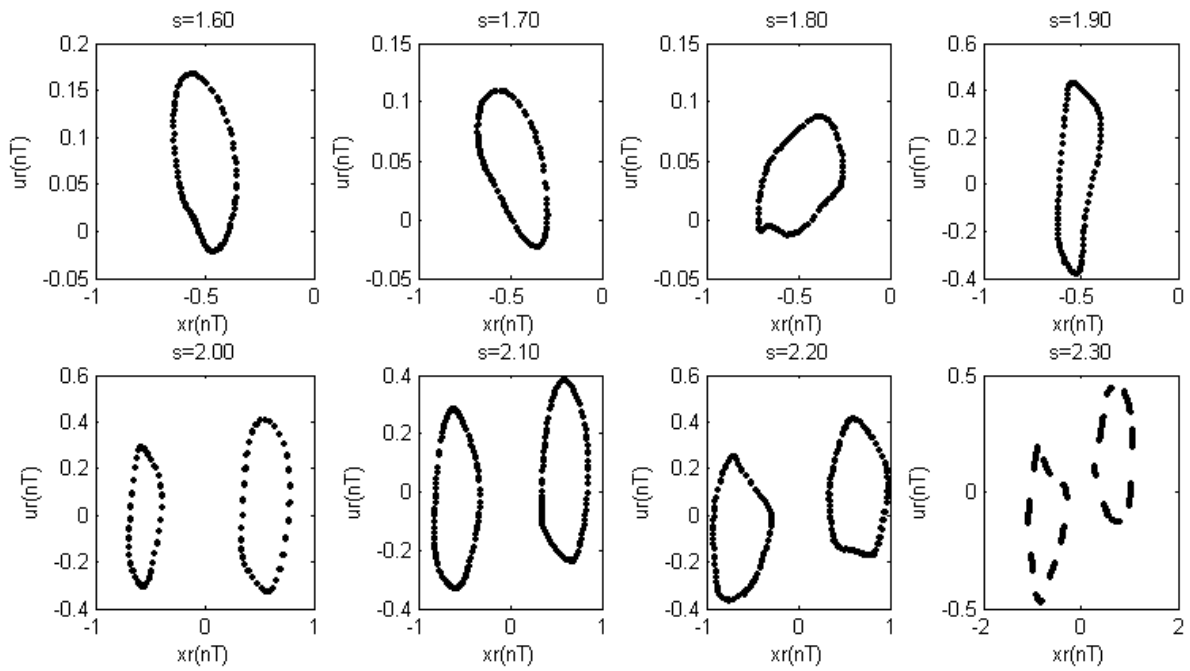
(e)

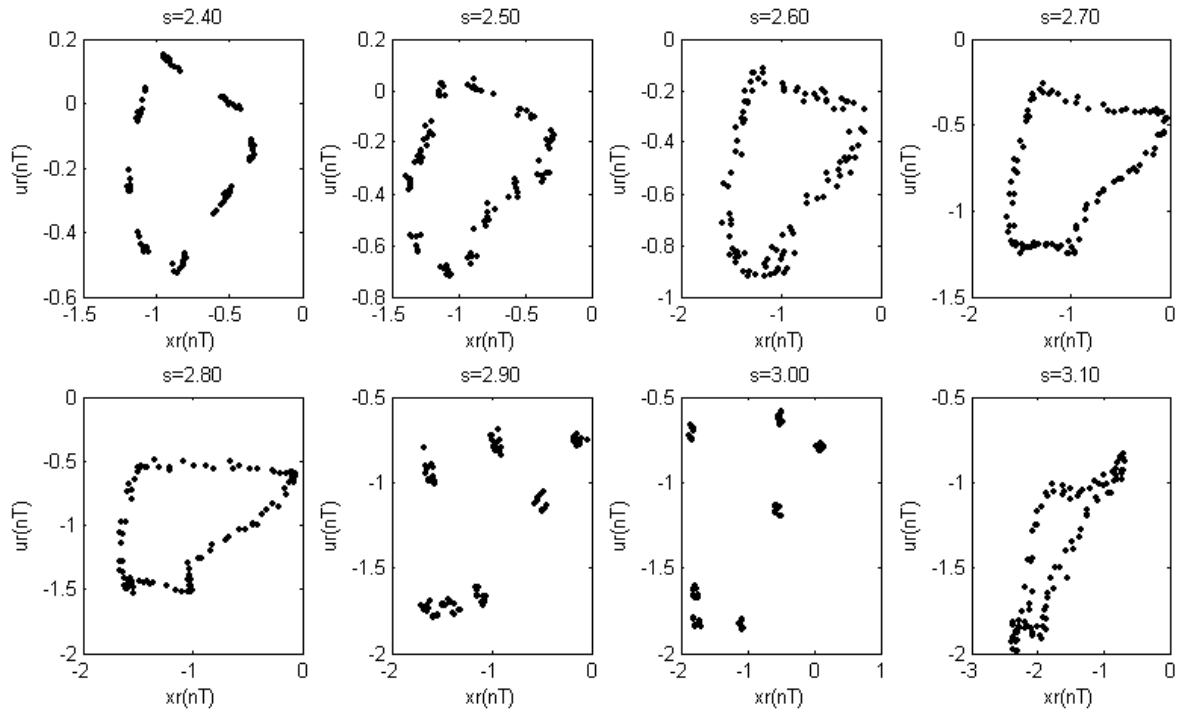
Fig.2 Bifurcation diagrams for bearing geometric center and gear center of gear-bearing system using dimensionless rotational speed ratio, s , as bifurcation parameter.



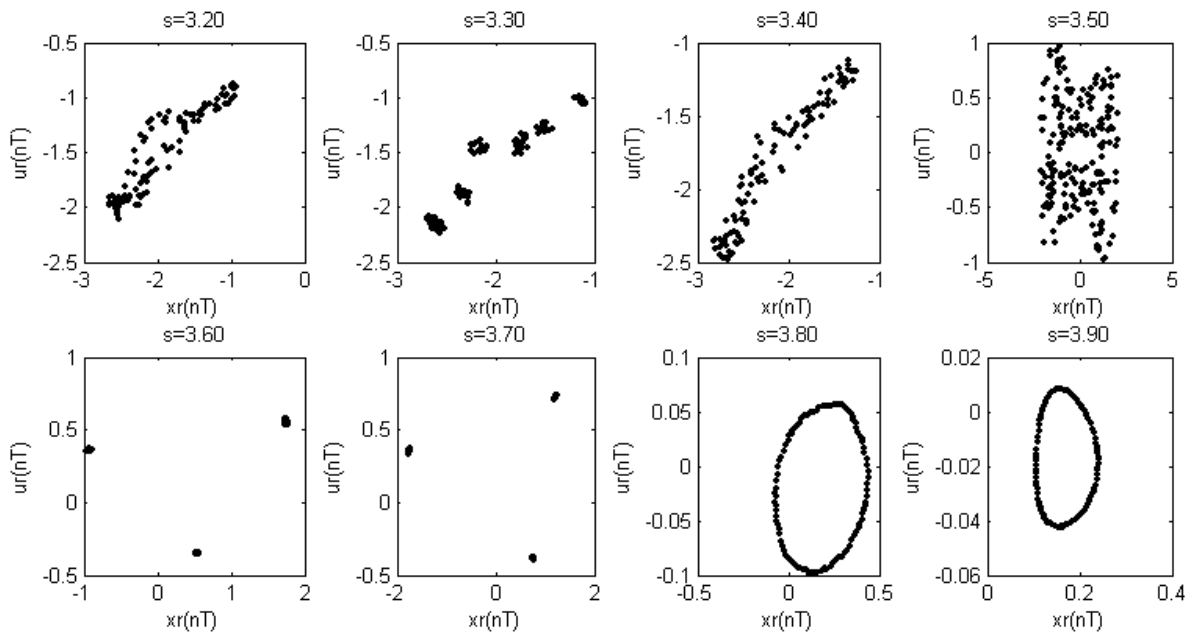


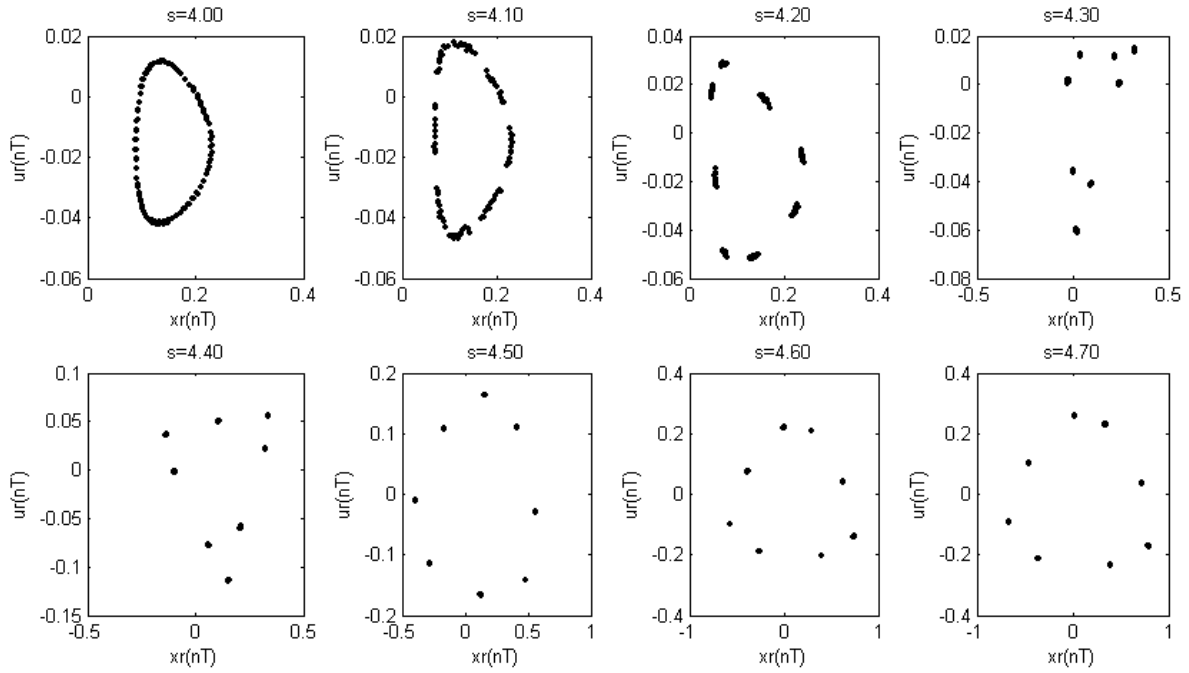
Part-a





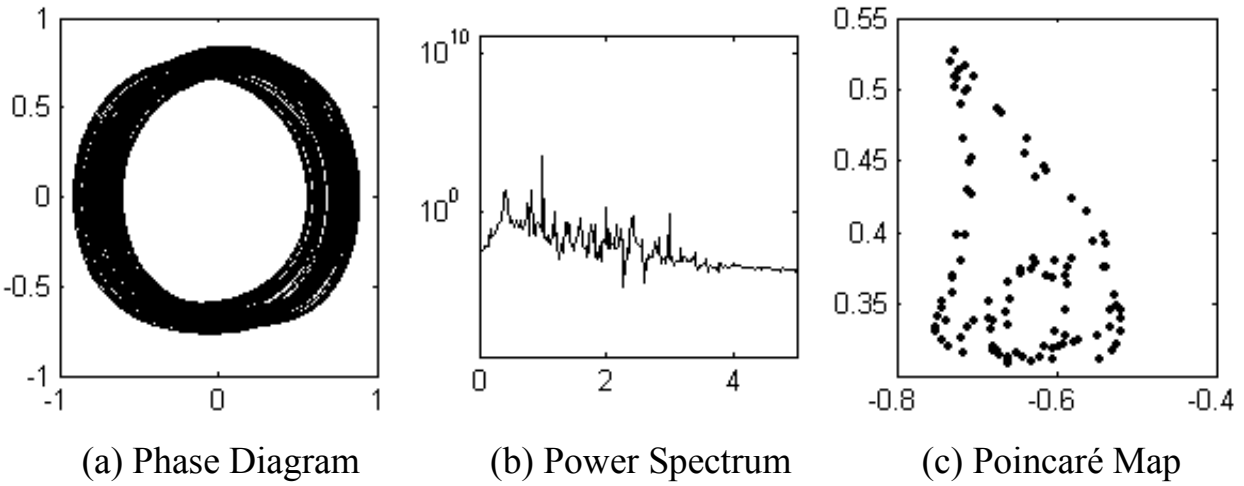
Part-b





Part-c

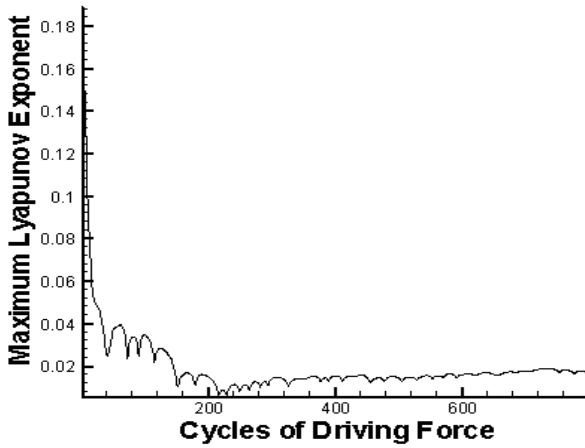
Fig.3 Poincaré maps corresponding to different dimensionless rotational speed ratio, $s(x_r)$.



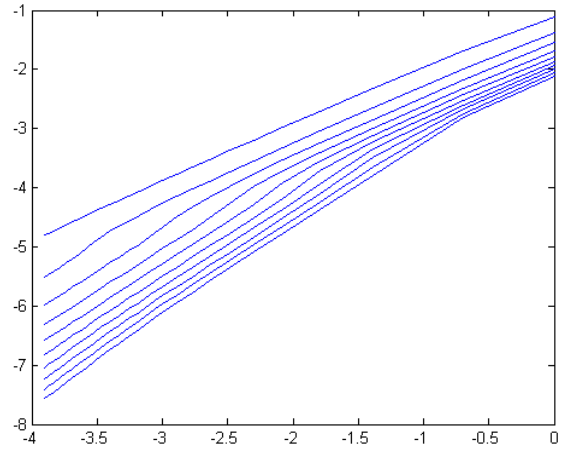
(a) Phase Diagram

(b) Power Spectrum

(c) Poincaré Map

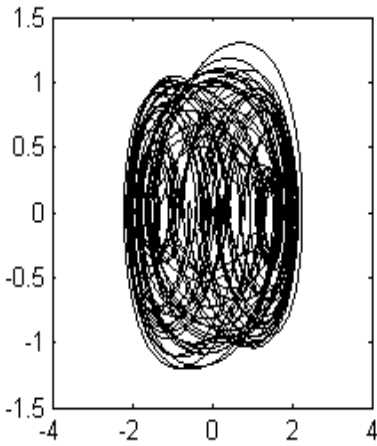


(d) Lyapunov Exponent

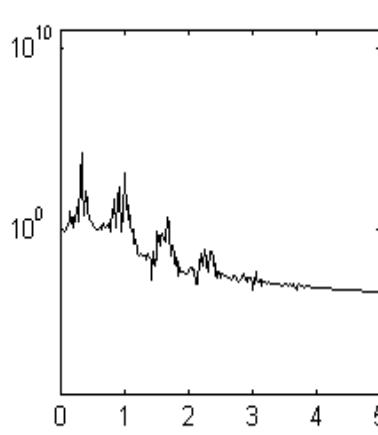


(e) Fractal Dimension

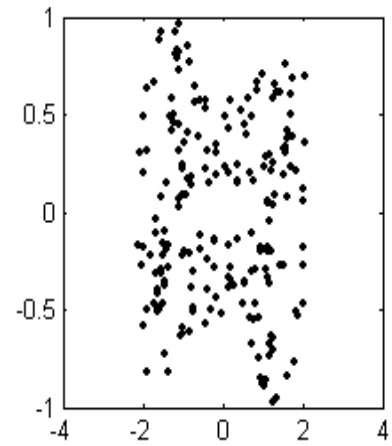
Fig.4 Simulation results obtained for gear-bearing system with $s=1.30(x_r)$.



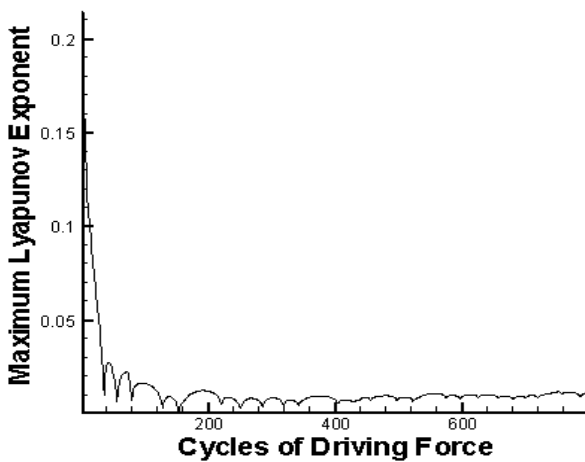
(a) Phase Diagram



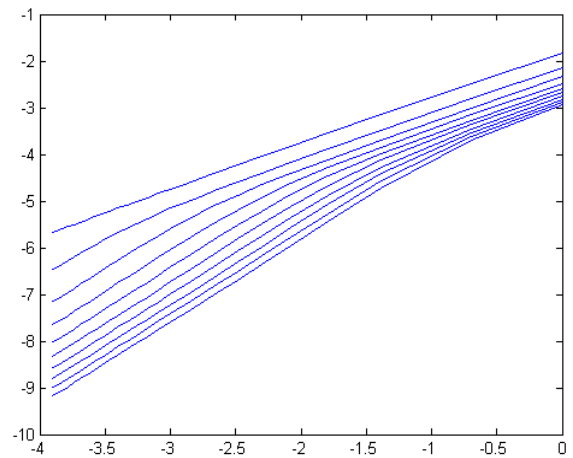
(b) Power Spectrum



(c) Poincaré Map

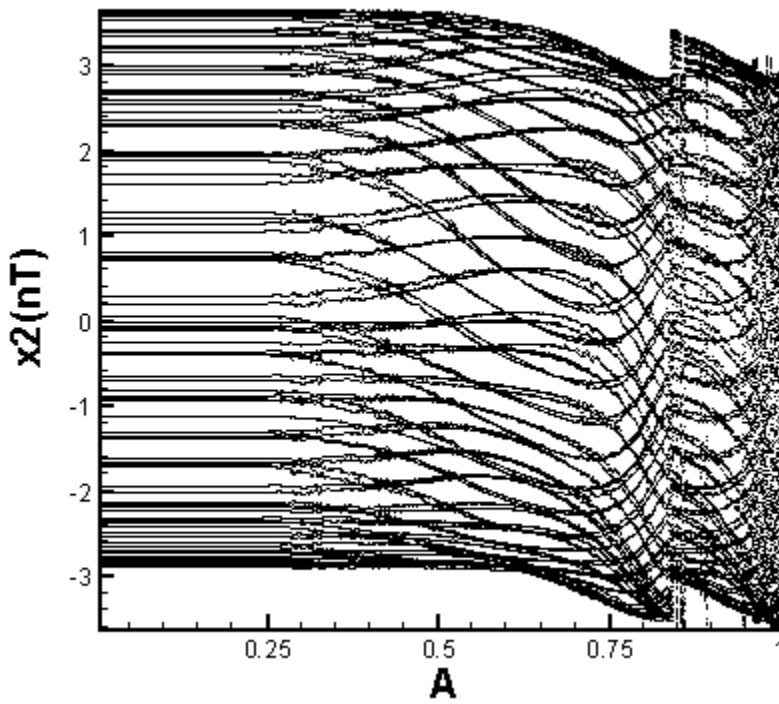
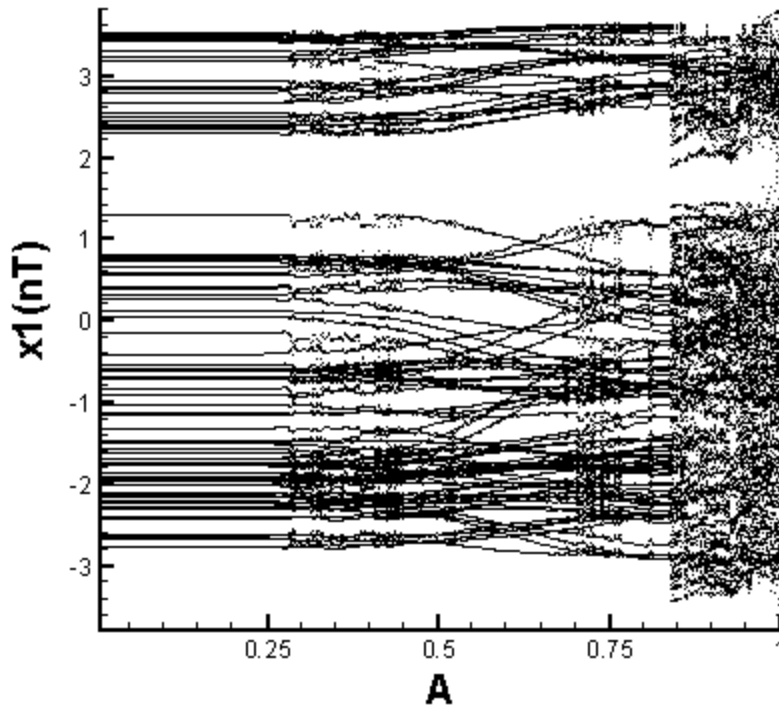


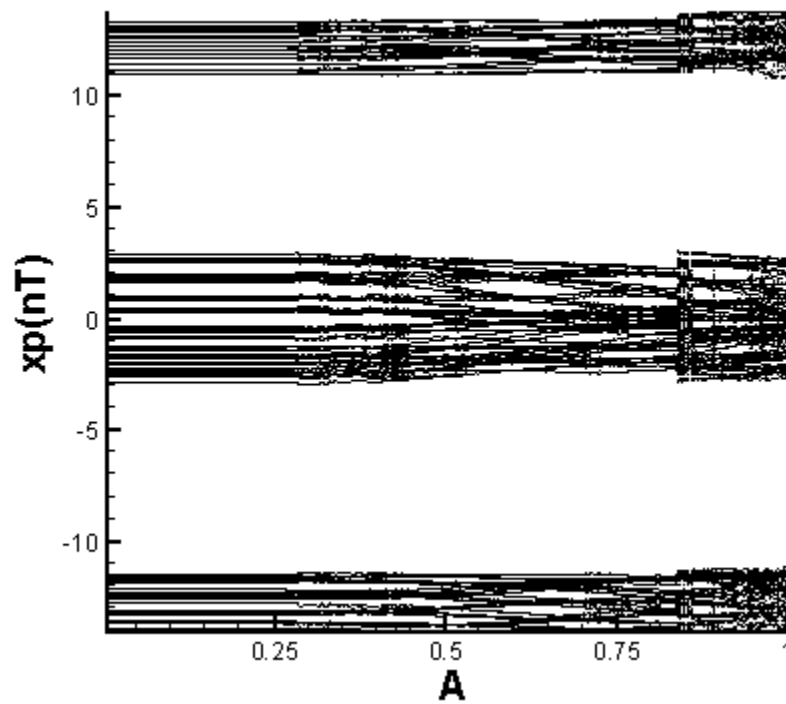
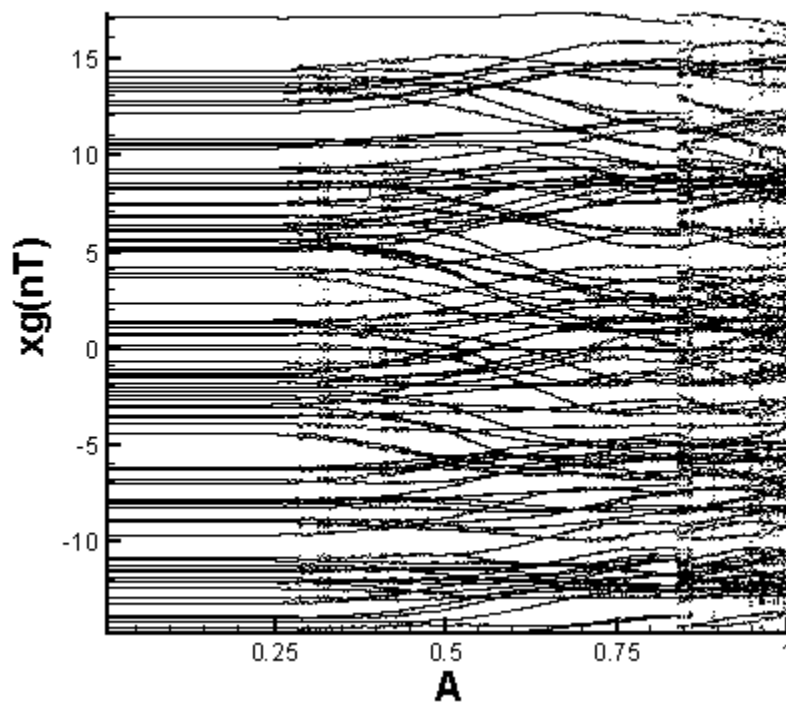
(d) Lyapunov Exponent



(e) Fractal Dimension

Fig.5 Simulation results obtained for gear-bearing system with $s=3.50(x_r)$.





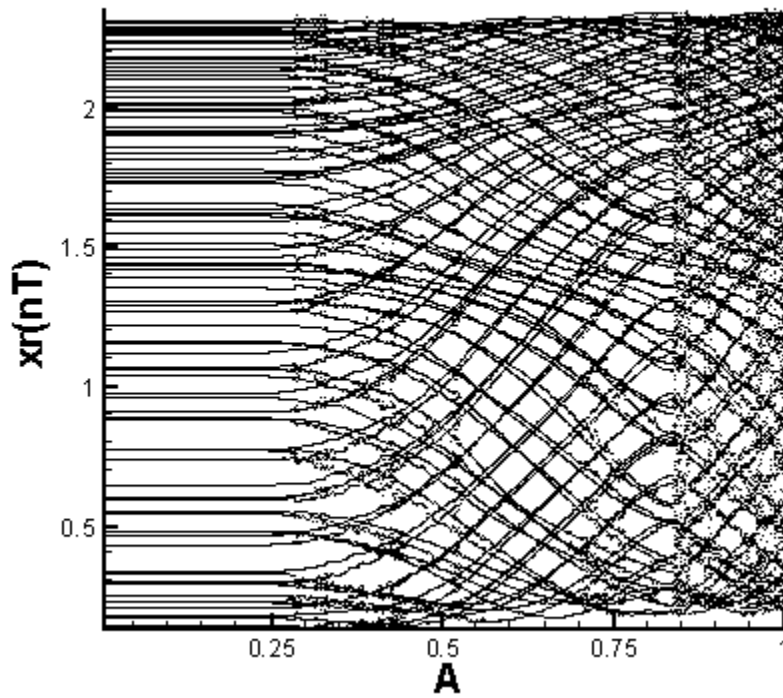
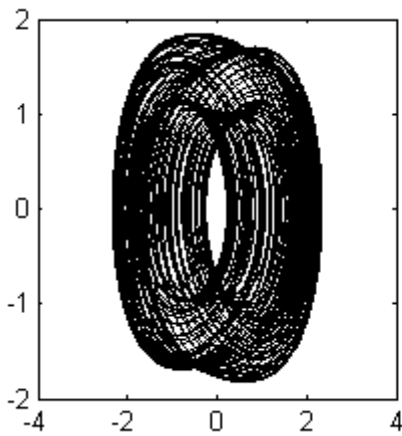
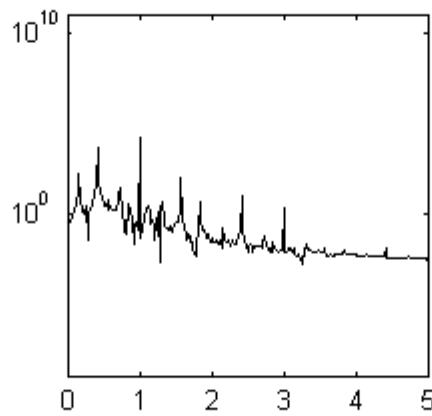


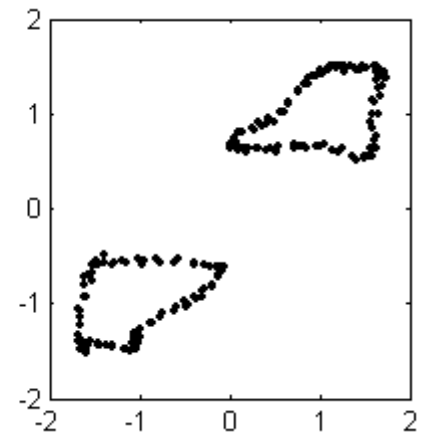
Fig.6 Bifurcation diagrams of gear-bearing system using dimensionless parameter of the depth of crack, A , as bifurcation parameter.



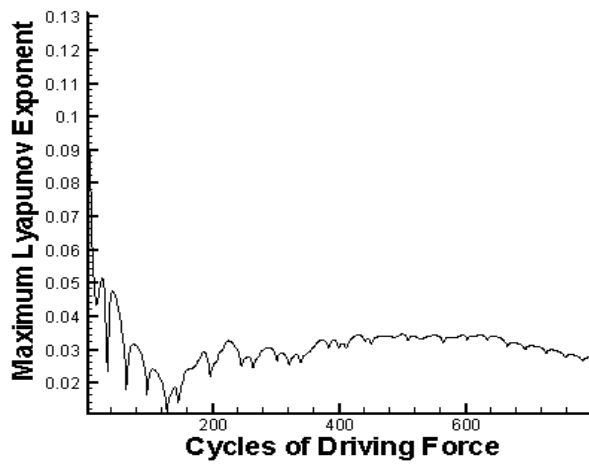
(a) Phase Diagram



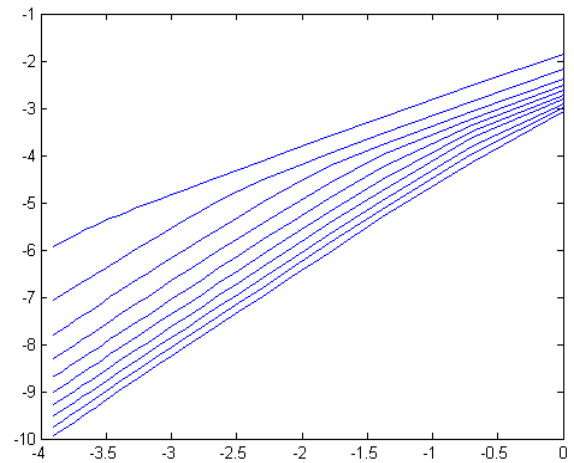
(b) Power Spectrum



(c) Poincaré Map



(d) Lyapunov Exponent



(e) Fractal Dimension

Fig.7 Simulation results obtained for rotor geometric center of gear-bearing system with $A=0.93(x_r)$.

光子晶體光纖之洩漏模態分析

蔣榮生



義守大學 電機工程學系 教授

摘要

本論文提出了一種基於表面積分方程法的全向量數值演算法，通過單獨求解特徵方程的複數傳播係數，對光子晶體光纖(Photonic crystal fiber, PCF)中的洩漏模態進行解析。它可用於計算光子晶體光纖的複數等效折射率和侷限損耗。由於複數解的尋根是分析方法中的關鍵技術，具有該技術的新演算法可用於解決光子晶體光纖的洩漏模態。在文章中分析並討論具有六角形圓形氣孔結構的實芯 PCF 的洩漏模態。由數值結果可知，等效折射率之虛部所計算出的侷限損失如何隨氣孔尺寸、氣孔圈數和波長而變化。藉由增加氣孔尺寸和氣孔數量可以實現減少侷限損失，從所獲得結果可清楚發現，侷限損耗隨波長的增加而增加，這意味著對於更長的波長，

光更容易洩漏；同時，隨著氣孔尺寸 d/Λ 的增加，損耗顯著減小。

關鍵詞：光子晶體光纖、極化分光器、表面積分方程法

前言

洩漏模態是在引導輻射功率中傳播並沿傳播方向指數衰減的模態。在經典光纖中，已知兩種類型的洩漏模態：穿隧洩漏模態，其由於纖芯和纖殼之間的邊界的曲率而產生，並且折射由落入邊界內的光束產生的洩漏模態，其中角度小於臨界角[1]。從歷史記錄來看，洩漏模態概念最早由 Marcuvitz 在 1956 年描述[2]，他注意到量子力學穿隧效應的近似類比。他說明：波動方程在中心範圍的場表示

式，若其解具有複數傳播係數，則該場會在無限橫向空間極限處變為無窮大[3]。1961年，Cassedy和Cohn首次測量了洩漏模態並證實了由於接地介質板上方的線電流源引起的漏洩漏波[4]。一般來說，我們注意到洩漏模態首先在Snyder和Love [1]的教科書中描述。洩漏模態的分析對於設計各種光子和光電元件是實用的，例如凹陷內纖殼單模光纖[5-7]，感測器[8-10]和彎曲光纖[11-13]。

光子晶體光纖(PCF)，也稱為多孔光纖或微結構光纖，因其具有控制光的吸引力優勢而引起了極大的關注[14-16]。PCF由單一材料組成，通常為二氧化矽，沿著光纖軸線在纖芯周圍具有多個氣孔網格。光纖的纖殼由橫截面上的二維周期性氣孔陣列組成，並且纖芯是通過打破週期性結構而形成的中心缺陷。眾所周知，具有打破週期性的某些週期性結構在缺陷處表現出光定位現象[17]。常見的PCF類型是實芯PCF，因為它是易於製作。對於實芯PCF，引導機制是由於修正式全反射，這與傳統光纖中發生的相似。PCF具有許多顯著的特性，例如無限的單模，特殊色散效應，設計靈活性，超連續譜產生，單模區域的極大或小的有效纖芯區域，以及高非線性

[18-21]。PCF的這些顯著特徵在從通信光纖鏈路到光電元件的各種領域中具有廣闊的應用前景。在本文將研究的實芯PCF中，傳播時衰減的模態稱為洩漏模態[22]。由於實芯PCF的折射率分佈類似於W型波導[3]，由於PCF的結構具有高折射率的最外層纖殼，因此沒有真正的侷限模態，這與光纖的纖芯相同。儘管光主要被限制在PCF的纖芯中，但是由於纖殼具有有限數量的氣孔圈，一些光可以通過相鄰氣孔之間的通道洩漏，因此PCF中的一般模態是洩漏的。因此，即使沒有材料吸收或散射損失，侷限損失也是不可避免的。計算上，通過確定對應於複數折射率或傳播係數的向量波方程的洩漏模態解來模擬侷限損失[22]。

基於表面積分方程法(SIEM)[23-26]之有效率數值方法用於分析PCF的傳播特性。SIEM提供非常準確的結果，只需極少量的未知數。SIEM研究由兩個同質材料組成的PCF，只需要考慮兩個材料之間介面的場量。因此，可以顯著減少計算未知數和自由度，並且在不損失精度的情況下提高計算效率。然而，這些論文僅側重於研究傳導模態。在本文中，發展了一種基於SIEM的全向量演算法，用於分析PCF中的洩漏模態。因此

使得SIEM的應用方面會有顯著的擴展。

近年來，已經將幾種數值技術應用於PCF的洩漏模態。2001年，懷特等人[27]通過使用多極點方法計算洩漏模態的侷限損失，該方法用於精確計算具有有限數量氣孔的PCF的複數傳播係數，但它僅限於僅具有圓形的結構孔。有限元素法(FEM)已成功用於模擬PCF的洩漏模態[28-30]。FEM精確且通用，但由於PCF的橫截面必須離散成許多有限元素，因此不可避免地需要大量未知數。因此，FEM需要大量的計算資源，例如記憶體和計算時間。光束傳播方法能夠評估洩漏模態的侷限損失[31]；然而，這種方法在數值上是密集的，並且在區分具有相似傳播係數的模態方面存在困難。

在本論文中，提出了一種基於表面積分方程法的全向量數值演算法，該演算法能夠計算PCF的侷限損失和複數等效折射率。此新演算法可以用有限數量的氣孔模擬PCF的洩漏模態，其能分析等效折射率的虛部的侷限損失如何隨氣孔尺寸、氣孔圈數和波長而變化。

表面積分方程法

表面積分方程法(Surface integral equation method, SIEM)，即為本文應用分析光子晶體光纖相關特性之數值方法，以求得傳播係數與模態場。考慮以光子晶體光纖由兩個均勻區域描述，這兩個區域分別是空氣孔洞以及背景中的二氧化矽。假設 F 代表笛卡爾坐標系中的任何場成分坐標，則 F 是每個區域的亥姆霍茲方程式(Helmholtz equation)的解：

$$\nabla_t^2 F(\bar{r}) + k^2 F(\bar{r}) = 0 \quad (1)$$

其中 F 直角座標中任何場量， ∇_t^2 則為二維拉普拉斯運算子(Laplacian operator)。

依據格林第二恆等式(Green's second identity)，可將定義於一均勻區域 R 中的赫姆霍茲方程式(Helmholtz equation)由微分方程式轉換成積分方程式，適當選擇函數 G 具有 $G = (-j/4)H_0^{(2)}(k|\bar{r} - \bar{r}'|)$ 的形式，為二維格林函數(2-D Green's function)。簡化為下列的形式：

$$F(\bar{r}) = \iint_{\Gamma} \left(F(\bar{r}') \frac{dG(k, \bar{r}, \bar{r}')}{dn} - G(k, \bar{r}, \bar{r}') \frac{dF(\bar{r}')}{dn} \right) d\bar{r}' \quad (2)$$

當 $\bar{r} = \bar{r}'$ 時，上式中格林函數的法向微分會產生一個奇異點(singularity)。為了

避開奇異點，我們可以改變在這個點的積分路徑，將這個點的積分路徑向外變形為一個半圓，並且將半徑趨近於零。經由這樣的處理並且利用漢克函數(Hankel function)的特性，式(3)可以轉換成下列的形式：

$$\frac{1}{2}F(\bar{r}) = P \int_{\Gamma} \left(F(\bar{r}') \frac{dG(k, \bar{r}, \bar{r}')}{dn} - G(k, \bar{r}, \bar{r}') \frac{dF(\bar{r}')}{dn} \right) d\bar{r}' \quad (3)$$

其中 P 為柯西主值積分 (Cauchy principle value integral)。

$$k = \begin{cases} \sqrt{k_0^2 n^2 - \beta^2} & , k_0^2 n^2 > \beta^2 \\ -j\sqrt{\beta^2 - k_0^2 n^2} & , \beta^2 > k_0^2 n^2 \end{cases} \quad (4)$$

k_0, β 代表自由空間之波數與傳播係數。值得注意， k 於Ref.[23]中可以是實數或純虛數，然而在本論文中是採用複數值的形式，由於 β 也是洩漏模態的複數值。表面積分方程法的全向量數值演算法，通過單獨求解特徵方程的複數傳播係數，對光子晶體光纖中的洩漏模態進行解析。它可用於計算光子晶體光纖的複數等效折射率和侷限損耗。由於複數解的尋根是分析方法中的關鍵技術，具有該技術的新演算法可用於解決光子晶體光纖的洩漏模態。對於洩漏模態的複數橫面波數 k 可由下式獲得：

$$k = \pm \sqrt{k_0^2 n^2 - \beta^2} \quad (5)$$

數值分析

為了驗證基於SIEM的全向量數值演算法的有效性，首先計算如圖1(a)中所示的二氧化矽實芯PCF的侷限損失。氣孔間距 Λ 為6.75微米，氣孔直徑 d 為5.0微米， $\lambda = 1.45$ 微米， $n_s = 1.45$ 。圖1(b)，(c)顯示兩個氣孔圈的PCF的基本模態 HE_{11} 之磁場向量實部的分佈和虛部的場強分佈。

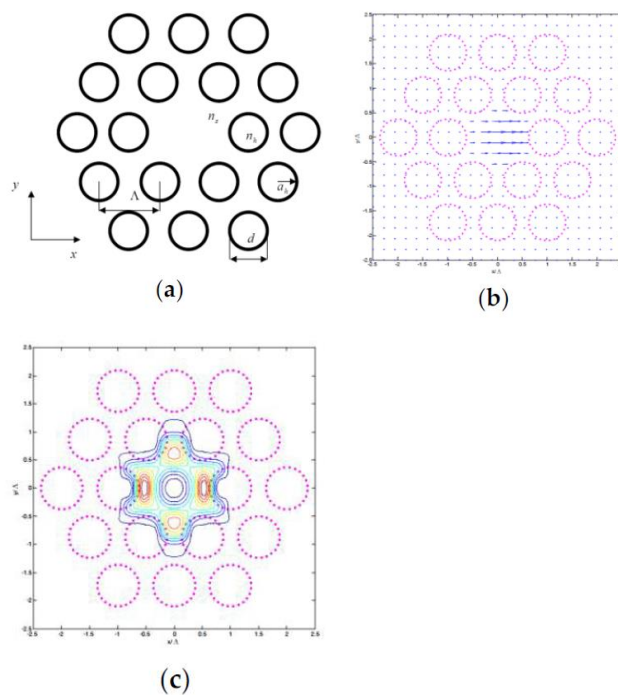


圖1 (a)二氧化矽實芯光子晶體光纖的截面示意圖。

(b)基本模態 HE_{11} 之磁場向量實部分佈。

(c)基本模態之磁場場強的虛部分佈。

同時SIEM也可以解出PCF全部二階模態： TE_{01} ， HE_{21} 和 TM_{01} 模態的實部和虛部的磁場場強分佈，如圖2所示。

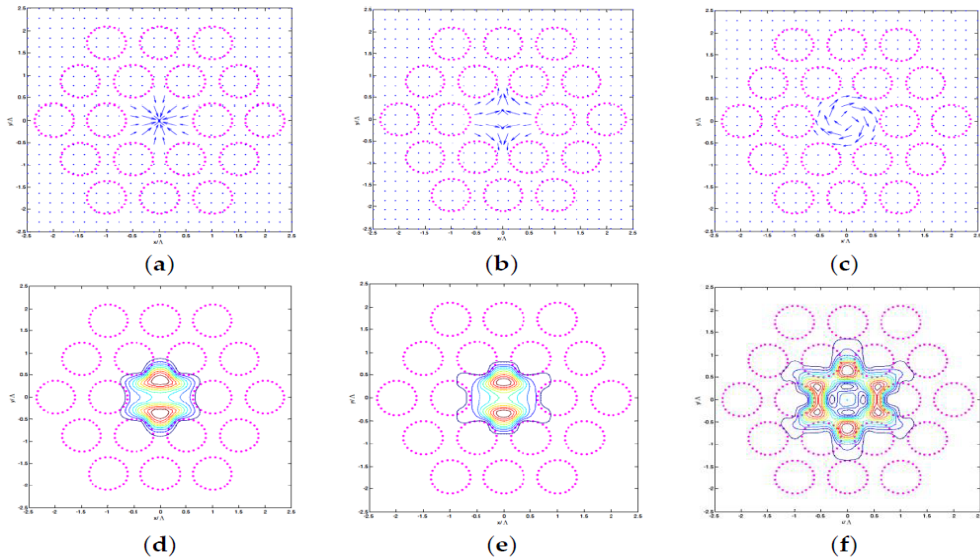


圖2 二階模態橫面磁場向量場實部分佈之(a)TE₀₁, (b)HE₂₁, (c)TM₀₁模態

;(d)TE₀₁, (e)HE₂₁, (f)TM₀₁模態之虛部的磁場場強分佈在具有18個氣孔的PCF。

表格1顯示上述模態利用SIEM與多極點法[27]獲得的精確結果的直接比較，可以通過量化模態場量來檢定每種模態。

表1.表面積分方程法和圖1(a)中的多極點法[27]的模態等效折射率和侷限損失的比較

Mode Class	SIEM n_{eff}	Loss (dB/m)	Multipole Method n_{eff}
HE ₁₁	$1.4453471152 + i2.684 \times 10^{-8}$	1.01	$1.4453471163 + i2.578 \times 10^{-8}$
TE ₀₁	$1.4384402631 + i4.062 \times 10^{-7}$	15.29	$1.4384402675 + i4.101 \times 10^{-7}$
HE ₂₁	$1.4383130349 + i6.974 \times 10^{-7}$	26.25	$1.4383130373 + i6.898 \times 10^{-7}$
TM ₀₁	$1.4382295027 + i1.256 \times 10^{-6}$	47.28	$1.4382295029 + i1.268 \times 10^{-6}$

傳播係數 β 與傳播模態等效折射率 n_{eff} 有 $\beta=(2\pi/\lambda) \cdot n_{eff}$ 等式關係。SIEM演算法產生複數等效折射率，獲得侷限損失可以如下計算式[32]：

$$\text{Loss (confinement loss: dB/m)} = \frac{20 \times 10^6}{\ln 10} \frac{2\pi}{\lambda} \text{Im}[n_{eff}]$$

由表格1所示結果，可清楚展現本文提出之演算法與多極點法在侷限損失和複數等效折射率具有顯著的一致性。在通過收斂性驗證後，可得知SIEM可獲得準確的解析並節省計算時間。

圖3顯示了具有2個氣孔圈(18個氣孔)的PCF的基本洩漏模態的色散曲線(複數等效折射率與波長關係)，其中 $n_{\text{silica}} = 1.45$ 及 $d/\Lambda = 0.74$ (氣孔尺寸大小)。由於在實際的光子晶體光纖皆為有限數量的氣孔圈，因此所有模態都會形成洩漏洩漏模態，其可由 n_{eff} 的虛部計算獲得侷限損失。由圖3可知洩漏模態的曲線位置就位於 n_{eff} 曲線的虛部。

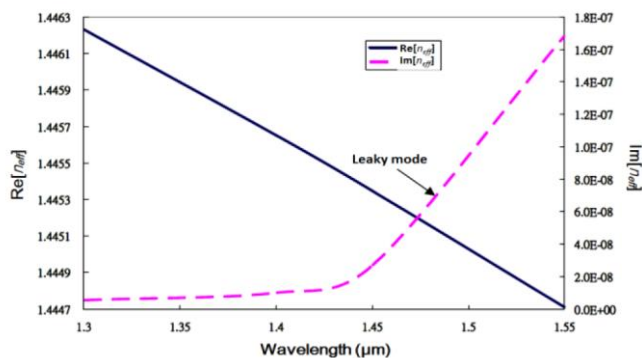


圖3 具有2個氣孔圈的PCF的基本洩漏模態的色散曲線圖

圖4(a)顯示具有六角形圓形氣孔結構的實芯PCF的示意截面圖，它由嵌入二氧化矽的4個氣孔圈(60個氣孔)形成(折射率 $n_{\text{silica}} = 1.46$)，其中 d/Λ 是氣孔尺寸(d 是氣孔直徑； Λ 是氣孔間距)。而圖4(b)則展示具有2個氣孔圈(18個氣孔)的PCF的基本洩漏模式的強度分佈，其 $d/\Lambda = 0.4$ 和 $\lambda/\Lambda = 0.5$ 。由圖可以清楚地看到六邊形對稱性和由於氣孔中斷引起的能量的洩漏。能量場侷限取決於氣孔尺寸和氣孔圈數。從表格1中的模態類別的結果可以發現，高階

模態比基本模態具有更大的侷限損失。

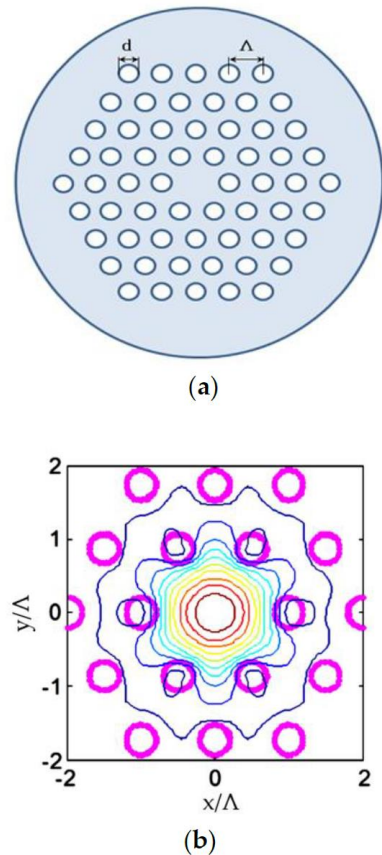


圖4 (a)具有4個氣孔圈(60個氣孔)的PCF的示意圖， d/Λ 是氣孔尺寸，背景材料是二氧化矽。
(b)具有2個氣孔圈， $d/\Lambda=0.4$ 和 $\lambda/\Lambda=0.5$ 的PCF的基本洩漏模式的強度分佈。

圖5顯示具有 $n_{\text{silica}}=1.46$ 和 $d/\Lambda=0.6$ 的2圈氣孔PCF的基本模態 n_{eff} 的波長響應。結果表示隨著波長的增加， n_{eff} 的實部減少， n_{eff} 的虛部顯著增加。

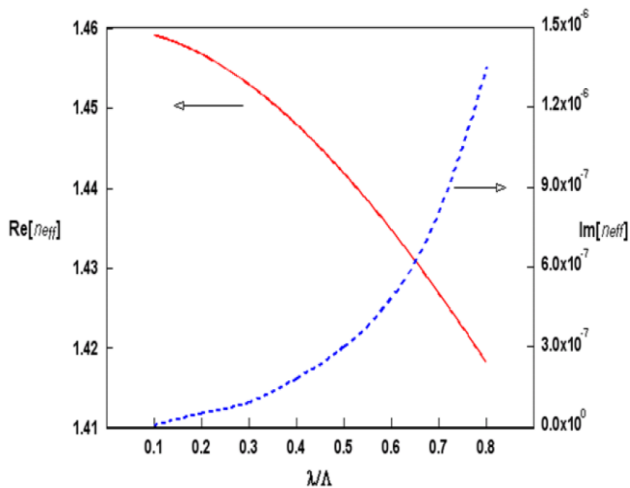


圖5 18個氣孔PCF, n_{eff} 的實部(實線)和虛部(虛線)的波長響應圖

圖6展示侷限損失與氣孔尺寸 d/Λ 的關係，對於 $\lambda/\Lambda=0.5$ 的各種數量氣孔圈。隨著氣孔尺寸和氣孔圈的數量，侷限損失單調遞減。可以看出，小的氣孔尺寸和較少數量的氣孔都會引起較大的損失，但是如果氣孔尺寸增大或者採用更多的氣孔，則會迅速減少。圖6的插圖顯示了折射率分佈。纖芯的折射率 n_1 等於外纖殼層，而內纖殼層的折射率 n_2 小於 n_1 。纖芯和內纖殼的半徑分別用 a 和 b 表示。因為PCF的結構具有高折射率的最外層纖殼，其折射率等於纖芯，因此沒有真正的侷限模態。由於氣孔提供侷限場量的低折射率，通過增加氣孔尺寸或氣孔數量來減少損失表明內纖殼具有較低的折射率或較大的半徑。

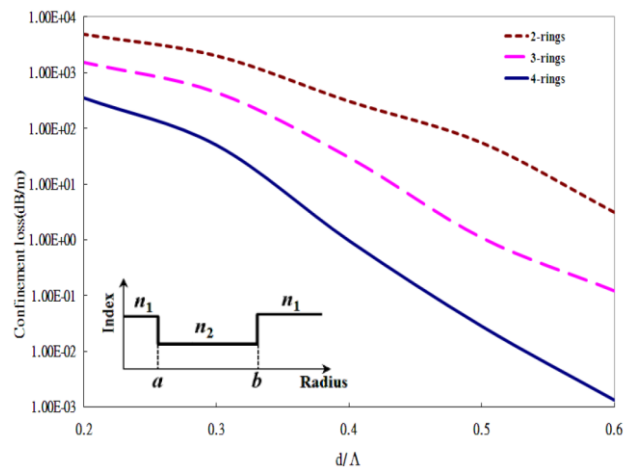


圖6 PCF實芯纖芯周圍各種氣孔圈數的侷限損失與氣孔尺寸 d/Λ 的關係圖

圖7顯示3個氣孔圈(36個氣孔)PCF的各種氣孔尺寸 d/Λ 的損耗波長關係圖。它們表明侷限損失隨著波長增加，這意味著對於更長波長，光能量洩漏更容易增加。同時可以發現，隨著氣孔尺寸 d/Λ 的增加，損失顯著減小。

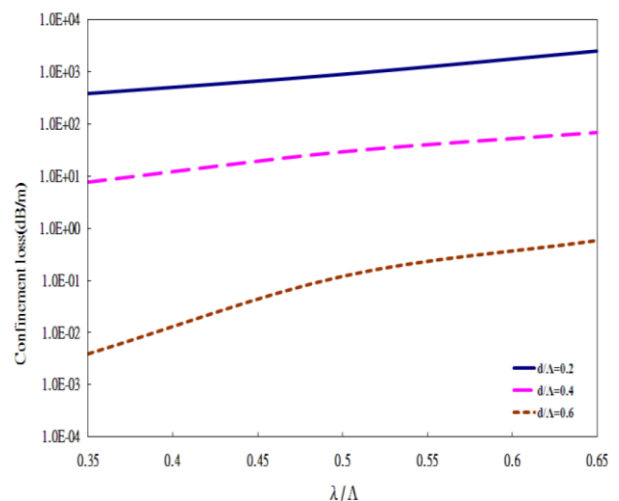


圖7 PCF實芯纖芯3個氣孔圈(36個氣孔)不同氣孔尺寸 d/Λ 的損耗波長關係圖

結論

本論文提出了一種基於表面積分方程法的全向量數值演算法，通過單獨求解特徵方程的複數傳播係數，對光子晶體光纖的洩漏模態進行解析。該數值演算法產生了用於處理有限數量的氣孔的有效程式，它可用於計算光子晶體光纖的複數等效折射率和侷限損耗。由於複數解的尋根是分析方法中的關鍵技術，具有該技術的新演算法可用於解決光子晶體光纖的洩漏模態。因為 PCF 的結構具有高折射率的最外層纖殼，其折射率等於纖芯，因此沒有真正的侷限模態，因此所有模態都屬於洩漏模態。本文分析並討論具有六角形圓形氣孔結構的實芯 PCF 的洩漏模態。由數值結果可知，等效折射率之虛部所計算出的侷限損失如何隨氣孔尺寸、氣孔圈數和波長而變化。藉由增加氣孔尺寸和氣孔數量可以實現減少侷限損失，從所獲得結果可清楚發現，侷限損耗隨波長的增加而增加，這意味著對於更長的波長，光更容易洩漏；同時，隨著氣孔尺寸 d/Λ 的增加，損耗顯著減小。表明侷限損失隨著波長增加，這意味著對於更長波長，光能量洩漏更容易增加。同時可以發現，隨著氣孔尺寸 d/Λ 的增加，損失顯著減小。

參考文獻

- [1] Snyder, A.W.; Love, J.D. Optical Waveguide Theory; Kluwer Academic Publishers: Norwell, MA, USA, 1983.
- [2] Marcuvitz, N. On field representations in terms of leaky modes or eigenmodes. IRE Trans. Antennas Propag. 1956, 4, 192–194.
- [3] Hu, J.; Menyuk, C.R. Understanding leaky modes: Slab waveguide revisited. Adv. Opt. Photonics 2009, 1, 58–106.
- [4] Cassedy, E.S.; Cohn, M. On the existence of leaky waves due to a line source above a grounded dielectric slab. IRE Trans. Microw. Theory Tech. 1961, 9, 243–247.
- [5] Maeda, M.; Yamada, S. Leaky modes on W-fibers: Mode structure and attenuation. Appl. Opt. 1977, 16, 2198–2203.
- [6] Renner, H. Leaky-mode loss in coated depressed-cladding fibers. IEEE Photonics Technol. Lett. 1991, 3, 31–32.
- [7] Chou, C.C.; Sun, N.H. Analysis of leaky-mode losses for optical fibers.

- J. Opt. Soc. Am. B 2008, 25, 545–554.
- [8] Harris, J.; Lu, P.; Larocque, H.; Chen, L.; Bao, X. In-fiber Mach–Zehnder interferometric refractive index sensors with guided and leaky modes. *Sens. Actuators B Chem.* 2015, 206, 246–251.
- [9] Liu, Q.; Li, S.; Chen, H.; Fan, Z.; Li, J. Photonic crystal fiber temperature sensor based on coupling between liquid-core mode and defect mode. *IEEE Photonics J.* 2015, 7, 1–9.
- [10] Gao, R.; Lu, D.F.; Cheng, J.; Jiang, Y.; Jiang, L.; Qi, Z.M. Humidity sensor based on power leakage at resonance wavelengths of a hollow core fiber coated with reduced graphene oxide. *Sens. Actuators B Chem.* 2016, 222, 618–624.
- [11] Wang, P.; Semenova, Y.; Wu, Q.; Farrell, G.; Ti, Y.; Zheng, J. Macrobending single-mode fiber-based refractometer. *Appl. Opt.* 2009, 48, 6044–6049.
- [12] Lu, P.; Chen, Q. Femtosecond laser microfabricated fiber Mach–Zehnder interferometer for sensing applications. *Opt. Lett.* 2011, 36, 268–270.
- [13] Zhang, X.; Peng, W. Fiber optic refractometer based on leaky-mode interference of bent fiber. *IEEE Photonics Technol. Lett.* 2015, 27, 11–14.
- [14] Knight, J.C.; Birks, T.A.; Russell, P.S.J.; Atkin, D.M. All-silica single-mode optical fiber with photonic crystal cladding. *Opt. Lett.* 1996, 21, 1547–1549.
- [15] Broeng, J.; Mogilevstev, D.; Barkou, S.E.; Bjarklev, A. Photonic crystal fibers: A new class of optical waveguides. *Opt. Fiber Technol.* 1999, 5, 305–330.
- [16] Chiang, J.S.; Wu, T.L. Analysis of propagation characteristics for an octagonal photonic crystal fiber (O-PCF). *Opt. Commun.* 2006, 258, 170–176.
- [17] Ferrando, A.; Silvestre, E.; Miret, J.J.; Andres, P.; Andres, M.V. Vector description of higher-order modes in photonic crystal fibers. *J. Opt. Soc. Am. A* 2000, 17, 1333–1340.

- [18] Birks, T.A.; Knight, J.C.; Russell, P.S.J. Endlessly single-mode photonic crystal fiber. *Opt. Lett.* 1997, 22, 961–963.
- [19] Broderick, N.G.R.; Monro, T.M.; Bennett, P.J.; Richardson D.J. Nonlinearity in holey optical fibers: Measurement and future opportunities. *Opt. Lett.* 1999, 24, 1395–1397.
- [20] Knight, J.C. Photonic crystal fibres. *Nature* 2003, 424, 847–851.
- [21] Cregan, R.F.; Mangan, B.J.; Knight, J.C.; Birks, T.A.; Russell, P.S.J.; Roberts, P.J.; Allan, D.C. Single-mode photonic bandgap guidance of light in air. *Science* 1999, 285, 1537–1539.
- [22] Zolla, F.; Renversez, G.; Nicolet, A.; Kuhlmeij, B.; Guenneau, S.; Felbacq, D. *Foundations of Photonic Crystal Fibres*; Imperial College Press: London, UK, 2005.
- [23] Su, C.C. A surface integral equations method for homogeneous optical fibers and coupled image lines of arbitrary cross sections. *IEEE Trans. Microw. Tech.* 1985, 33, 1114–1119.
- [24] Yang, W.; Gopinath, A. A boundary integral method for propagation problems in integrated optical structures. *IEEE Photonics Technol. Lett.* 1995, 7, 777–779.
- [25] Wu, T.L.; Chiang J.S.; Chao, C.H. A novel approach for calculating the dispersions of photonic crystal fibers. *IEEE Photonics Technol. Lett.* 2004, 16, 1492–1494.
- [26] Chiang, J.S.; Wu, T.L. Analysis of an ultrashort PCF-based polarization splitter. *J. Light. Technol.* 2010, 28, 707–713.
- [27] White, T.P.; McPhedran, R.C.; de Sterke, C.M.; Botten, L.C.; Steel, M.J. Confinement loss in microstructured optical fibers. *Opt. Lett.* 2001, 26, 1660–1662.
- [28] Ferrarini, D.; Vincetti, L.; Zoboli, M.; Cucinotta, A.; Selleri, S. Leakage properties of photonic crystal fibers. *Opt. Express* 2002, 10, 1314–1319.
- [29] Zhang, Z.; Shi, Y.; Bian, B.; Lu, J. Dependence of leaky mode coupling on loss in photonic crystal

fiber with hybrid cladding. *Opt. Express* 2008, 16, 1915–1922.

[30] Gu, G.; Kong, F.; Hawkins, T.W.; Foy, P.; Wei, K.; Samson, B.; Dong, L. Impact of fiber outer boundaries on leaky mode losses in leakage channel fibers. *Opt. Express* 2013, 21, 24039–24048.

[31] Steel, M.J.; Osgood, R.M., Jr. Polarization and dispersive properties of elliptical-hole photonic crystal fibers. *J. Light. Technol.* 2001, 19, 495–503.

[32] Finazzi, V.; Monroe, T.M.; Richardson, D.J. Small-core silica holey fibers: Nonlinearity and confinement loss trade-offs. *J. Opt. Soc. Am. B* 2003, 20, 1427–1436.

物聯網系統架構與應用開發簡介



廖冠雄

義守大學 資訊工程學系 助理教授

摘要

物聯網(Internet of Things, 簡稱IoT)系統整合了各項仍在持續快速進步的資通訊技術, 成為繼工業革命以及電腦發明之後, 再度讓人類生活產生大幅進化的基石。近年來物聯網的產品以及衍生出的環境, 已經開始逐漸融入各種產業以及日常生活中, 各種智慧型應用系統也逐漸成形, 例如智慧製造、智慧居家、智慧醫療、智慧運輸、智慧農業等等。本文的主要目的是針對物聯網系統的參考架構, 以及物聯網應用系統開發實務進行說明, 期能建立讀者對物聯網系統技術的基本概念。

前言

由於電腦科學與網路通訊技術的快速發展, 今日我們的生活已經離不開這兩項技術所衍生的相關產物。例如, 我們每天都會使用手機或電腦來上網, 透過社群軟體或即時通訊軟體(如 Facebook、Line 等)與親朋好友分享生活資訊與線上交談, 透過電子郵件與公司行號往來業務訊息, 透過網頁瀏覽器或手機 APP 得知新聞消息、進行網路購物、查詢公車時刻表等等。而近年來在感測技術上的進步, 除了人與人之間的訊息交換之外, 我們也逐漸可以透過網路與各種實體(包含物品與環境)做資訊交換, 亦即與所謂的「物」(Things)作連網交談, 最後達到萬物皆可上網互通的目標, 這就是所謂的「物聯網」。

物聯網的重要性在於其可應用於各種民生與產業領域，發展出過去所沒有的新型智慧應用服務，例如：智慧農業、智慧工廠、智慧運輸、智慧能源管理、智慧醫療、...等等(如圖 1)，將人類的文明從電腦發明後的資訊時代，再度提升到另一個與環境緊密互動的新時代，使得各種產業得以更有效率的發展，而且創造出更加便利的生活環境。

本文即針對物聯網系統的參考架構以及實務開發進行簡要說明，期能建立讀者對於物聯網技術的基本概念。

物聯網系統參考架構

物聯網的主要目的是透過各種感測、網通、運算等技術的整合，形成物與人之間全面互動的環境，讓我們可以在這個基礎上，針對各種領域發展新式應用服務，因此物聯網系統的架構當然主要是由感測、網通、運算等技術元件所構成。然而隨著應用場域與效能需求上的變化，物聯網的架構至今並沒有統一的標準規範，但綜合各物聯網發展組織與學界研究成果來看 [1-5]，一般公認基本的物聯網系統為如圖 2 的三層式架構，包含感知層

(Perception Layer)、網路層(Network Layer)、以及應用層(Application Layer)。

感知層主要包含了環境資訊感測元件以及資訊傳遞網路所形成的子系統，其主要功能為感測各式環境資訊，並將這些資訊透過網路層所提供的通訊平台匯集到後端的應用層，也可以接受來自應用層的指令，對感測元件進行特定的控制。感知層的主要組成元件包括：

- 感測器(Sensor)與致動器(Actuator)：

感測器的主要功能是量測各種環境(包含人體)資訊，例如：溫度、濕度、空氣微粒量、體溫、血壓、血糖等等，並將量測到環境資訊轉換成對應的數值，透過感測器網路或特定的通訊界面，將數值經由網路層傳遞到後端的應用服務系統中。致動器則是可以接受來自外部的控制信號，進行指定的動作，例如：馬達、水閘、燈號、加熱器等等。後端的應用服務系統可以發出指令給致動器，進行指定動作。而致動器與感測器之間也可以互相傳遞資訊，來完成某個特定的功能。另外，已經大量運用於物流業貨品追蹤的射頻識別(RFID)標籤，往往也被視為是一種感測器，因為其內部攜帶了貨品的相關資訊，可經由讀

取器(Reader)的讀取將資訊傳遞到應用服務系統，也可將特定資訊寫入RFID 標籤中，相當於感測器與致動器的角色。

- 感測器網路(Sensor Network)：

因為感測器大都是布建在特定地點，且其主要任務僅為感知環境資訊並轉換成對應的數值資料，再透過通訊界面(通常是無線網路)做資料傳遞。故感測器往往都是由電池供應電力的嵌入式模組來實現，除了有限的運算能力與儲存空間之外，其無線通訊界面的傳送範圍也不大。然而通常在一個區域內的感測器布建數量不會只有一兩個，所以可以採用專為群組感測器傳遞資料所設計的無線感測器網路(例如：Zigbee)，透過感測器之間所形成的網狀拓撲結構，讓感測器彼此可以互相協助轉傳資料到指定的感測器或資料收集點。

- 閘道器(Gateway)：

由於感測器多為簡易功能的模組所組成，沒有能力將資料透過網際網路傳遞到後端應用服務系統，因此需要布建一個專門的資料收集點，即閘道器，來收集特定範圍內的所有感測器資訊，再由閘道器將匯集的資料送到後端。而後端應用服務也可透過閘道器來控制感測器或致動器。除此

之外，不同無線通訊介面規格的感測器之間(例如：藍芽與 Zigbee)，也可透過閘道器來互相交換資料。另一方面，近年來在物聯網架構理論中興起的「邊緣運算」(Edge computing) [6]，即是將某些需要即時性反應的特定功能及其所需要的運算，在靠近感測器的資料收集裝置(通常是閘道器)執行，以提升反應速度並形成分散式服務架構，提升整體服務效能，因此閘道器在未來的物聯網架構中將扮演重要的角色。

網路層的主要功能是提供感知層與應用層之間的資料交換通道，在架構上包含兩個部分，一為讓感知層與應用層的各項元件可以連結上網際網路(Internet)的接取網路(Access Network)，另一則是現有的網際網路平台。接取網路包括各式有線或無線的連網技術，例如乙太網路(Ethernet)、藍芽(Bluetooth)、Wi-Fi 無線區域網路、3G/4G/5G 行動通訊網路、LPWAN 長距離低功耗無線網路等等。

應用層則是透過網路層匯集來自感知層的感測資料，並向感知層傳遞控制訊息以實現特定應用服務的子系統。應用服務中的各種功能以軟體來實現，其中並包含管理者與

使用者的操作介面(例如網頁、圖形介面等等)。為提供系統發展上的彈性，開發與運作平台可以大量採用現有雲端運算技術以及大數據運算/儲存技術來實現。應用服務的發展重點，在於運用所收集到的感測資訊以及各式自動化技術，設計出智慧型新穎服務，應用在農業、居家、城市管理、醫療、製造等不同領域。

物聯網系統開發實務

以上一節的三層式物聯網架構為基礎，實際的物聯網系統組成可依此設計並選用適當的元件來實現，如圖 3 所示。

在感知層中的裝置主要是執行環境資訊感測以及接受命令執行動作的感測節點。一般來說，感測節點是以微控制器或微處理器作為運算核心，執行程式來控制感測元件或致動元件，並透過通訊界面與外界交換資訊，傳輸感測資訊或接收遠端命令。在工業應用上，有時會以可程式控制邏輯器(Programmable Logic Controller, 簡稱 PLC)做為控制核心。

目前市面上已有相當多專門的物聯網感測節點開發板，除了硬體之外也提供整合式軟體開發環境，以加速

感測節點雛型系統的開發，也可直接作為感測節點的主體。有些開發板以時脈不高(大約十幾到數百 MHz)且記憶體僅數百 K Bytes 的微控制器作為運算核心，例如 Arduino[7]系列、聯發科 Linkit 7697 系列[8]等等。此類開發板大都無作業系統，或是只能運行專門的嵌入式作業系統(例如 mbed[9]、FreeRTOS[10]、Nucleus RTOS[11]等等)。有些開發板則是較微控制器高階一些，以時脈為數百 MHz 的 MIPS 或 ARM 處理器，並搭配 Wi-Fi 或 Bluetooth 等無線網路界面的 SoC 做為運算核心，例如以樂鑫 ESP8266 或 ESP32[12]晶片為核心的開發板，或是以聯發科 MT7688[13]晶片為核心的開發板皆屬於此類。此類開發板通常具有容量較大的記憶體，因此可以運行如 embedded Linux 等功能較強大的作業系統，也支援使用更高階的程式語言(如 Python、Lua 等等)做程式編撰。最後，有些更高階的開發板則屬於單板電腦系統，例如 Raspberry Pi [14]、BeagleBoard [15]、研揚 Up Board[16]等等，其運算能力除了可以執行感測節點任務之外，也相當適合作為閘道器的開發平台。近年來，由於人工智慧與深度學習的軟硬體技術的快速發展，已開始出現適合作為邊緣運算閘道器的開發板，如 Nvidia Jetson Nano [17]

等，搭載 GPU 處理器，可執行複雜的人工智慧運算。

網路層的組成可分成兩個部分來探討。首先考慮感知層的通訊連結，即圖 3 中的鏈結層網路 (Link-Layer Network)。鏈結層網路為傳遞資料訊息的實體網路，其主要任務有二：(1)實現感測器、致動器、以及閘道器之間相互通訊；(2)作為感知層連結到網際網路的橋樑，也就是實現接取網路的功能。

就感知層內的裝置互相通訊來說，由於感測節點大都布建於待量測資訊的所在地，且並非所有地點都能夠以有線的方式提供電源與通訊，因此以電池作為電力來源，以及採用無線網路作為資料通道為較適合的作法。適於物聯網應用的無線網路應具備以下特性：(1)具有低耗電量的設計；(2)可應付大量感測節點裝置(數千至數萬)傳遞量測資訊；(3)低複雜度，可於嵌入式系統中運行；(4)成本低廉，適合大量生產。

目前常用於物聯網感知層的無線網路技術主要有：

- 以 IEEE 802.15.4 為基礎者：包含 Zigbee、6LoWPAN[18]、以及工業用的 WirelessHART、ISA100.11a、WIA-PA[19]等等。

- Wi-Fi 無線區域網路：即目前通用的 IEEE 802.11 系列的無線區域網路，但因其單一網路可容納裝置數不多(大約數十個)，且耗電量相對較大，傳送範圍有限(最大 100 公尺)，因此較不適合需要大量感測裝置的應用。
- Wi-Fi HaLow[20]低功耗無線區域網路：IEEE 802.11 工作群組因應物聯網需求制訂了 802.11ah 標準[21]，Wi-Fi 聯盟即採用了 802.11ah 作為主體定義了 HaLow 低功耗無線區域網路規範。
- 低功耗藍芽(Bluetooth Low Energy，簡稱 BLE)：藍芽的規格自 4.0 版之後，針對物聯網感測節點的需求，加入了 BLE 規範，提供更簡化以及更省電的資料傳輸機制。
- 長距離低功耗無線廣域網路(Low-Power Wide-Area Network，簡稱 LPWAN)：前述各種物聯網無線網路的最大傳輸距離僅大約 1 公里左右，為因應大範圍(數公里~十幾公里)感測數據的無線傳輸需求，已有多項 LPWAN 技術被開發出來，包括：
 - 使用非授權頻譜者：有 LoRaWAN[22]、Sigfox[23]、Weightless[24]、Ingenu[25]等等。
 - 使用授權頻譜者：即原有行動通

訊規格的再延伸，如 3GPP 所發展的 LTE-M 以及 NB-IoT[26]，可融入現有行動通訊系統中提供服務，兩者也都已經納入未來 5G 行動通訊系統中。

表 1 為上述各項感知層無線網路技術的比較，物聯網系統規劃者應以實際場域環境狀態以及應用領域選用合適的技術。

至於感知層連結到網際網路的部分，現有的接取網路技術皆可以應用於感知層與網路網路的介接，例如：有線的 Ethernet、VDSL、FTTx 等，以及無線的 Wi-Fi、3G/4G/5G 行動通訊網路等。其實務發展的關鍵課題在於必須根據所採用的感知層軟硬體平台技術，來決定介接到網際網路的架構。例如當感測節點使用 Zigbee 作為鏈結層網路時，那麼就需要布建一個具有 Zigbee 介面與接取網路介面的閘道器，作為 Zigbee 感測網路與網際網路的中介點，將匯集自感測裝置的資料以指定的資料交換格式，透過網際網路傳送到後端的應用系統，也將來自後端應用系統的命令，轉送到 Zigbee 感測網路中的指定裝置。但若感測節點本身即可透過鏈結層的網路介面直接連接到網際網路，例如 Wi-Fi 無線區域網路介面，且其韌體也具備與後端應用

系統直接交換資料的能力，那麼就不需要布建閘道器，直接讓感測裝置與應用系統溝通即可。

接下來談網路層的另一部分，也就是網際網路部分。網際網路是物聯網架構內統一的資料交換網路。以 ISO OSI(Open System Interconnection)分層式網路協定模型來看，如同我們早已熟知，網際網路以 IP 作為網路層協定，並以 TCP 與 UDP 作為傳輸層協定。然而在物聯網系統中，為了符合感測裝置與後端應用系統間的資料交換需求，必須要有專屬的應用層協定來達到這個目的。已成為 Web 服務基石的 HTTP 協定[27]當然可以用來作為物聯網的資料交換協定，然而由於 HTTP 的運作模式為嚴格的「客戶端-伺服器」(Client-Server)模式，資料交換必須由客戶端主動提出「要求」(Request)訊息再由伺服器端傳回「回應」(Response)訊息的方式來進行，缺乏可以讓感測裝置對於環境資訊的變化作主動回報的「事件通報」(Event Notification)模式，且 HTTP 為純文字型態的協定，其訊息標頭(Header)過於冗長，因此只能適用於物聯網閘道器與後端應用系統之間，或是應用系統內各軟體模之間的資料交換，而不適合用來作為感知層與應用層之間的一般性資料交換

協定。

目前在物聯網系統中最為廣泛採用的資料交換協定為 CoAP (Constrained Application Protocol)[28] 以及 MQTT (Message Queuing Telemetry Transport)[29]。CoAP 是參考 HTTP 所設計之符合物聯網需求的資料交換協定，讓資源有限的感測裝置可透過 CoAP 與外界交換資訊。CoAP 仍承襲 HTTP 的 Request/Response 模式來交換資料(如圖 4 所示)，但新增了事件通知的功能，且其改採 UDP 作為傳輸層協定，並大幅縮短標頭結構，使得 CoAP 可以運作於感測裝置之中。

然而即使感測裝置使用 CoAP 來做資料交換，當同時有多個其他裝置或應用程式都想要取得這個裝置的資訊時，這個裝置仍必須逐一分別把資訊傳出，這樣仍可能會導致感測裝置負荷過重，此時採用 MQTT 協定便可避免此種困擾。在使用 MQTT 協定時，我們必須建置一個資料匯集與發佈的伺服器—MQTT Broker，感測裝置將量測到的資料，使用「Publish」(發布)命令將該資料冠以一個特定的標題 (Topic)傳送到 MQTT Broker。若一個裝置或應用程式想要取得該標題所對應的資料時，就先以「Subscribe」(訂閱)命令向 MQTT Broker「訂閱」這個標

題，則 MQTT Broker 一旦收到感測裝置「發布」的這個標題的資料，就會自動轉送到有訂閱此標題的裝置或應用程式(如圖 5 所示)。因此，感測裝置只要發布一次資料到 MQTT Broker 即可，由 MQTT Broker 將資料轉送給需求者。MQTT 的缺點在於其所使用的傳輸層協定為 TCP，較 UDP 耗用系統資源，且需要建置一個 MQTT Broker 伺服器來匯集與轉送資料，而轉送的過程可能會產生較長的時間延遲，對於需要嚴格即時反應的應用場域來說較不適合。

應用層即是根據想要達到之智慧應用的需求規格，選用合適的平台來實現所需的應用系統。在平台內必須具備下列支援性質的基礎功能，以供上層各項應用服務來運用：(1)感測裝置資料收集與訊息交換、(2)感測資料儲存與提取、(3)資料運算輔助模組(如統計運算、大數據處理、機器學習等)。由於一個完整的物聯網智慧應用服務的系統開發相當龐大複雜，因此目前一些大型的雲端運算平台，如 Microsoft Azure、Amazon AWS、Google GCP、IBM Bluemix 等等，都有提供結合上述各項基本功能的雲端應用開發平台，提供良好便捷的開發環境以及豐富的功能支援，甚至也提供感測裝

置程式開發所需的程式庫，使得開發者可專注於物聯網應用服務本身的前後端整合實現以及後續的系統維運。

參考文獻

- [1] H. P. Breivold, “A Survey and Analysis of Reference Architectures for the Internet-of-things,” ICSEA 2017, Oct. 2017, Athens, Greece.
- [2] D. Singh, G. Tripathi, and A. J. Jara, “A survey of Internet-of-Things: Future vision, architecture, challenges and services,” 2014 IEEE World Forum on Internet of Things (WF-IoT), Mar. 2014.
- [3] A. Al-Fuqaha, M. Guizani, M. Mohammadi, M. Aledhari, and A. Ayyash, “Internet of Things: A Survey on Enabling Technologies, Protocols, and Applications,” IEEE Communication Surveys & Tutorials, vol. 17, no. 4, 2015.
- [4] P. Sethi and S. R. Sarangi, “Internet of Things: Architectures, Protocols, and Applications,” Journal of Electrical and Computer Engineering, 2017.
- [5] B. N. Silva, M. Khan, and Kijun Han, “Internet of Things: A Comprehensive Review of Enabling Technologies, Architecture, and Challenges,” IETE Technical Review, vol. 35, no. 2, 2018.
- [6] P. G. Lopez, et al., “Edge-centric Computing: Vision and Challenges,” ACM SIGCOMM Computer Communication Review, vol. 45, no. 5, Oct. 2015.
- [7] <https://www.arduino.cc/>
- [8] <https://labs.mediatek.com/zh-tw/platform/linkit-7697>
- [9] <https://www.mbed.com>
- [10] <https://www.freertos.org/>
- [11] <https://www.mentor.com/embedded-software/nucleus/>
- [12] <https://www.espressif.com/en/products/hardware/esp32/overview>
- [13] <https://labs.mediatek.com/zh-tw/chipset/MT7688>
- [14] <https://www.raspberrypi.org/>
- [15] <http://beagleboard.org/>
- [16] <https://www.aaeon.com/tw/p/up-board-computer-board-for-professional-makers>

- [17] <https://developer.nvidia.com/embedded/buy/jetson-nano-devkit>
- [18] Z. Shelby and C. Bormann, “6LoWPAN: The Wireless Embedded Internet,” John Wiley & Sons, Aug. 2011.
- [19] B. M. Wilamowski and J. D Irwin, “Industrial Communication Systems,” CRC Press, Oct. 2017.
- [20] <https://www.wi-fi.org/discover-wi-fi/wi-fi-halow>
- [21] “802.11ah-2016 - IEEE Standard for Information technology-- Telecommunications and information exchange between systems - Local and metropolitan area networks--Specific requirements - Part 11: Wireless LAN Medium Access Control (MAC) and Physical Layer (PHY) Specifications Amendment 2: Sub 1 GHz License Exempt Operation,” Retrieved 2018-06-09.
- [22] <https://lora-alliance.org/about-lorawan>
- [23] <https://www.sigfox.com/en>
- [24] <http://www.weightless.org/>
- [25] <https://www.ingenu.com/>
- [26] https://www.3gpp.org/news-events/3gpp-news/1805-iot_r14
- [27] R. T. Fielding, et al., “Hypertext Transfer Protocol – HTTP/1.1,” IETF RFC 2616, June 1999.
- [28] Z. Shelby, K. Hartke, C. Bormann, “The Constrained Application Protocol (CoAP),” IETF RFC 7252, June 2014.
- [29] <http://mqtt.org/documentation>

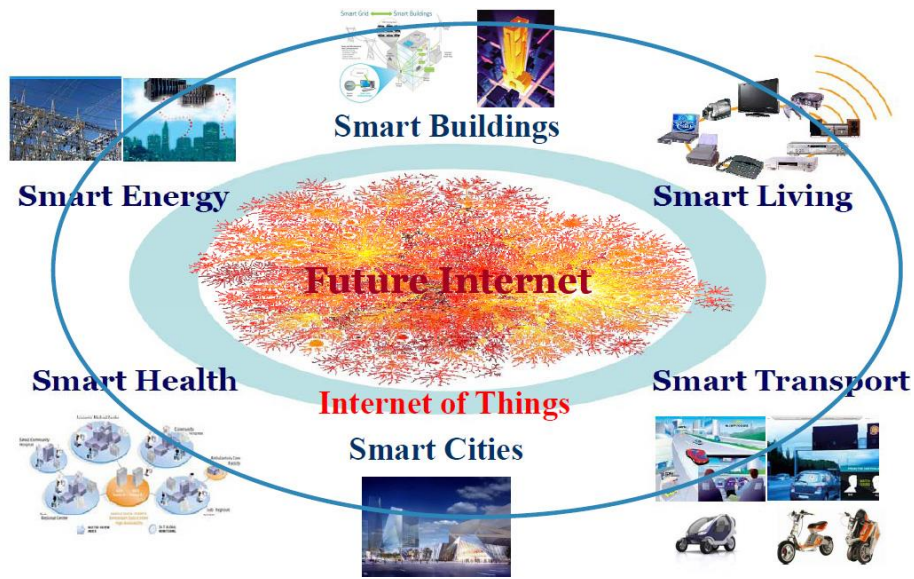


圖 1：物聯網將帶動各種智慧應用服務

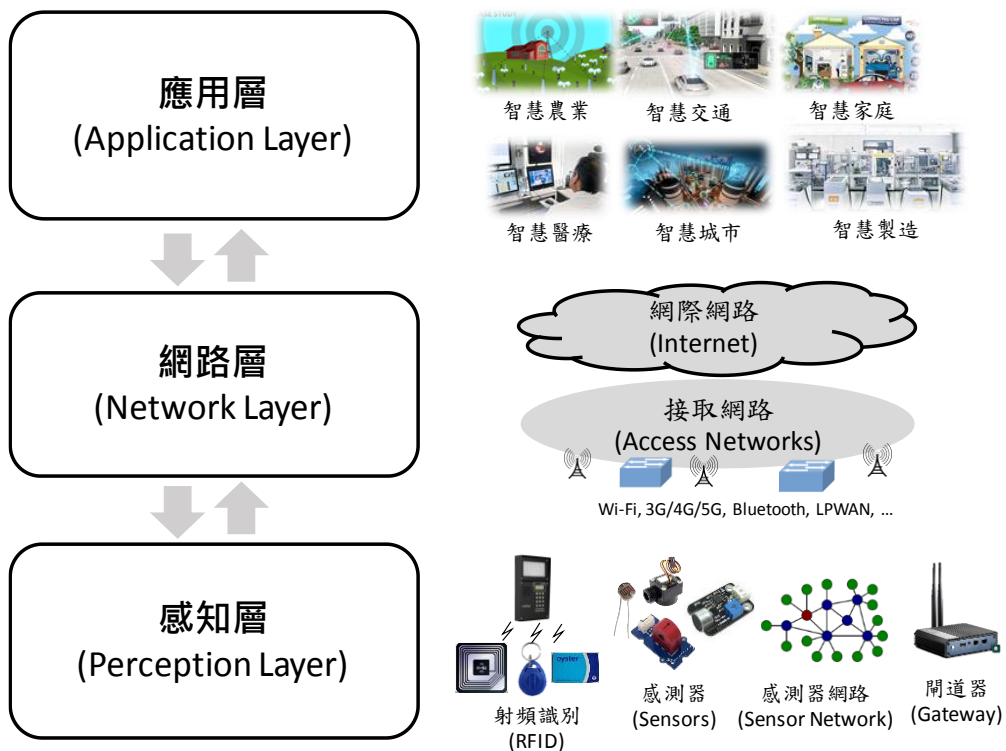


圖 2：物聯網系統參考架構

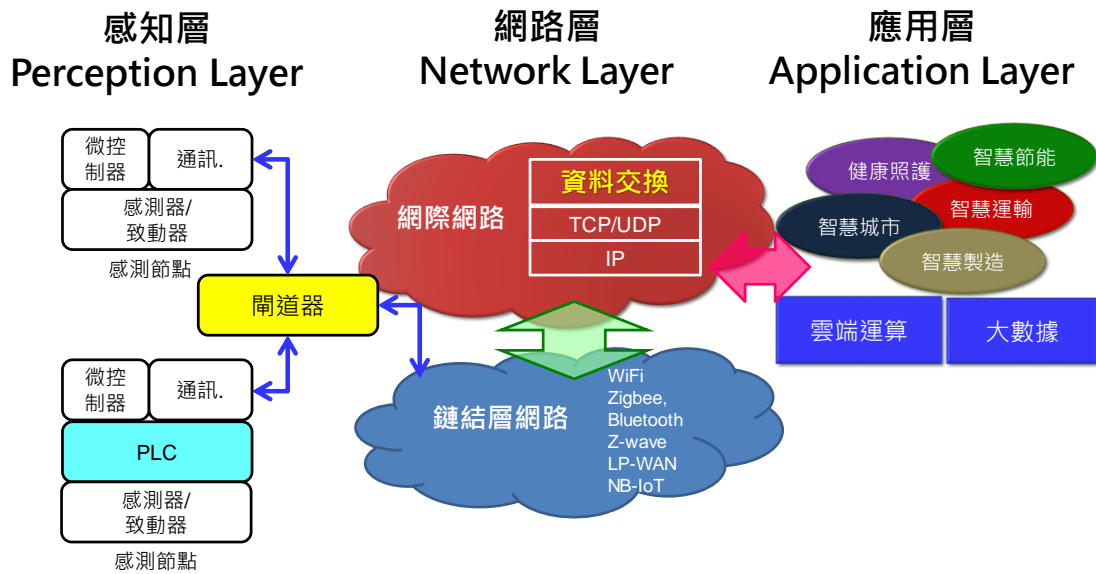


圖 3：物聯網系統實際組成

表 1：感知層無線網路技術比較

	Wi-Fi	802.11ah	802.15.4-based	BLE	非授權頻譜 LPWAN (LoRaWAN)	NB-IoT	LTE-M
資料速率 (bps)	1M~3.5G (ac)	150K~78 M	20K~250 K	1M (v4.x) 2M (v5)	300~50K (EU) 900~100K(US)	250K	1M
傳輸範圍	~ 100 m	~ 1 Km	~ 100 m	~100 m (v4.x) ~300m (v5)	2-5Km (urban) 15Km (rural)	15Km	~11Km
網路拓模 型態	Star	Star	Star, Cluster Tree, Mesh	Peer-to-Peer	Star	Star (蜂巢式)	Star (蜂巢式)
最大 裝置數	數十個	~ 6000	~ 65 K	---	Uplink:>1M, Downlink:<100 k	---	---
節電設計	N	Y	Y	Y	Y	Y	Y

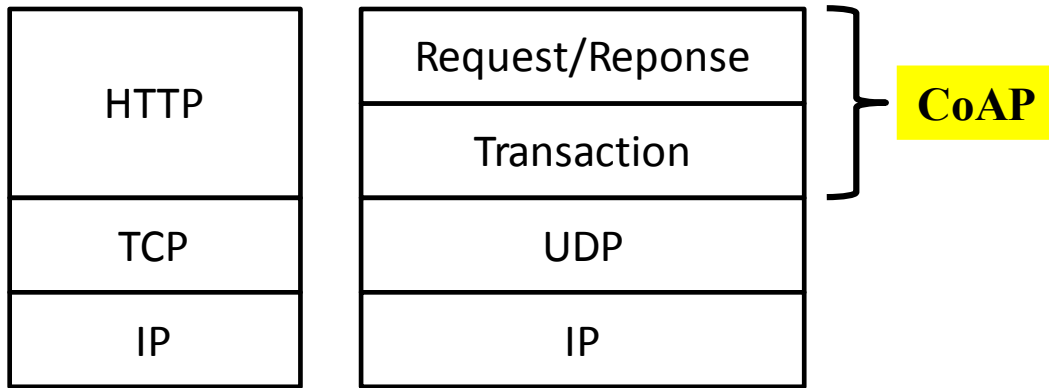


圖 4：CoAP 協定

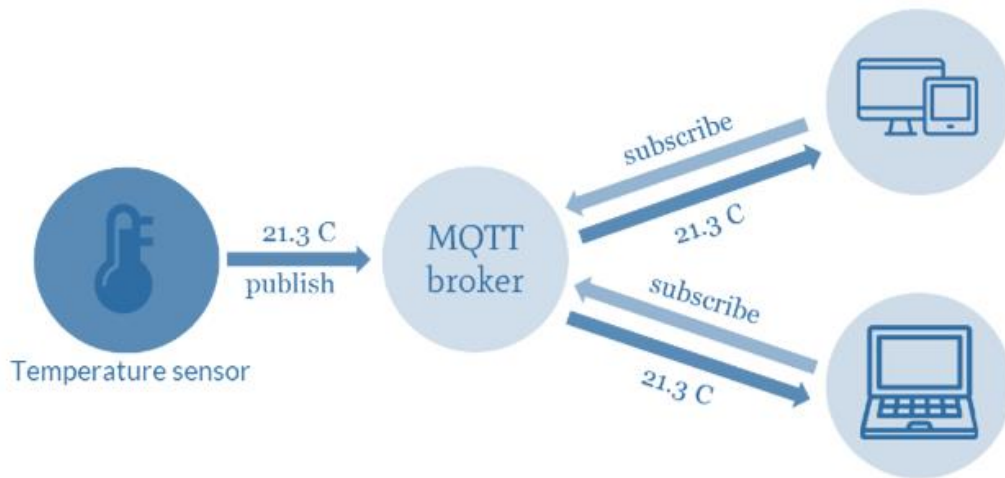


圖 5：MQT 運作模式

義大醫院、義守大學近期活動



義大醫院

多重抗藥性菌株之預防及管制

主講人：義大醫院感染管制部黃俊凱部長

日期：108年7月6日(六)

地點：義大癌治療醫院六樓會議廳

醫學人文典範獎座-Surgical training and professionalism
in preparation for a surgeon.

外科醫師養成訓練及專業的選擇

主講人：先進醫療技術整合發展委員會李伯皇主任委員

日期：108年7月18日(四)

地點：義大癌治療醫院六樓會議廳

外科預防性抗生素的使用

主講人：義大癌治療醫院內科部鍾幸君副部長

日期：108年8月1日(四)

地點：義大癌治療醫院六樓會議廳

Research Program in Liver Cancer and Viral Hepatitis – the Why, What and How

主講人：Professor of Medicine Division of Gastroenterology and Hepatology Liver Transplant program Department of Medicine Stanford University Medical Center

日期：108年8月3日(六)

地點：義大癌治療醫院六樓會議廳

正子掃描解讀:酮體與葡萄糖在失智症的迷思 Exploring the myth of ketones and glucose in AD by PET scan

主講人：台灣醫用迴旋加速器學會曾凱元常務理事

日期：108年8月8日(四)

地點：義大癌治療醫院六樓會議廳

個人防護具穿脫流程(含洗手)演練與評核

主講人：義大醫院感染管制科葉秋燕技術主任

日期：108年10月24日(四)

地點：義大癌治療醫院六樓會議廳

手部衛生推廣/隔離防護措施

主講人：義大醫院一般醫學兒科林庭逸醫師

日期：108年11月28日(四)

地點：義大癌治療醫院六樓會議廳

義守大學

義守大學108年高中生暑假體驗課程

活動對象：各高中職學生

日期：108年7月4日(四)

地點：義守大學校本部與醫學院區之各學院學系

科技部消息

* 公開徵求2020-2022臺波(NCBR-MOST)(國際合作鏈結法人)雙邊協議擴充加值型(add-on)國際合作計畫

- 一、本部補助經費項目包括：國際合作所需業務費、赴國外差旅費、符合本部規範額度上限內核予國際合作主持費新臺幣5,000元/月，本臺波雙邊協議擴充加值型計畫徵求案不核予管理費。
- 二、「臺波(NCBR-MOST)雙邊協議擴充加值型(add-on)國際合作計畫」研擬「擴充加值」經費金額與「原計畫」經費之總和應以新臺幣120萬/年為原則，惟實際核予經費以審查結果為準。
- 三、「臺波(NCBR-MOST)國際合作鏈結法人雙邊協議擴充加值型(add-on)國際合作計畫」研擬「擴充加值」經費金額與「原計畫」經費之總和應以新臺幣330萬/年為原則，惟實際核予經費以審查結果為準。
- 四、本案聯絡人：
 - (一)臺方(MOST)：科教發展及國際合作司 陳禹銘研究員
電話：02-2737-7959 Email: ymchen@most.gov.tw
 - (二)波蘭國家研究發展中心(NCBR)：Mr. Konrad Kosecki
電話：+48 22-39-07-460 Email: konrad.kosecki@ncbr.gov.pl
- 五、計畫申請截止日：108年7月30日(二)。
- 六、訊息相關網址：<https://www.most.gov.tw/folksonomy/rfpList>。

*徵求2020-2022年臺韓(MOST-NRF)雙邊協議型擴充加值(add-on)國際合作研究計畫

「雙邊協議型擴充加值 (add-on)國際合作研究計畫」，雙方研究人員組成合作研究團隊，共同合作進行本項研究計畫。

本項臺韓(MOST-NRF)雙邊合作研究計畫須由臺灣及韓國雙方計畫主持人共同研議並提出計畫申請。其中韓方主持人須依韓國國家研究基金會之規定向該基金會提出申請；我方計畫主持人須依本須知所述方式向本部申請「雙邊協議型擴充加值(add-on)國際合作研究計畫」。

一、本案聯絡人：

(一)臺灣(MOST)：科教發展及國際合作司 金曉珍研究員

Email: jsjen@most.gov.tw

(二)韓國(NRF)：Global Exchange Program Team Directorate for International Affairs National Research Foundation of Korea Ms. Kim Ji-min

Email: jmkim@nrf.re.kr

二、計畫申請截止日：108年7月30日(二)。

三、訊息相關網址：<https://www.most.gov.tw/folksonomy/rfpList>。

* 科技部109年度補助科學與技術人員國外短期研究案，
自108年5月1日起至8月1日止受理申請

本部109年度補助科學與技術人員國外短期研究案，持續配合政府新南向政策鼓勵申請機構推薦人選赴東協10國、南亞6國及紐澳等國家研究，擴展學術合作，重點如下：

一、上述國家包括東協10國(菲律賓、越南、寮國、柬埔寨、泰國、緬甸、馬來西亞、新加坡、印尼、汶萊)、南亞6國(印度、孟加拉、不丹、尼泊爾、巴基斯坦、斯里蘭卡)，以及紐西蘭、澳大利亞。

二、研究領域宜符合上述國家區域特色，及易發揮資源共享效益為主，內容涵括人文社會科學(如政治經濟發展、企業發展與管理、文學、藝術、語言、人才教育、社會文化、宗教信仰、南島語言與文化、科學教育)、自然科學(如大氣、海洋、地球科學、空間資訊、永續發展整合、防災科技)、生命科學、工程及應用科學等領域。

三、本案聯絡人(MOST)：

科教及國際合作司 謝婉琳小姐

電話：02-2737-7987

電腦操作問題請洽本部資訊系統服務專線

電話：02-2737-7590~7592

四、計畫申請截止日：108年8月1日(四)。

五、訊息相關網址：<https://www.most.gov.tw/folksonomy/rfpList>。

* 108年度「新型態產學研鏈結計畫」-價創計畫徵求公告

建立產學研連結創新研發之生態系統，提升研發成果商業化之可行性，達成衍生新創公司或促成廠商併購技術團隊之目的，徵求符合政府產業創新政策推動方向，具潛力發展為破壞式創新之研發成果：

- 一、技術已成熟可於1~2年內出場成立衍生新創公司或受併購之申請案，優先考慮。
- 二、已有投資人提出投資意願之申請案(需提出佐證資料如投資方評估報告等)，優先考慮。
- 三、計畫申請截止日：108年8月21日(三)。
- 四、訊息相關網址：<https://www.most.gov.tw/folksonomy/rfpList>。

* 109年度臺法幽蘭計畫(MOST-BFT ORCHID)雙邊人員交流互訪型計畫及雙邊研討會計畫

為發展臺灣與法國兩國研究單位間之科技交流，推展新的合作機會，本部與法國在臺協會比照法國外交部與其他國家共同建立之科技交流管道，推動「幽蘭計畫」。

一、本案聯絡人(MOST)：

科教發展及國際合作司 李佩育科長

電話：02-2737-7810

傳真：02-2737-7607

E-mail：pylee@most.gov.tw

二、計畫申請截止日：108年8月28日(三)。

三、訊息相關網址：<https://www.most.gov.tw/folksonomy/rfpList>。

*科技部「臺灣與波蘭、匈牙利、保加利亞及捷克雙邊人員互訪交流(2020-2021 PPP)計畫」

為培養國內年輕研究人員國際合作經驗，累積國際學術人脈及增進國際移動力，本部自2001年起分別與波蘭科學院(PAS)、匈牙利科學院(HAS)、保加利亞科學院(BAS)、捷克科學院(CAS)簽署協定推動雙邊人員互訪交流PPP5計畫，補助為先期規劃未來合作而研擬之雙方互訪交流計畫。

一、本案聯絡人(MOST)：

科教及國際合作司 陳禹銘研究員

電話：02-2737-7959

Email: ymchen@most.gov.tw

二、計畫申請截止日：108年9月2日(一)。

三、訊息相關網址：<https://www.most.gov.tw/folksonomy/rfpList>。

*徵求2020年度臺日(RIKEN)雙邊協議型擴充加值(add-on)國際合作研究計畫

「雙邊協議型擴充加值(add-on)國際合作研究計畫」，雙方研究人員組成合作團隊進行本項研究計畫。本項臺日(MOST-RIKEN)雙邊合作研究計畫須由臺灣及RIKEN雙方計畫主持人共同研議並提出計畫申請。日方主持人須依RIKEN之規定辦理；我方計畫主持人須依本公告所述方式向本部申請「雙邊協議型擴充加值(add-on)國際合作研究計畫」。

- 一、申請期間：2019年5月1日起至2019年9月30日止，申請機構須於系統彙整送出，並依第六點第十項規定，於申請截止日前函送申請名冊。申請人請控留申請機構受理窗口辦理行政作業之時間，以免逾期致影響申請權益。
- 二、每項申請案須由臺灣及RIKEN各1位主持人共同研議計畫內容，英文計畫名稱必須相同，申請件數每人以1件為限。
- 三、在專題計畫線上申請系統上方點選新增申請案，在計畫類別「專題類—隨到隨審計畫」下選擇「雙邊協議型擴充加值(add-on)國際合作計畫」進入，開始新增計畫，並依系統要求填列表格及上傳相關資料。

四、本案聯絡人：

(一)臺灣(MOST)：科教發展及國際合作司 金曉珍研究員
Email: jsjen@most.gov.tw

(二)日本(RIKEN)：International Affairs Section International Affairs Division RIKEN Ms. Shien Liu
Email: iad-collab@riken.jp

五、計畫申請截止日：108年9月30日。

六、訊息相關網址：<https://www.most.gov.tw/folksonomy/rfpList>。

產學合作消息

* 經濟部技術處「鼓勵中小企業開發新技術計畫」(SBIR)

- 一、SBIR計畫就是「小型企業創新研發計畫(Small Business Innovation Research)」，它是經濟部為鼓勵國內中小企業加強創新技術或產品的研發，依據「經濟部促進企業開發產業技術辦法」所訂定的計畫，期望能以此協助國內中小企業創新研發，加速提升中小企業之產業競爭力，以迎接面臨之挑戰。
- 二、申請資格：依公司法設立之中小企業。
- 三、受理期間：計畫為政府持續推動與支持之計畫，廠商可隨時提出申請，並無特定的申請截止日期。
- 四、相關連結：<http://www.sbir.org.tw/index>。

* 勞動部勞動力發展署高屏澎東分署「補助大專校院辦理就業學程計畫」

- 一、為提升大專生之就業知識、技能、態度，爰補助大專校院辦理實務導向之訓練課程，以協助大專生提高職涯規劃能力，增加職場競爭力及順利與職場接軌。課程包含「專精課程」、「職場體驗」及「共通核心職程課程」。
- 二、申請資格：台灣地區依中華民國大學法設立之公私立大學。

三、受理期間：依網站公告為主，每年約2、3月。

四、相關連結：https://www.wda.gov.tw/News_Content.aspx?n=85E1E406503C665B&sms=4AB77FB5C324175E&s=C6A795A82C17519E。

* 產業升級創新平台計畫

一、經濟部工業局原推動之「標竿新產品創新研發輔導計畫」(含主導性新產品計畫、創新應用服務計畫)，自104年起調整為「產業升級創新平台輔導計畫」，以「推高質」、「補關鍵」、「展系統」以及「育新興」等四大策略，「產業高值計畫」、「創新優化計畫」、「新興育成計畫」、「主題式研發計畫」、「研發貸款計畫」5大計畫，透過研發補助方式，鼓勵企業投入研發創新活動，開發具市場競爭力之產品或服務，提升自主研發能量技術，期以提升我國產業附加價值、產業結構優化，並鏈結國際市場。

二、申請資格：由單一企業或多家企業聯合提出申請；或可由企業與學術機構或法人機構共同提出申請(各計畫規範不同，詳情請參閱各計畫說明)。

三、受理期間：「產業高值計畫」、「創新優化計畫」、「新興育成計畫」計畫為政府持續推動與支持之計畫，廠商可隨時提出申請，並無特定的申請截止日期；其餘兩項依計畫辦公室公告為主。

四、相關連結：<https://tiip.itnet.org.tw/>。

*經濟部技術處「A+企業創新研發淬鍊計畫」相關計畫

- 一、為引導業者投入具潛力的前瞻產業技術開發，並鼓勵進行跨領域整合，以完備我國產業生態發展，經濟部技術處以「A+企業創新研發淬鍊計畫」名稱銜接原「業界開發產業技術計畫」，期望引導產業投入更具價值的高階先進技術開發，並鼓勵垂直領域及跨領域整合，協助補足產業缺口，發展完整產業生態體系，使產業創新成果發揮更大效益。
- 二、申請資格：依公司法設立之本公司或從事與創新服務研究發展活動相關具稅籍登記之事務所及醫療法人、財務健全、其專業團隊具從事提供知識之創造、流通或加值之工作經驗且有實績者，均可提出計畫申請。
- 三、受理期間：計畫為政府持續推動與支持之計畫，廠商可隨時提出申請，並無特定的申請截止日期。
- 四、相關連結：<https://aiip.tdp.org.tw/index.php>。

*經濟部工業局「協助傳統產業技術開發計畫」(CITD)

- 一、為落實照顧傳統產業政策，經濟部工業局度積極透過「協助傳統產業技術開發計畫」，將近投入新台幣4億元，協助並鼓勵傳統產業進行新產品開發、產品設計及聯合開發，預計將嘉惠290家以上傳統產業業者，提升其競爭力。
- 二、申請資格：須為民間傳統產業業者(詳細資格條件請參閱網站)。
- 三、受理期間：每年兩次，約為12月-隔年1月、4-5月(依網站公告為主)。
- 四、相關連結：<http://www.citd.moeaidb.gov.tw/CITDweb/Web/Default.aspx>。

*科技部「補助產學合作研究計畫」

一、整併原有的大產學、小產學及數位產學相關補助要點，並建構產業需求導向之產學合作模式，以整合運用研發資源，發揮大學及研究機構之研發力量，以期能透過產學的團隊合作與相互回饋的機制，提升國內科技研發的競爭力。分為「先導型」、「應用型」及「開發型」計畫。

二、申請資格：

(一)申請機構：係指公私立大專校院、公立研究機構及經本會認可之財團法人學術研究機構。

(二)合作企業：係指依我國相關法律設立之獨資事業、合夥事業及公司，或以營利為目的，依照外國法律組織登記，並經中華民國政府認許，在中華民國境內營業之公司，並以全程參與本會產學合作研究計畫為原則。

三、受理期間：(依網站公告為主)

(一)先導型產學合作計畫，申請日期約為每年2月。

(二)應用型產學合作計畫，申請日期約為每年2月及7月。

(三)開發型產學合作計畫，申請日期約為每年2月、7月及10月。

四、相關連結：https://www.most.gov.tw/folksonomy/list?subSite=&l=ch&menu_id=4dda1fd8-2aa9-412a-889b-9d34b50b6ccd&view_mode=listView。

*科技部「產學技術聯盟合作計畫(產學小聯盟)」

一、產學小聯盟鼓勵學術界研究人員以其過去研發之成果為主軸，成立「核心技術實驗室」，整合與該核心技術相關的企業，將其所累積之研發能量提供對外協助與服務，以實驗室為核心，與業界共同組成會員形式之產學技術聯盟，讓產、學間增加互動，提升業界的競爭能量及技術能量。本計畫以多年期個別型計畫形式提出。

二、申請資格：

(一)申請機構(以下稱計畫執行機構)：係指公私立大專校院及公立研究機關(構)。

(二)計畫主持人及共同之資格：比照本部補助專題研究計畫作業要點第三點規定。

(三)產學技術聯盟合作計畫：指學術界研究人員以其過去研發之成果及核心技術為主軸，對外提供協助與服務為目標之計畫，可由單一或多位研究人員組成，其項目應涵蓋核心技術之內容、該技術之應用性、未來可能參與共同組成會員形式之聯盟會員及該聯盟運作計畫等。

(四)聯盟會員：指依商業登記法登記之獨資或合夥事業、公司或財團法人。

三、受理期間：依網站公告為主，每年約5~8月。

四、相關連結：http://web.etop.org.tw/eTop_Alliance/。



義守大學 研究發展處

84001 高雄市大樹區學城路一段1號

電話：07-657-7711

傳真：07-657-7471

Mail : research@isu.edu.tw

發行人： 陳振遠 校長

總編輯： 林麗娟 副校長
沈季燕 副校長
陳俊益 研發長

編輯部： 張寧組長、盧雅真代理
組長、陳映臻小姐



義大醫院 醫學研究部醫學教育部

82445 高雄市燕巢區角宿里義大路1號

電話：07-615-0011

傳真：07-615-5352

Mail : ed103308@edah.org.tw

ed100075@edah.org.tw

杜元坤 院長

楊生滿 副院長
沈德村 行政長

陳素婷課長、李雅純小姐、
陳麗芬小姐

